TECHNISCHE UNIVERSITÄT MÜNCHEN

Max-Planck-Institut für Plasmaphysik

A Feasibility Study of Tungsten-Fiber-Reinforced Tungsten Composites with Engineered Interfaces

Juan Du

Vollständiger Abdruck der von der Fakultät für Maschinenwesen der Technischen Universität München zur Erlangung des akademischen Grades eines

Doktor-Ingenieurs

genehmigten Dissertation.

Vorsitzender:	Univ.-Prof. Dr.-Ing. H. Baier
Prüfer der Dissertation:	1. Hon.-Prof. Dr.-Ing., Dr.-Eng. (Japan) H. H. Bolt
	2. Univ.-Prof. Dr. mont. habil. E. Werner

Die Dissertation wurde am 25.10.2010 bei der Technischen Universität München eingereicht und durch die Fakultät für Maschinenwesen am 11.02.2011 angenommen.

To my family

Kurzfassung

Wolfram gilt als ein viel versprechender Kandidat für den Einsatz als Struktur- und Armierungsmaterial im Divertor eines thermonuklearen Fusionsreaktors. Allerdings ist seine Sprödigkeit (unzureichende Zähigkeit) der größte Nachteil bei einem Einsatz unter den anspruchsvollen thermomechanischen Bedingungen. Die mit konventionellen Ansätzen bisher erreichte Zähigkeit ist immer noch unzureichend für die Anforderungen. Deshalb gibt es einen hohen Bedarf an der Erforschung neuer Mechanismen zur Zähigkeitsteigerung, welche auch unter versprödenden Bedingungen aktiv bleiben.

In dieser Arbeit wird eine solche zähigkeitssteigernde Methode vorgeschlagen. Sie basiert auf einer Verstärkung mit Wolframfasern (W_f/W_m-Verbundwerkstoff) mit speziell beschichteten Grenzflächen. Die Methode ist analog dem zähigkeitssteigernden Mechanismus von keramikfaserverstärkten Keramiken (FCMC), der auf Energiedissipation durch kontrollierte Ablösungen und Reibung an der Faser/Matrix-Grenzfläche basiert. Die Brucheigenschaften der eingebrachten Grenzfläche sind die Schlüsselfaktoren, welche die Gesamtzähigkeit des Verbundes bestimmen. In dieser Arbeit wird eine ausführliche Analyse des Bruchverhaltens diverser Grenzflächen von W_f/W_m-Verbundwerkstoffen durchgeführt, um die Realisierbarkeit eines zähigkeitsgesteigerten W_f/W_m-Verbundwerkstoffes zu zeigen.

Kommerziell erhältlicher Wolframdraht wurde für die Faserverstärkung und dichtes Wolfram wurde als Matrix gewählt. Basierend auf duktilem Kupfer, sprödem Zirkon- und Erbiumoxid, schmierendem Kohlenstoff und deren Kombinationen wurden insgesamt 14 verschiedene Beschichtungen als Grenzflächen untersucht. Die Grenzflächen wurden in einer Magnetronbeschichtungsanlage auf die Fasern aufgebracht. Die Wolframmatrix wurde durch chemische Gasphasenabscheidung (CVD) mit der vollen Dichte von 19.3±0.2 g/cm^3 um die Fasern herum abgeschieden.

Die Eigenschaften der Grenzflächen wurden mit Hilfe von Faserdurchdrückversuchen (Push-out Test) an Einzelfaser-W_f/W_m-Verbundwerkstoffen. Die Ergebnisse zeigen, dass die Grenzflächenbruchenergien das Kriterium für eine Rissablenkung erfüllen.

Die Struktur der Grenzflächen wurde sowohl vor als auch nach den Durchdrückversuchen mit Hilfe eines Rasterelektronenmikroskopes analysiert, das mit einem fokussierten Ionenstrahl zum freischneiden der Grenzflächen ausgerüstet ist. Die Ergebnisse lassen darauf schließen, dass sich die Versagenszone übereinstimmend mit

den Ergebnissen der Grenzflächenparameterbestimmung ausbildet. Die Ablenkung eines Risses an der Grenzfläche wurde durch einen 3-Punkt-Biegversuch unmittelbar gezeigt. Hierbei zeigte sich ein Verhalten ähnlich zähigkeitsgesteigertem FCMCs.

Grenzflächen aus Zirkon- und Erbiumoxid zeigten eine höhere thermische Stabilität, während Kupfer- und Kohlenstoffgrenzflächen stärker durch eine Wärmebehandlung beeinflusst wurden.

Die Vorhersage der mechanischen Eigenschaften für W_f/W_m-Verbundwerkstoffen mit mehreren Fasern lassen darauf schließen, dass das Versagensverhalten des W_f/W_m-Verbundwerkstoffes dem typisch „zäher“ Werkstoffe entsprechen wird. Dies ist in guter Übereinstimmung mit den ermittelten Grenzflächeneigenschaften und den Ergebnissen der Rissablenkungsuntersuchung und unterstützt die ursprüngliche Motivation dieser Arbeit.

Abstract

Tungsten is a primary candidate for the structural and armor materials for the divertor of thermonuclear fusion reactors. However, the brittleness (lack of toughness) is the most critical drawback of tungsten under such complex thermo-mechanical operating conditions. The achieved and the projected toughness of tungsten based on conventional approaches are insufficient for the design requirements. Therefore, there is an urgent need to explore novel toughening mechanisms for tungsten to retain its toughness even under conditions of embrittlement.

In this work, such a toughening method for tungsten is proposed based on the reinforcement of tungsten fibers (W_f/W_m composites) and engineered interfaces. The underlying toughening mechanism is analogous to that of a fiber-reinforced ceramic matrix composite (FCMC), which relies on energy dissipation by controlled debonding and friction at the fiber/matrix interfaces. The fracture properties of the engineered interface are the key factors controlling the overall composite toughness. In this work, intensive analysis has been performed on the fracture behavior of various engineered interfaces of W_f/W_m composites for exploring the feasibility of producing a toughened W_f/W_m composite.

Commercial tungsten wires (fibers) were selected as reinforcement, while dense tungsten was chosen as the matrix. Based on the brittle zirconia and erbia, the ductile copper, the lubricating carbon, and their combinations, 14 types of coatings were used as interfaces. The interface coatings were deposited successfully via magnetron sputter deposition and the tungsten matrix was fabricated via chemical vapor deposition (CVD) with full density, 19.3±0.2 g/cm^3.

The interfacial parameters were calibrated by means of a fiber push-out test on a single-fiber W_f/W_m composite. The results showed that the interfacial fracture energy of employed interfaces satisfied the fracture criteria for the crack deflection.

Microscopic analysis of the interface structures was carried out before and after the push-out test by means of scanning electron microscope (SEM) equipped with focused ion beam (FIB) engraving the embedded interface domains. The results of the interfacial debonding location were in accordance with the interfacial parameter calibration results. The interfacial crack deflection was also directly demonstrated by a three-point bending (3PB) test, which coincided exactly with the typical behavior of a toughened FCMC.

Higher thermal stability was found in the zirconia and the erbia interfaces, while the copper and carbon interfaces were affected more by the heat treatment.

Mechanical property prediction of the W_f/W_m composites with multiple fibers indicated that the stress-strain curves of the involved W_f/W_m composites were of typical 'tough' material type, which agreed well with the interfacial parameter calibration results and the interfacial crack deflection demonstration results, supporting the primary motivation of this thesis.

Symbol list

B_1 : constant, $= E_m \nu_f / [E_m(1-\nu_f) + E_f(1+\nu_m)]$

B_2 : $= 1 - 2\upsilon_f B_1$

Δ : average energy absorption, kJ/m^2

c : crack length, m

c_* : critical crack length, m

c_f : fiber volume fraction

c_m : matrix volume fraction

d_i : diameter of the indenter head, μm

d_f : diameter of fiber, μm

d_0 : displacement in the dynamic event, μm

D_f : diameter of the specimen holder (down side), μm

D_m : diameter of the specimen, μm

E : Young's modulus, GPa

E_m : matrix Young's modulus, GPa

E_f : fiber Young's modulus, GPa

E_c : composite Young's modulus, GPa

E' : $= E/(1-\nu^2)$ in plain strain, GPa

ζ_m : matrix shear modulus, $\approx E_m / \left[2(1+\nu_m)\right]$, GPa

Γ : energy release rate, J/m^2

Γ_D : debonding energy release rate, $=\Gamma_i$ in W_f/W_m composite, J/m^2

Γ_c : critical energy release rate, or fracture energy, J/m^2

Γ_i : the mixed-mode fracture energy of the interface, J/m^2

G_i : the mode II fracture energy of the interface, assumed to be equal to Γ_i, J/m^2

Γ_f : the mode I fracture energy of fiber, J/m^2

Γ_m : the mode I fracture energy of matrix, J/m^2

H : specimen thickness, mm

K : stress intensity factor, MPa·m$^{1/2}$

K_1 : fracture toughness of the single-fiber W_f/W_m composite, MPa·m$^{1/2}$

K_c : critical stress intensity factor, or fracture toughness, MPa·m$^{1/2}$

K_f : fiber fracture toughness, MPa·m$^{1/2}$

K_m : matrix fracture toughness, MPa·m$^{1/2}$

k : constant, $=E_m\nu_f/[E_m(1-\nu_f)+E_f(1+\nu_m)]$

L : embedded length, mm

L' : stretched length, m

l : sliding (debonding) length, mm

$\overline{l_S}$: associated spacing of σ_{sat}, μm

P : applied load, N

P_i : initial debonding load, N

P_d : partial debonding load, N

$P_{\max}$: maximum debonding load, N

P_{fr} : maximum frictional sliding load, N

ΔP : the difference between $P_{\max}$ and P_{fr}, N

p : applied pressure, MPa

p_d : maximum stress at the complete debonding, $= P_{\max} / \pi r_f^2$, MPa

p_R : residual stress, MPa

Ω : crack resistance

$\overline{R}$: effective matrix radius, mm

R : composite cylinder radius, mm

r_f : fiber radial, μm

S : diameter of the specimen holder (upside), mm

U : energy change of a load plate per unit thickness, J/m

v_i : indenter velocity, μm/s

X : acoustic dissipation factor

χ : crack coefficient

α_1 : elastic mismatch of the interface, $= (E_f' - E_m') / (E_f' + E_m')$

α_2 : elastic constant parameter in shear-lag theory

γ : surface energy

ε_{mc} : composite strain at matrix cracking, %

ε_{sat} : composite strain at saturating matrix cracking, %

ε_y : composite yield strain, %

ε_u : composite ultimate strain, %

ε_{f-u} : fiber ultimate strain, %

μ : friction coefficient

ν : Poisson's ration

υ : spring stretched length, m

σ_i : cluster deviation of the push-out data

σ : applied stress, far field average stress, MPa

σ_y : main applied stress component (parallel to the interface), MPa

σ_x : stress component acting normal to the interface, MPa

σ_{mc} : matrix cracking stress, MPa

σ_{sat} : saturating matrix cracking stress, MPa

σ_y : composite yield stress, MPa

$\sigma_{f-yield}$: fiber yield stress, MPa

σ_u : composite ultimate stress, MPa

σ_D : debonding stress, $= 2c_f \sqrt{\frac{E_f E_c \Gamma_D}{c_m E_m r_r}}$, MPa

σ_S : sliding stress, $= \left(\frac{2c_f E}{c_m E_m} \right) \frac{\tau_R}{\rho}$, MPa

σ_{f-u} : fiber ultimate stress, MPa

σ_* : critical crack stress, MPa

σ_0 : interfacial residual stress, MPa

σ_r : radial stress, MPa

σ_R : interface radial stress, MPa

σ_P : stress caused by Poisson's effect, MPa

σ_z : applies axial stress, MPa

$\sigma_{z,\Delta T}$: thermal mismatch radial stress, MPa

σ_f^∞ : far-field average fiber stress, MPa

σ_m^{∞} :far-field average matrix stress, MPa

τ_d : interfacial shear strength, MPa

τ_{fr} : interfacial sliding shear stress, MPa

τ_0 : residual shear stress, $=\sigma_0 \times \mu$, MPa

τ_R : asperity caused shear stress, $=\sigma_R \times \mu$, MPa

$\tau_{sliding}$: average sliding stress, MPa

$\tau_{\Delta T}$: thermal mismatch shear stress, MPa

$\tau_{R,\Delta T}$: total shear stress consisting of τ_R and $\tau_{\Delta T}$, MPa

τ_D : cohesive shear strength, $=\left(\frac{\rho c_m E_m}{2c_f E}\right)\sigma_D$, MPa

σ_A : $=\frac{2c_f E_c \sqrt{E_f \tau_R}}{c_m E_m}$

ξ : $=2\mu B_1 l_1 / r_f$

ρ : $=\left[\frac{2\zeta_m E_c}{c_m E_m E_f \log(\overline{R}/r)}\right]^{1/2}$

Subscripts:

i	indenter
i	initial
0	original
f	fiber
m	matrix
c	composite
mc	matrix cracking
max	maximum
min	minimum
d	debonding
fr	friction
y	yielding
u	ultimate
sat	saturating

Contents

Chapter 1

Introduction

1.1 Motivation

The first realistic attempt to solve the world's energy problems by means of controlled thermonuclear fusion dates back to the 1950s [1]. In order to understand the underlying physical principles and technological capabilities of fusion, intensive activities have been carried out worldwide with a steady increase in performance over the decades. Several experimental fusion devices of different types and scales have been built with the main aim to understand the underlying physics and the material-related issues which are critical for the extreme loading conditions [2-7]. The International Thermonuclear Experimental Reactor (ITER), is currently under construction and aiming at exceeding the break-even point, meaning more output power would be generated than input power consumed [8]. Already, research and development for a Demonstration Power Plant (DEMO), the successor to ITER, which is aimed at demonstrating the feasibility of fusion as a commercial power source, has begun.

The most easily achievable fusion reaction for energy generation on earth is the fusion of the hydrogen isotopes deuterium (D) and tritium (T), due to their large cross-section at relatively moderate temperatures of about 100 MK [9]. The reaction products are helium and a high-energy neutron:

$$D + T \rightarrow {}^{4}He\ (3.5\ MeV) + n\ (14.1\ MeV) \tag{1.1}$$

The hot plasma is thermally insulated from the surrounding materials via magnetic confinement [9]. Heat is generated by neutrons and highly energetic particles impacting the walls (blanket and divertor). The heat is then removed by coolants which, in turn, produce conventional electrical energy via steam generators.

The hottest wall region in a fusion reactor is the divertor located at the bottom of the vacuum chamber. The divertor system (consisting of the baffle, dome, inner and outer wing, as well as the vertical target) is responsible for both heat removal and exhausting the He ash, the unburnt D and T, and other impurities [10]. The choice of materials is limited to those that meet certain requirements including mechanical and thermo-physical

properties, radiation effects, chemical compatibility and corrosion resistance, material availability, cost and joining technology, as well as safety and waste disposal requirements [11, 12].

For DEMO, surface heat fluxes up to 15 MW/m^2 are expected in the divertor region [13]. Tungsten (W) has been selected as a primary candidate for the structural and armor materials for the divertor (see Table 1.1, the divertor modes according to the European Power Plant Conceptual Study (PPCS)) due to its unique thermo-physical properties (high conductivity and low expansion coefficient at high temperature, high strength and high melting point, and excellent surface erosion resistance) [14-17]. Nearly 15% of the total fusion thermal power has to be removed efficiently via the divertor—from the W armor to the coolant flowing through the structure material tubes [18]. Among the concept-designs of the divertor, the helium (He)-cooled divertor designs (Modes B and C according to PPCS, see Table 1.1) are one of the most attractive modes due to their high operation reliability and thermodynamic efficiency [18-19]. E.g., Fig. 1.1 shows the schematic drawing of the EU-HEMJ (He-cooled modular divertor with multiple-jet cooling) finger concept of a He-cooled W-alloy divertor system [20, 21]. The high-flux testing results of the mockups based on this design show that although the He-jet-cooling system can achieve the required divertor performance under heat flux of 10 MW/m^2, its operation reliability was extremely limited by the pre-existing defects caused by construction and the cracks formed due to the heat flux in the W structural alloys [21-23]. The simulation results based on an optimized concept (integrated plate/finger concept) showed that for He inlet/outlet temperatures of 600 °C/700 °C, respectively, and a surface heat flux of 10 MW/m^2, the maximum W-alloy temperature is 1241 °C, and the maximum combined stress is 435 MPa [24]. Therefore, the W structural material has to show stable, good performances under conditions with wide working temperature ranges from (600 °C, due to the joining to the ODS (oxide dispersion strengthening) steel) to 1300 °C (due to the recrystallization of W), high pressures (He gas, ≥10 MPa), and high thermal stresses (~450 MPa, caused by joining to ODS) and the heat flux impact during operation) [19-25]. Under such complex thermo-mechanical operating conditions, W is faced with a number of drawbacks: brittleness at “low” temperatures, overall low fracture toughness, DBTT (ductile brittle transaction temperature) well above room temperature, and embrittlement due to neutron irradiation (production of lattice defects) and recrystallization [14-17]. Therefore, the most serious issue of W being used as plasma facing components (especially structural materials) is the low fracture toughness (low ductility).

Table 1.1. Operating conditions and requirements of the divertor component according to PPCS [14-17].

Parameters	Mode A	Mode B	Mode C	Mode D
Armor material	W	W	W	W
Structure material	Copper alloy (CuCrZr)	Tungsten at high heat removal part and advanced ODS as back-bone		SiC_f/SiC
Divertor peak load	15 MW/m^2	>10 MW/m^2	>10 MW/m^2	>5 MW/m^2
Coolant	Water	He	He	He or liquid metal
Inlet/outlet temperature	140/325 °C	600/700 °C	600/700 °C	600 °C ~/-
Average neutron wall load	2.2 MW/m^2	2.0 MW/m^2	2.2 MW/m^2	2.4 MW/m^2
Highest structure material operation temperature	~550 °C	1200~1300 °C	1200~1300 °C	1200~1300 °C

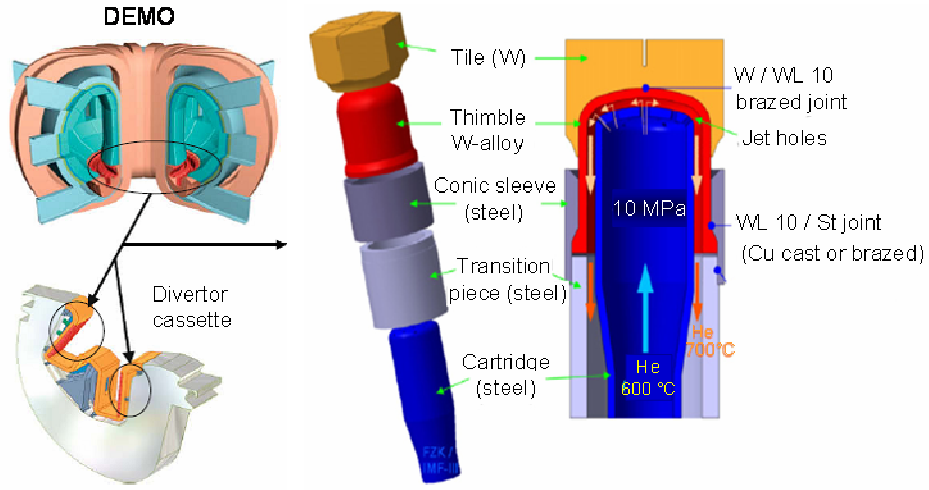

Figure 1.1. Schematic drawing of the EU-HEMJ finger concept of a He-cooled W-alloy divertor system. WL 10: W-1% La_2O_3; St joint: steel joint [20-21]

In order to obtain safe and more reliable operating conditions, greater efforts and increasing budgets have been devoted to improve the ductility of tungsten. The "grain boundary designs"—the optimization of grain size and shape, grain boundary character and impurities, as well as dislocation density and arrangement—are the most widely employed methods [26-29]. Metallurgical techniques, such as dispersion (La_2O_3), doping (K), or alloying (Re), have been adopted to improve the grain boundary character and impurity; but approaches based on those techniques show no significant improvement in the low-temperature brittleness of tungsten [26-28]. An ultra-fine grain (UFG)

microstructure created via severe plastic deformation (SPD), which has been adopted to increase the dislocation density resulted in an increase of the tungsten fracture toughness by a factor of five (to ~30 MPa·$m^{1/2}$), but only at room temperature [29]. UFG-W alloys, which combine both redistribution of impurities and high dislocation densities were previously thought to exhibit a high fracture toughness. However, after being exposed to 1200 °C for 1 h the fracture toughness of potassium-doped tungsten alloys treated by SPD is reduced severely due to recrystallization, since the onset of recovery and recrystallization is shifted towards lower temperatures due to the stored energy after SPD [14].

In spite of intensive research efforts, the hitherto achieved tungsten toughness based on these conventional approaches is still insufficient for the design requirements. Microstructure instability and embrittlement due to neutron irradiation are the main unsolved concerns. Additionally, requirements due to plasma compatibility and low activation for neutron irradiation impose a severe limitation on the selection of chemical compositions, so that the availability of metallurgical techniques is also strongly restricted. Therefore, there is an urgent need to explore an innovative toughening mechanism which functions effectively even under neutron irradiation and in the embrittling temperature regime.

For the last two decades, active research efforts have been conducted to develop long fiber-reinforced ceramic matrix composites (FCMCs) for high-temperature structural applications [30]. The toughness of FCMCs has been notably improved, and overall mechanical performance was successfully approved in several industrial applications (e.g., brake disks of aircrafts or racing cars) [31-53]. The working principle of a high toughness FCMC is the non-plastic energy dissipation caused by the controlled interfacial cracking (debonding) and the subsequent frictional sliding at the fiber/matrix interfaces [30-54]. When a running matrix crack meets an array of fibers oriented perpendicularly to the crack plane, the crack can deflect along the interfaces, provided a specific mechanical fracture condition is satisfied. Then the fibers bridge the opening primary crack and suppress its dynamic propagation. As the applied load is increased, the crack opens further and the interfacial debonding continues, leading to a frictional fiber pull-out. The energy consumed by the crack deflection and fiber sliding is a measure of apparent toughness. The toughening mechanism of FCMCs is now well understood in terms of the fracture mechanics, where mechanical fracture properties of the interface are the determining parameters. The details about the FCMCs toughening mechanism are discussed in chapter 2.

This toughening mechanism of FCMCs can also apply to brittle tungsten, provided that the reinforcing fibers are strong enough and that the fiber/matrix interfaces satisfy

the energy-dissipation criteria. Tungsten-fiber-reinforced tungsten matrix composites (W_f/W_m) are a candidate in this context. Commercially available tungsten wires are generally very strong (tensile strength >2.5 GPa) and more ductile (fracture strain >2%). These beneficial properties are due to the structure being extremely textured and fine grained. Hence, the original toughness of the tungsten wires can be utilized until the wires become fully embrittled during fusion operation. The amount of its contribution to the total toughness of a W_f/W_m composite will depend on the volume fraction of the fibers. On the other hand, the overall chemical purity will only be modified slightly by interface coating because thin films (<1 μm) are used. The fracture toughness of the W_f/W_m composite is predicted to be improved when the interface coating between the fiber and the matrix introduces energy consumption by interfacial debonding and frictional fiber sliding. There is no previous publication existing in the literature dealing with these kinds of tungsten composites. The idea of a novel W_f/W_m composite based on a fundamentally different toughening mechanism is the motivation for the present work.

1.2 Objective and strategy

The goal of this thesis is to demonstrate the feasibility of synthesizing a toughened W_f/W_m composite using the FCMCs toughening mechanism. A suitable interface between the W fiber and the W matrix is a basic requirement for achieving the high fracture toughness. Therefore, in order to optimize the interface between W fiber and W matrix to produce the aforementioned energy dissipation, the main focus of this work lies in the investigation of the interfacial fracture behavior of W_f/W_m composites with various engineered interfaces.

In this work, the main areas of interest in exploring the interfacial fracture behavior of the W_f/W_m composites are:

1. Design and synthesis of the W_f/W_m composites. The basic composite model—the single-filament (fiber) W_f/W_m composite model—is designed for the investigation of the interfacial fracture behavior. Various materials are selected as interfaces since there is no literature about interfaces of W_f/W_m composites.

2. Investigation of the interfacial fracture properties of W_f/W_m composites. A fiber push-out test is a convenient method to extract the fracture parameters of an interface. Interfacial parameters are determined by calibrating the experimental data from the extensive push-out tests with theoretical models. Additionally, a miniaturized three-point bending test is employed for direct observation of the interfacial debonding behavior when the interface is enduring a tensile load. Mechanical tests are performed on the

specimens after heat treatment to explore the thermal stability of the interfaces of W_f/W_m composites.

3. Microstructure analysis of the interfaces of W_f/W_m composites. Microstructure analysis of the interface domains is carried out before and after the push-out test by means of scanning electron microscopy (SEM) and focused ion beam (FIB) preparation. The energy dispersive x-ray spectroscopy (EDXS) and secondary ion mass spectrometry (SIMS) are adopted for demonstrating the chemical composition and distribution of the interfaces.

4. Mechanical property prediction of the W_f/W_m composite with multiple fibers. Mechanical properties of the W_f/W_m composite with multiple fibers was predicted based on results obtained from the single filament W_f/W_m composite.

The theoretical background on the FCMCs toughening mechanism, the W_f/W_m composite interface selection, the W_f/W_m composite fabrication, the push-out test, the three point bending test, the mechanical property prediction, and the microstructure identification techniques are described in detail in chapter 2. The material and experimental details are described in chapter 3. The results and relevant discussions of the microstructure and chemical composition analysis of the interface, the interfacial fracture behavior investigation, the interface thermal stability analysis, as well as the mechanical property prediction of the W_f/W_m composites with multiple fibers are presented in chapter 4 and chapter 5, respectively. In chapter 6, a summary of this thesis and concluding remarks are given.

Chapter 2

Background knowledge

2.1 W_f/W_m composite concept

2.1.1 General view of composite

Composite materials are formed by combining two or more materials to meet a specific engineering role by exploiting the desirable properties of the components, whilst minimizing the harmful effects of their less desirable properties [55, 56].

The composites are classified according to the type of matrix material: Polymer Matrix Composites (PMCs), such as glass fiber reinforced polymers; Metal Matrix Composites (MMCs), such as aluminium reinforced with ceramic particles or short fiber; Ceramic Matrix Composites (CMCs), such as SiC whisker reinforced alumina [57]. Fig. 2.1 shows examples of typical microstructures for the three main classes, grouped according to the nature of the matrix.

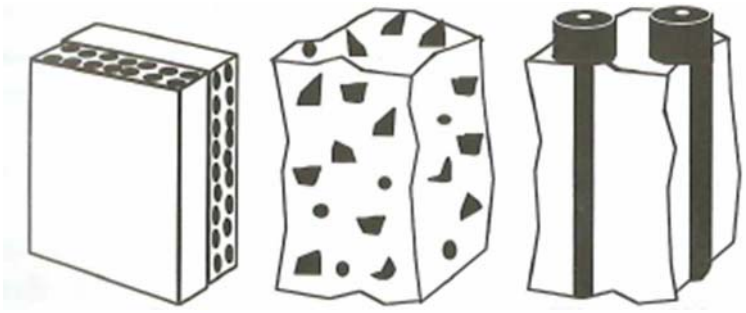

Figure 2.1. Schematic depiction of representative polymer, metal and ceramic matrix composites [57]

PMCs are aiming to elevate the strength and the stiffness of the materials by incorporating high stiffness fibers or particles since polymers have lower strength and modulus. MMCs can achieve desirable features such as low density, tailored thermal

expansion, conductivity, as well as high stiffness and strength due to the incorporation of the reinforcement. For example, the superalloys used in jet engines can easily withstand temperatures up to 800°C and can be operated up to 1100°C with oxidation-resistant coatings [58]. However, beyond this temperature, one must use ceramic materials. Ceramic materials have high strength, low density, chemical inertness and even high stiffness of extreme high temperature. However, these attractive properties come with one deadly flaw, namely: an utter lack of toughness. Therefore, CMCs are aiming to toughen the matrix by incorporating fibers in the ceramic and thus exploit the attractive high-temperature strength and environmental resistance of composite without risking catastrophic failures [57, 58].

Fiber-reinforced ceramic matrix composites (FCMCs) constitute one of the most popular techniques of composite design. It is based on taking advantage of the high strength and high stiffness of the fibers, which are combined with the matrix in order to obtain a combination of mechanical properties that cannot be achieved with either constituent alone. The fibers can be continuous-fiber (long-fiber), short-fiber (whiskers). The arrays of fibers can be random, parallel, laminate, woven, braided or knitted. The following parts will mainly focus on parallel arranged continuous-fiber reinforced ceramic matrix composites to introduce the concept of tungsten fiber reinforced tungsten matrix composite.

2.1.2 FCMC toughening mechanism

2.1.2.1 Basic concept of toughness

Toughness, is defined as the amount of energy per volume that a material can absorb before rupturing. It represents the resistance to fracture of a material when stressed.

The most well known ‘fracture mechanics’ is given by Griffith theory (1920) [59]. Griffith fracture theory points out that a crack cannot propagate unless the energy of the system is thereby decreased. The energy being released when a crack advances comes from the associated release of stored elastic strain in the surrounding materials (plus any work done by the loading system). If this is insufficient to counterbalance the energy absorbed in the material through the creation of new fracture surfaces and associated internal damage or deformation processes, then the crack cannot advance. In many materials, efficient mechanisms for internal energy absorption are stimulated by the high stresses at a crack tip, so that the energy balance for crack propagation is often unfavorable and so they exhibit high toughness (resistance to fracture). This is particularly true for most metals, since the dislocation motion which occurs is highly effective in this regard.

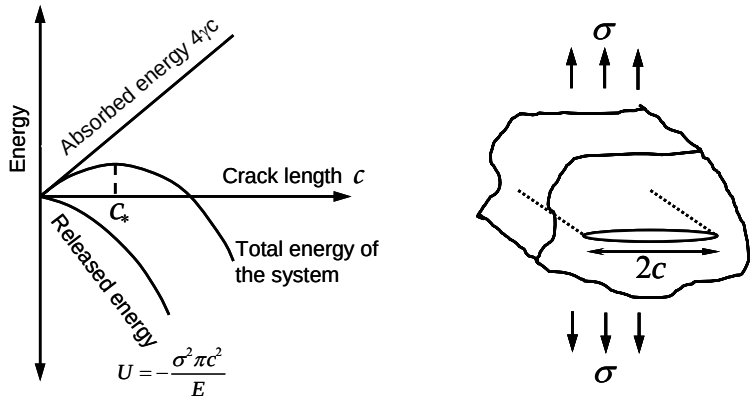

Figure 2.2. Schematic plot of the two contributions to the energy associated with the presence if the crack in a brittle material, as a function of crack length. A crack of length, c_* or larger will grow spontaneously, with a reduction in the total energy [57]

In brittle materials, such as glass, in which energy absorption processes are not readily stimulated, the only significant energy penalty of crack propagation comes from the new surface area of the crack faces. Griffith showed that the change in the stored energy of a loaded plate of unit thickness, caused by the introduction of an interior crack of length $2c$, is given by

$$U = -\frac{\sigma^2 \pi c^2}{E} \tag{2.1}$$

where σ is the applied stress and E is the Young's modulus. The other contribution to the overall energy change is that required to create the new surface area, which is positive and has a value of $4\gamma c$, where γ is the surface energy. The dependence of these two contributions on the length of the crack is shown in Fig. 2.2 [57]. Only cracks longer than a critical length, c_*, will grow spontaneously (with reduction in net energy). This critical length is found by differentiating the total energy with respect to crack length and setting the result equal to zero, leading to

$$c_* = \frac{2\gamma E}{\sigma^2 \pi} \tag{2.2}$$

This approach was extended by Irwin (1948) [59] to encompass tougher materials. This surface energy term 2γ is supplemented by other contributions to energy absorption in the vicinity of an advancing crack tip. For a given applied stress and pre-existing crack size, an expression can be obtained from Eq. (2.2) for the energy release rate, Γ, which has units of J/m^2

$$\Gamma = \frac{\sigma^2 \pi c}{E} \tag{2.3}$$

For fracture to occur, this must exceed a critical value, sometimes referred to as the crack resistance, Ω. This critical value represents the total energy absorbed, per unit of crack advance area and is often termed Γ_c, the critical energy release rate, or fracture energy. Values of Γ_c are fairly easy to obtain experimentally. For example, the work done in a tension or bending test is given by the area under a load-displacement curve and, provided this energy is all permanently absorbed in the specimen, the fracture energy is then found by simply dividing by the area created through the failure. Tough (ductile) metals have fracture energies of 30~100 kJ/m^2; whereas a brittle material, such as glass, can have a value as low as 0.01 kJ/m^2. Rearranging Eq. (2.3), the stress necessary to cause spontaneous fracture in a component with a pre-existing crack of size c ($2c$ if internal) can be written as

$$\sigma_* = \sqrt{\frac{\Gamma_c E}{\pi c}} \tag{2.4}$$

This approach is particularly useful in practical terms, because attention is diverted to the complex problem of the precise nature of the stress field close to the tip of the crack to a more global approach involving macroscopic quantities which are measurable experimentally. However, there is still interest in the phenomena occurring locally near the crack tip. A useful link is provided between the energy and stress field approaches by the concept of a stress intensity factor K. This parameter, which largely evolved from the work of Irwin in the 1950s [59] can be expressed as

$$K = \sigma\sqrt{\pi c} \tag{2.5}$$

It therefore encompasses the effects of both the applied load and the pre-existing crack size, with the relative weighting that these two parameters have in determining the value of Γ, the energy release rate (see Eq. (2.3)), which characterizes the severity of the stress field around the crack tip. A critical value can be identified, corresponding to the case where the associated value of Γ reaches Γ_c

$$K_c = \sigma_*\sqrt{\pi c} = \sqrt{E\Gamma_c} \tag{2.6}$$

This critical stress intensity factor is often known as the fracture toughness. For tough materials, the fracture toughness can exceed 100 MPa·m$^{1/2}$, while a brittle material might typically have a value around 1 MPa·m$^{1/2}$.

2.1.2.2 FCMC fracture toughness

During fracture of a brittle material, energy is consumed in creating the new surface area of the crack faces. In a FCMC, the energy consumed by crack deflection (new

surface creation) and fiber frictional sliding along the interfaces between the fiber and the matrix leads to a high tolerance for the fracture of the composite that in turn, leads to a high fracture resistance (fracture energy), although neither fiber nor matrix are tough materials. Practical evidence of this toughening effect is not scarce. A composite made from glass fiber and epoxy resin has a fracture energy comparable with those of metals (Γ_c ~50 kJ/m^2), even though the constituents are both brittle (Γ_c ~0.01-0.1 kJ/m^2). This high toughness is closely linked with interfacial effects [57].

Figure 2.3 is a typical schematic illustration of an aligned ceramic-matrix composite reinforced with continuous fibers in the longitudinal direction under a tensile stress. Its corresponding stress-strain characteristics are shown in Fig. 2.4 a. At a stress of σ_{mc}, the stress-strain curve shows a change in the slope (a dip), indicating an occurrence of matrix cracking (normally, reinforcement (fiber) has higher toughness and a larger strain-to-fracture value than those of the matrix). The initial matrix cracking can occur at different locations simultaneously and thus introduce multiple cracking. As the multiple cracking develops, the slip zones of neighboring cracks overlap and produce a shielding effect. After the shielding process is completed, a saturation crack density results. This occurs at a stress of σ_{sat} (see Fig. 2.4 a). When the propagating primary matrix cracks meet the array of fibers standing perpendicular to the crack faces, they can deflect along the vertical interfaces when a specific fracture mechanical condition is satisfied (see Fig. 2.3). Then the strong fibers collectively bridge the primary cracks suppressing their dynamic extensions. The stress-strain curve continues to rise until, at a stress marked σ_y, the fibers start to yield, followed by σ_u, the fiber bundle fails (see Fig. 2.4 a). Subsequently, the phenomenon of fiber pull-out (frictional sliding out of the matrix) starts. The extent of this fiber pull-out region depends critically on the interfacial frictional resistance. Thus the fiber/matrix interfacial properties have a strong influence on the stress-strain curve of the composite. If the interface bonding is too strong, the matrix cracking will be accompanied by a small amount of fiber pull-out, which is an undesirable characteristic from a toughness viewpoint. The total amount of the consumed energy by crack deflection and fiber frictional sliding is a measure of the apparent toughness. The increased fracture toughness is a result of the controlled fracture behavior of the composite, while an unreinforced matrix or a reinforced matrix with an interface between fiber and matrix which does not introduce interfacial debonding fails catastrophically (see Fig. 2.4 b).

2.1 W_f/W_m composite concept

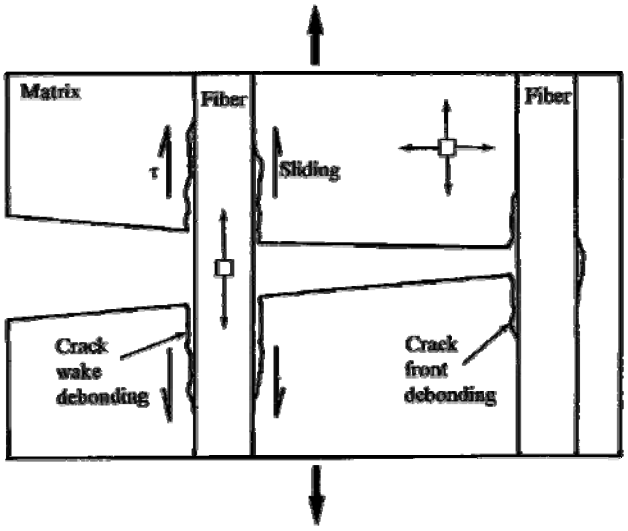

Figure 2.3. Schematic illustration of ceramic-matrix composite reinforced with continuous fiber [41]

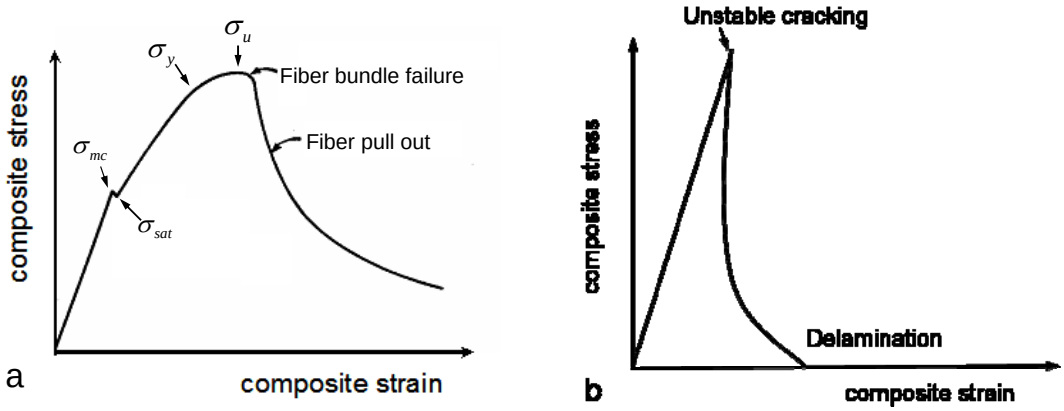

Figure 2.4. Schematic illustrating the range of stress-strain characteristic exhibited by ceramic-matrix composite: a) 'Tough' composite; b) 'Brittle' composite [41]

It is apparent that the area under the stress-strain curve in Fig. 2.4 a is much larger than that in Fig. 2.4 b, indicating that the composite with interfacial debonding has a higher fracture energy Γ_c which indicates higher fracture toughness K_c The interfacial debonding (crack deflection) characteristic is the prerequisite for realizing an increased fracture toughness of a composite. The crack deflection criteria are discussed below.

2.1.2.3 Crack deflection criteria

Cook and Gorden (1964) [58] analyzed the phenomenon of crack deflection or the formation of secondary cracks at a weak interface in terms of the stress state at the crack tip. Considering a fiber/matrix interface perpendicular to the main advancing crack, at the

tip of any crack, a triaxial stress state (plane strain) or a biaxial stress (plane stress) is present. Fig. 2.5 shows schematically the stress distribution at a crack tip. The main applied stress component, σ_y, has a very high value at the crack tip, and decreases sharply as the distance from the crack tip lengthens. The stress component acting normal to the interface, σ_x, is zero at the crack tip; it rises to a maximum value at a short distance from the crack tip and then falls off in a manner similar to σ_y. Now, it is easy to visualize that if the interface tensile strength is less than the maximum value of σ_x, then the interface will fail in front of the crack tip. According to the estimates of Cook and Gordon, an interfacial strength of 1/5 or less than that of the main stress component, σ_y , will cause the opening of the interface in front of the crack tip [58].

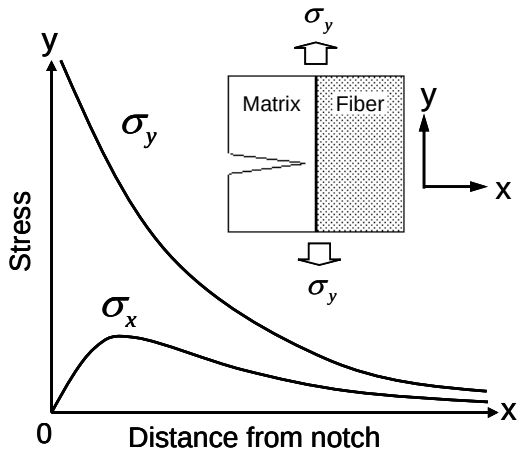

Figure 2.5. Stress distributions at a crack tip [58]

More sophisticated analyses of crack interaction with an interface have been proposed. One of the most popular results was made by He and Hutchinson (1989) [60]. Their results give the conditions for fiber/matrix debonding in terms of the energy requirements; see Fig. 2.6, a plot is made of Γ_i / Γ_f vs. α_1, where Γ_i is the mixed-mode interfacial fracture energy, Γ_f is the mode I fracture energy of the fiber, and α_1 is a measure of elastic mismatch as defined in the Fig. caption. There are three basic modes for the crack propagation: mode I (opening mode) corresponds to normal separation of the crack faces under the action of tensile stresses; mode II (sliding mode) corresponds to longitudinal shearing of the crack faces in a direction normal to the crack front; mode III (tearing mode) corresponds to lateral shearing parallel to the crack front [59]. Interfacial cracks often propagate under mixed-mode loading conditions which contains both mode I and mode II. This plot shows the conditions under which the crack will deflect along the interface or propagate through the interface into the fiber. For all values of Γ_i / Γ_f, area below the dashed line, interface debonding is predicted. For the special case of zero

elastic mismatch, i.e., for $\alpha_1 = 0$, the fiber/matrix interface will debond for Γ_i / Γ_f less than about 0.25. Conversely, for Γ_i / Γ_f greater than 0.25, the crack will propagate across the fiber. In general, for the elastic mismatch, with α_1 greater than zero, the minimum interfacial toughness required for interface debonding increases, i.e. a high modulus fiber tends to favor debonding. One shortcoming of this analysis is that it treats the fiber and matrix as isotropic materials, which is not always true, especially for the fiber. But this criterion is still a good guideline for high toughness composite design.

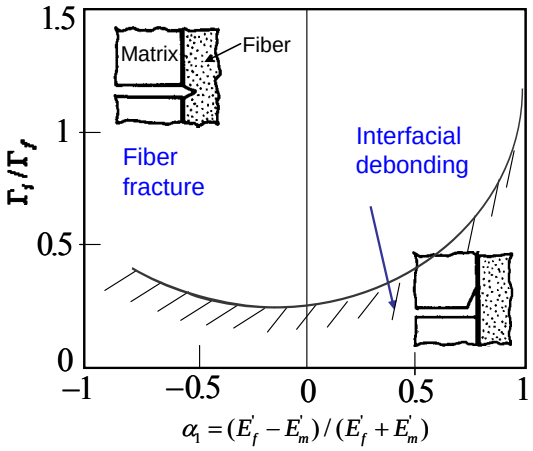

Figure 2.6. Fiber/matrix debonding criterion in terms of the energy requirements. 'm' and 'f' represent matrix and fiber respectively. $E' = E/(1-\nu^2)$ in plain strain, with ν as the Poisson's ratio [60]

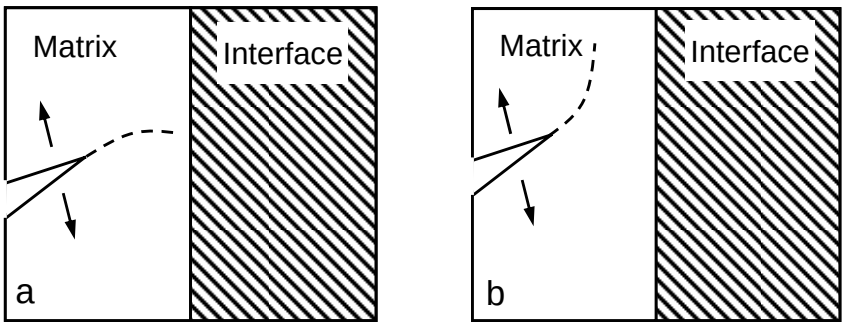

Figure 2.7. Propagation of slant crack in the proximity of an interface: a) matrix is stiffer than interface; b) matrix is more compliant than interface

Sometimes it happens that the crack at an interface deflects back into the original material and grows approximately parallel to the interface in its vicinity (of course it may turn in this way even before reaching the interface). This can occur if the fracture toughness of the matrix is lower than that of the interface, $\Gamma_m < \Gamma_i$. A crack generally has a greater tendency to deflection if it lies in a more compliant material: if a crack approaches perpendicularly to an interface behind which there is a stiffer material, the

stress intensity factor near the interface diminishes, as if the crack were repelled by that material. Fig. 2.7 shows the schematic image of these crack propagation types. Therefore, in order to achieve interfacial debonding, the interface should satisfy another criterion apart from Γ_i / Γ_f <0.25: the fracture energy of the interface must be less than that of the matrix [61].

2.1.2.4 FCMC interface and interfacial property evaluation

In order to generate the energy dissipation, a weak interface is usually adopted between the fiber and the matrix in a FCMC. The interface can be classified into four types according to the mode of energy dissipation. Fig. 2.8 shows the schematic drawings of each type. Type a) adopts no real interface coating but utilizes the surface roughness of fiber and matrix to form a weak bonding; type b 1) adopts a weak interface layer which may allow the microcracks diffuse in the layer; type b 2) utilizes the weak bonding between fiber and interface coating leading to a debonding between them; type c) adopts the interface coating with porous or particles leading to a crack deflection along these weak locations; type d) utilizes heterogeneous multilayer structure coating leading to a crack deflection in the multiple barriers (multiple inner interfaces).

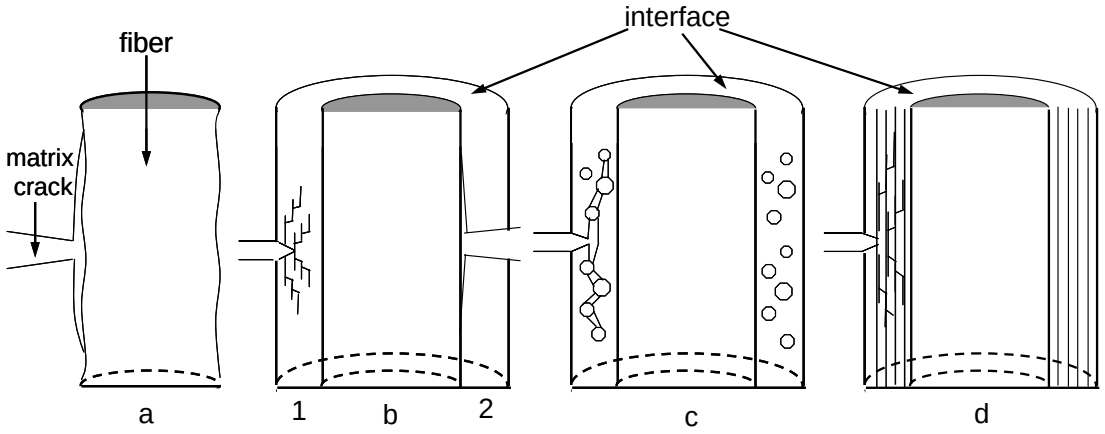

Figure 2.8. Interface bonds formed: a) by fiber surface roughness; b 1) by microcracks diffusing in the interface, b 2) by debonding between fiber and interface; c) by crack deflection in weak locations in a porous layer; d) by crack deflection in a multiple barrier [62]

When a fiber-reinforced composite is bearing a load, the interface transfers stress between fiber and matrix. In a perfect bonded interface, the stress transfer is an elastic transfer; while after an interfacial debonding event, the stress transfer is governed by the Coulomb friction law. In a practical case, the load transfer process contains both types and is complex. The interfacial bonding and debonding behaviors have strong influence on the mechanical properties of the composite. There are several interfacial parameters

which represent the interfacial properties: interfacial shear strength, τ_d, which is defined as the maximum average shear stress that a fiber/matrix interface can afford before it begins to fail; interface radial stress, σ_R which is defined as the radial stress generated by surface roughness of the debonded surfaces; interfacial residual stress, σ_0, which is a radial stress on the interface generated due to thermal expansion mismatch between the fiber and the matrix; interfacial friction coefficient μ, which is defined as the ratio between the radial stresses and the shear stresses of the interface; asperity caused shear stress τ_R, which is generated by $\tau_R = \sigma_R \times \mu$, also known as roughness caused shear stress; interfacial fracture energy, Γ_i which is defined as the critical energy release rate of the interfacial debonding process.

In order to obtain the values of these interfacial parameters and to evaluate the interfacial properties, a great amount of effort has been made to establish micromechanical models of the load transfer across the interface. Test methods including the single fiber compression test, the fiber fragmentation test, the fiber pull-out test, the fiber push-out (or indentation) test and the slice compression test are widely used [63]. Among these methods, fiber pull-out test and fiber push-out test are the most popular and well established techniques for evaluating interfacial properties using single filament (fiber) composite.

A single fiber pull-out test is performed as follows: a single fiber, half embedded into a matrix, is extracted under a tensile load, until the fiber debonds from the matrix and is pulled out. While a single fiber push-out test is conducted as follows: a thin slice specimen with the fiber central axis normal to the specimen surface is fixed; a compressed load is applied on the embedded fiber until the fiber debonds from the matrix and is pushed out. The recorded load-displacement curve can be interpreted using theoretical models. Fig. 2.9 shows the schematic illustrations of the load distribution of the fiber pull-out test and push-out test as well as their representative load-displacement curve. In principle, pull-out and push-out tests relate to similar micromechanics, but a push-out test has greater advantages being more convenient to implement.

Therefore, this work adopted the single fiber push-out test to explore the interfacial properties of the W_f/W_m composite. The details of interfacial parameters calibration based on the single fiber push-out test will be discussed in chapter 2.3.1.

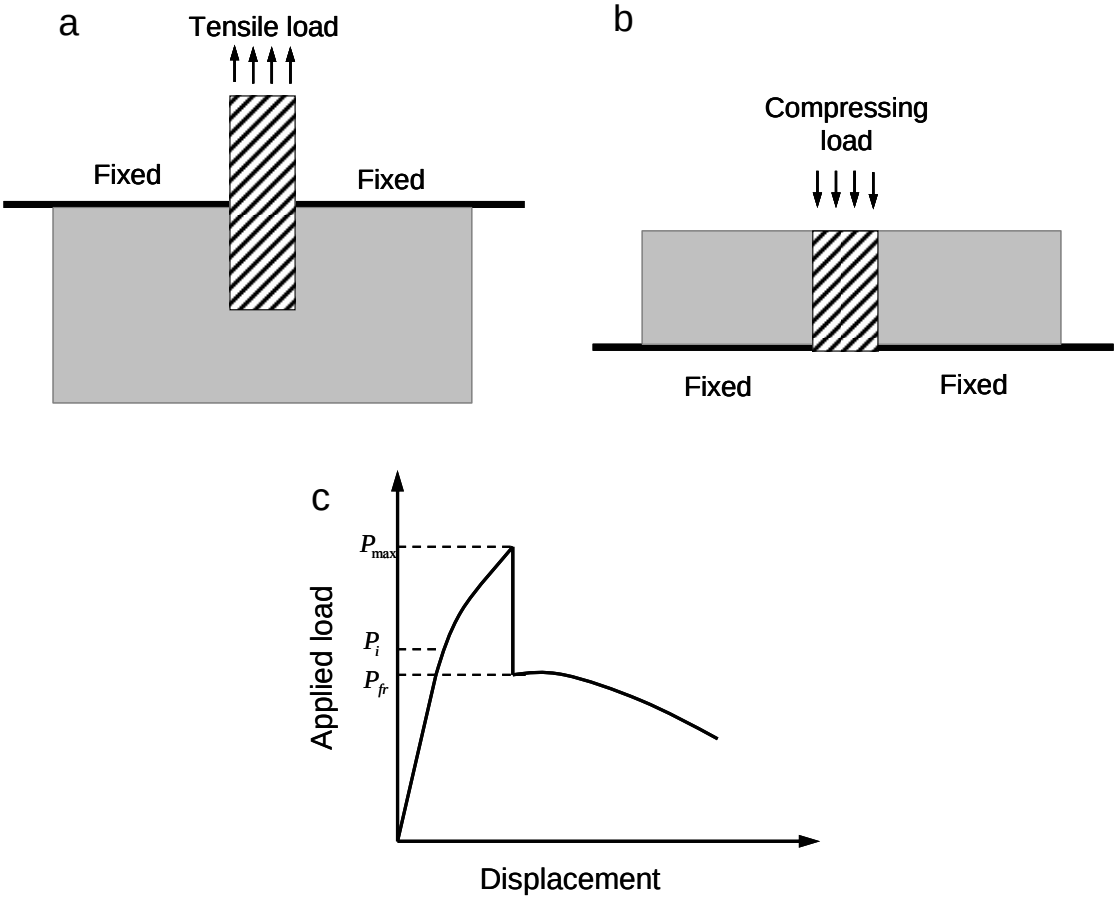

Figure 2.9. Schematic exhibitions of the loading situation of the fiber pull-out test and push-out test: a) pull-out test; b) push-out test; c) representative load-displacement curve, P_i indicates the load of initial debonding event, P_{max} is the maximum debonding load and P_{fr} is the fiber frictional sidling load

2.1.3 W_f/W_m composite design

Tungsten is a high atomic number metal. The biggest problem for tungsten as a structure material for Plasma Facing Components (PFCs) is brittleness, which is similar to that for ceramics. It is a reasonable expectation to be able to fabricate high-toughness tungsten by utilizing the FCMCs toughening mechanism. Therefore, the concept of tungsten fiber reinforced tungsten matrix (W_f/W_m) composite was created.

Figure 2.10 a is the designed structure of a W_f/W_m composite with fiber volume fraction c_f =0.6. The commercial tungsten fiber (wire) was selected as the reinforcement; dense tungsten was chosen as the matrix. Fig. 2.10 b shows the single-fiber W_f/W_m composite model used in this work. Commercially available tungsten wires are generally very strong and have more ductility (tensile strength: > 2.5 GPa). Hence the original toughness of tungsten wires can be utilized until the wires become fully embrittled

during service. On the other hand, the overall chemical purity will be just slightly modified by interface coating because only thin films (<1 μm) are used. Increased fracture toughness is expected for the W_f/W_m composite, as the interface coating introduces interfacial properties satisfying the crack deflection criteria.

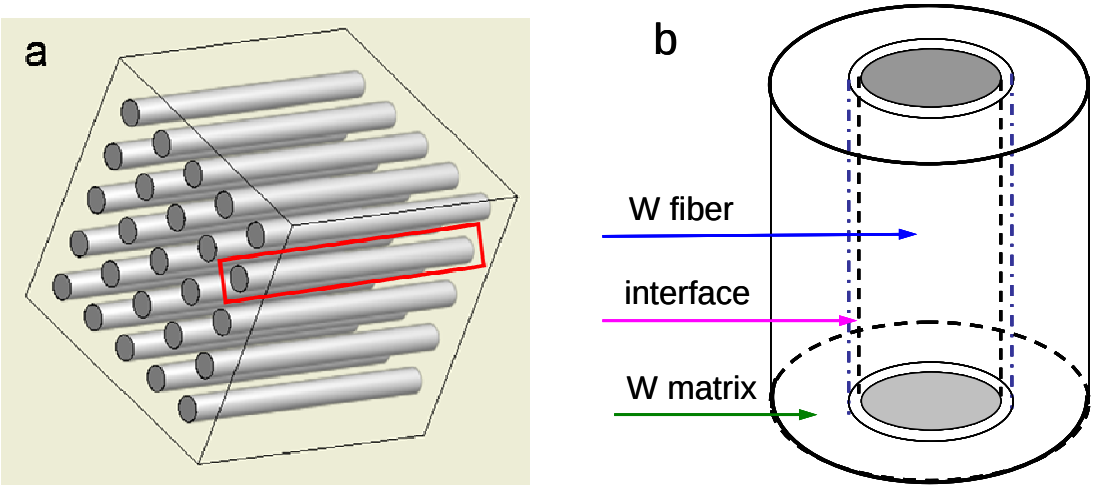

Figure 2.10. Schematic designed structure of the W_f/W_m composite: a) multi-filament; b) single filament

Thus, the most critical issue is to select the proper interface materials. Since there is no earlier publication dealing with these kinds of tungsten composites and no information about the interface selection for the W_f/W_m composite, a variety of materials are considered in this work regarding the interface types of FCMC (see Fig 2.8). Type a) is not suitable for W_f/W_m composite since the fiber and matrix will diffuse into each other at a high working temperature if there is no interlayer between W fiber and W matrix. Thus, the interface materials are selected concerning types b), c), and d), and discussed as follows.

Firstly, oxide coatings

Oxides are usually brittle and contain pores and microcracks (fit types b 1) and c)). The oxide coating interfaces are expected to introduce the crack deflection behavior for a composite. ZrO_2 and Er_2O_3 were selected as the interface material for the W_f/W_m composite due to their high thermal stability and low activation due to irradiation [64-68]. The thickness of the interface normally affects the interfacial properties and toughness of the composite [63]. Therefore, ZrO_2 coating with 150 nm, 450 nm, and 950 nm, and Er_2O_3 coating with 600 nm, and 1000 nm, respectively, were fabricated in order to analyze the thickness effect.

Secondly, ductile coatings

Copper (Cu) is a typical ductile material. No phase exists containing Cu and W thus no chemical bonding is expected between Cu and W [68]. The weak bonding between Cu and W is expected to generate the debonding between fiber and interface coating (fit type b 2)). Besides, higher energy dissipation is expected due to the strong plastic deformation of Cu. Moreover, the very high thermal conductivity of Cu is useful for the W_f/W_m composite to be used as structural material for a high heat impact component. Therefore, Cu with 150 nm, and 450 nm, respectively, were selected as the interface coating.

Thirdly, lubricating coating

Carbon is a typical lubricating material. It has been widely used in the CMC research area for decades [69-71]. The graphite structure provides small combining power between the hexagonal planes which is expected to generate the microcracks along the hexagonal planes (fit type b 1)). Therefore, carbon with a thickness of 600 nm was selected as the candidate for the interface material.

Fourthly, multilayer structure coatings

High energy dissipation is expected in a multilayer structure interface (see Fig. 2.8, type d). Therefore, based on the selected coatings above, ZrO_2/Zr multilayer, ZrO_2/W multilayer, Er_2O_3/W multilayer, Er/W multilayer, Cu/W multilayer were designed as the interface.

More details about the interface structure are discussed in chapter 3.

2.2 W_f/W_m composite fabrication

2.2.1 Interface coating fabrication-magnetron sputtering

Sputter deposition is one of the most popular physical vapor deposition (PVD) techniques and is widely used for coatings (thin films) fabrication. PVD is a vacuum-based coating technology to produce thin films of various materials onto various surfaces.

In a sputtering process ions are supplied by an inert gas ionized through a glow discharge (a current flowing through a low-pressure gas, plasma) between the target as cathode and the substrate (specimen) holder or the chamber wall as anode. The generated ions are accelerated toward the cathode (the target) and sputter atoms out of the target materials. The neutral target atoms impinge on a substrate (specimen), forming a coating [72].

According to the plasma creation and sustainment, the sputtering can be classified as DC (direct current) sputtering and RF (radio frequency) sputtering. DC sputtering refers

to a DC discharge with the plasma created and sustained by a DC power source, while RF discharge is with an RF power source [72, 73]. Fig. 2.11 shows the schematic drawing of the arrangements of these sputtering processes.

The deposition rate is affected by the sputtering yield, the gas pressure, and the bias (a negative voltage between substrate and the ground). More information refers to Ohring [73].

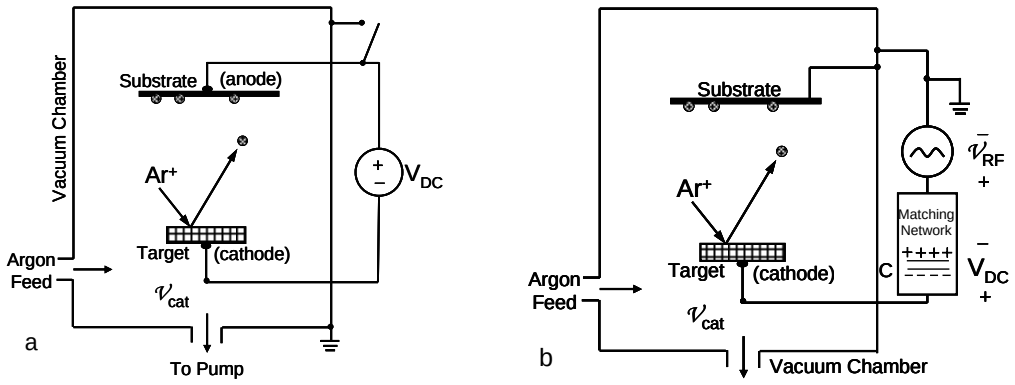

Figure 2.11. Schematic fashion of categories: a) DC, DC sputtering utilizes a DC gaseous discharge. Ions strike the target (the cathode of the discharge), which is the deposition source. The substrate and/or the vacuum chamber walls may be the anode; b) RF, in RF sputtering, there are typically a small area cathode (the target) and a large area anode, in series with a blocking capacitor (C). The capacitor is actually part of an impedance-matching network that improves the power transfer from the RF source to the plasma discharge [72]

Magnetrons make use of the fact that a magnetic field parallel to the target surface can constrain electron motion to the vicinity of the target. Electrons trapped by the magnetic field increase the probability of an ionizing electron-atom collision occurring. The increased ionization efficiency of a magnetron results in a dense plasma at the target region. This, in turn, leads to increased ion bombardment of the target, giving higher sputtering rates and, therefore, higher deposition rates at the substrate. In addition, the increased ionization efficiency achieved in the magnetron mode allows the discharge to be maintained at lower operating pressures (typically, 10^{-3} mbar, compared to 10^{-2} mbar) and lower operating voltages (typically, -500V, compared to-2 to -3 kV) than in the basic sputtering mode [74]. Fig. 2.12 shows the basic magnetic field arrangement during the sputtering process.

Presently, a lot of progress has been made in magnetron sputtering. Such as, the unbalance magnetron sputtering deposits dense films without introducing excessive intrinsic stress; multi-cathode sputtering devices deposit different layers on substrates without opening the vacuum chamber and changing cathodes; reactive sputtering

deposits compounds on substrates by sputtering from metallic targets in the presence of a reactive gas (usually mixed with the inert working gas, mostly Ar) [73-75].

The magnetron sputtering device utilized in this work is the 'Discovery®18 Multi-Cathode DC/RF-Denton Vacuum system, It has 4 cathodes and an oxygen gas supply system.

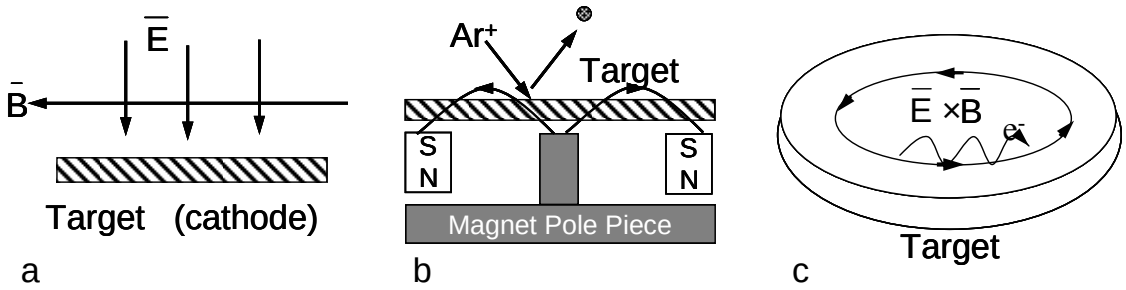

Figure 2.12. Different magnetic field styles of magnetron sputtering: a) in the planar magnetron sputtering arrangement, whether DC or RF, a static magnetic field is created parallel to the surface of the sputtering target to retain secondary electrons in that region; b) an annular design, such as the one shown here schematically in exploded cross section, is often employed; c) the electron drift in the $-\overline{E}\times\overline{B}$ direction, actually executing a cycloidal path [72]

2.2.2 W_f/W_m composite synthesis-chemical vapor deposition

Tungsten has one property similar to ceramics, which is its extremely high melting temperature (3410ºC). Therefore, the CMCs fabrication technologies are good candidates to synthesize W_f/W_m composite.

Cold pressing and sintering, hot pressing (slurry infiltration, hot isostatic pressing (HIP) et al.), reaction bonding processes, infiltration and directed oxidation are the conventional processing techniques of CMCs fabrication. Details can be found in Chawla [58]. Another group of techniques called in situ chemical reaction techniques are also a popular CMCs synthesis process. It mainly refers to chemical vapor deposition (CVD) and chemical vapor infiltration (CVI).

The CVD process involves the dissociation and/or chemical reactions of gaseous reactants in an activated (heat, light, plasma) environment, followed by the formation of a stable solid product. The deposition involves homogeneous gas phase reactions, which occur in the gas phase, and/or heterogeneous chemical reactions which occur on/near the vicinity of a heated surface leading to the formation of powders or films, respectively [76]. The reaction of CVD process can be classed as: pyrolysis, reduction, oxidation, compound formation, disproportionation, and reversible transfer. More details can be found in Ohring [73]. When CVD is used to impregnate large amounts of matrix material in fibrous preforms, it is called chemical vapor infiltration (CVI) [58].

2.2 W_f/W_m composite fabrication

Simply put, during the CVI process a solid material is deposited from gaseous reactants onto a heated substrate. A typical CVD or CVI process would require a reactor with the following parts [58]:

1. A vapor feed system.
2. A CVD reactor in which the substrate is heated and gaseous reactants are fed.
3. An effluent system where exhaust gases are handled.

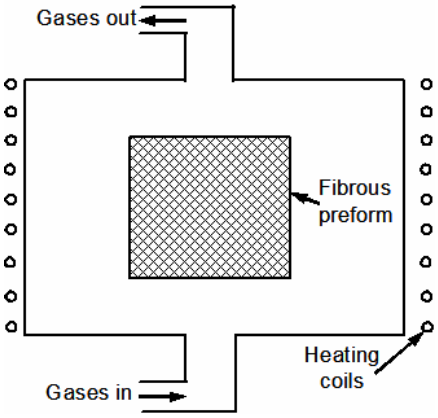

Figure 2.13. Schematic of an isothermal chemical vapor infiltration [58]

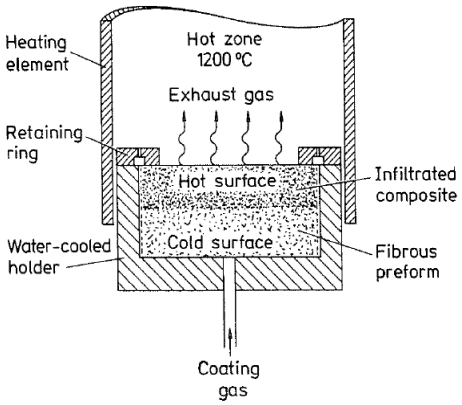

Figure 2.14. Schematic of a chemical vapor infiltration process with pressure and temperature gradients [58]

The basic chemistry to make a bulk ceramic matrix in and around fibers in a preform remains the same. One can synthesize a variety of ceramic matrixes such as oxides, glasses, ceramic, and intermetallics by CVD. Commonly, the process involves an isothermal decomposition of a chemical compound in the vapor form to yield the desired ceramic matrix on and in between the fiber in a preform. Fig. 2.13 shows a schematic of such an isothermal process. Normally, the CVI process is very slow because it involves diffusion of the reactant species products. The CVI process of making a ceramic matrix is, indeed, a kind of low-stress and low-temperature CVD process, and thus avoids some of the problems associated with high-temperature ceramic processing.

Another disadvantage of CVI is, when the CVI process is carried out isothermally, surface pores tend to close first, restricting the impregnation, surface machining, and reinfiltration to obtain an adequate density. Therefore, techniques like forced gas flow or a temperature gradient are applied to avoid this effect. A schematic of one version of this process is shown in Fig. 2.14. A graphite holder in contact with a water-cooled metallic gas distributor holds the fibrous preform. The bottom and side surfaces thus stay cool while the top of the fibrous preform is exposed to the hot zone, creating a steep thermal gradient. The reactant gaseous mixture passes unreacted through the fibrous preform

because of the low temperature. When these gases reach the hot zone, they decompose and deposit on and between the fibers to form the matrix. As the matrix material gets deposited in the hot portion of the preform, the preform density and thermal conductivity increase and the hot zone moves progressively from the top of the preform toward the bottom, when the composite is formed completely at the top and is no longer permeable, the gases flow radially through the preform, exiting from the vented retaining ring.

This variant of CVI, which combines forced gas flow and temperature gradient, avoids some of the problems mentioned earlier. Under these modified conditions, 70% to 90% dense SiC and Si_3N_4 matrices can be impregnated. And the impregnation time can be radically reduced.

As discussed above, the advantages of a CVI technique or any variant thereof include:

Good mechanical properties at high temperature.

Large, complex shapes can be produced in a near-net shape.

Considerable flexibility in the fibers and matrices that can be used (oxide and nonoxide).

Among the disadvantages, one should mention that the process is slow and expensive.

In this thesis, only a single filament composite, which is deposited tungsten matrix on the filament in the center, will be fabricated. The planned tungsten matrix thickness is 1~1.5 mm, the deposition speed and expense is also acceptable. Further more, the matrix with a low inner defect and good mechanical properties deposited by CVD process is best suited to analyze the fundamental interfacial behaviors of W_f/W_m composite. Therefore, CVD is adopted as the fabrication technique for the deposition of W matrix.

Tungsten matrix is deposited using the reduction of tungsten halide in hydrogen at reduced pressure. WF_6 has a lower deposition temperature (550 ºC) than WCl_6 (1000 ºC), and it is used widely as the precursor for the deposition of W films for metallization of ICs (intergrated circuits) to replace Al films [76]. The chemical reaction of the deposition of W matrix is

$$WF_6 + 3H_2 \rightarrow W + 6HF \qquad (2.7)$$

2.3 Interfacial property identification

2.3.1 Push-out test

The fiber push-out test is usually conducted in an instrumented indentation device in which load is applied on one end of the fiber cross section. The load and the fiber end displacement are recorded dynamically producing a characteristic load-displacement

curve which reveals the bonding quality and sliding behavior of the pushed out interface. Fig. 2.15 is the general illustration of a push-out experiment. A push-out test can best reflect the properties of the interface in an actual composite.

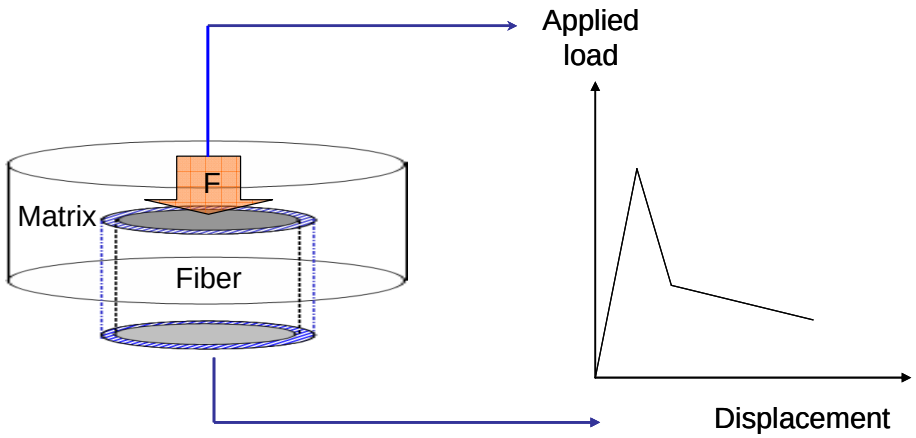

Figure 2.15. Illustration of the push-out process

In the course of the fiber push-out process, the applied load is in equilibrium with the resisting shear stress along the interface. The shear stress is generated by both the chemical (or/and mechanical) bonding and friction at the debonded interface. Generally, an ideal fiber push-out process can be divided into four distinct stages. An illustration of these stages and their corresponding interfacial shear stress distributions are shown in Fig. 2.16 with the corresponding schematic load-displacement curve in Fig. 2.17 [77].

Initially, the applied load increases linearly as the whole specimen undergoes purely elastic deformation (stage 1, until P_i) until the interface begins to fail when the maximum shear stress in the interface reaches the debonding strength τ_d of the interface. The initial debonding location is normally near the free surface of the fiber end (see Fig. 2.16, stage 1) if the fiber embedded length (specimen thickness) is large enough. The parallel direction along the interface is labeled as the z direction. The interfacial shear stress distribution shows an exponential decrease from the maximum value τ_d until it reaches 0 at a certain depth along z direction.

Some researchers [78-80] suggest the presence of a radial stress caused by the thermal expansion coefficient mismatching between the fiber and matrix, namely, the residual stress σ_0, which will generate residual shear stress (τ_0) along the interface according to $\tau_0 = \sigma_0 \times \mu$. Therefore, the residual shear stress exists in the whole process of the push-out test. In Fig. 2.16, σ_0 is indicated while the residual shear stress τ_0 is not presented in the interfacial shear stress distributions. Upon the onset of interface cracking, the total stiffness is reduced which can be observed as a kink in the curve. Sometimes the

deviation of the slope from the initial linearity may not be so conspicuous if the frictional resistance is strong (e.g. due to larger σ_0 or roughness of the debonded interfaces).

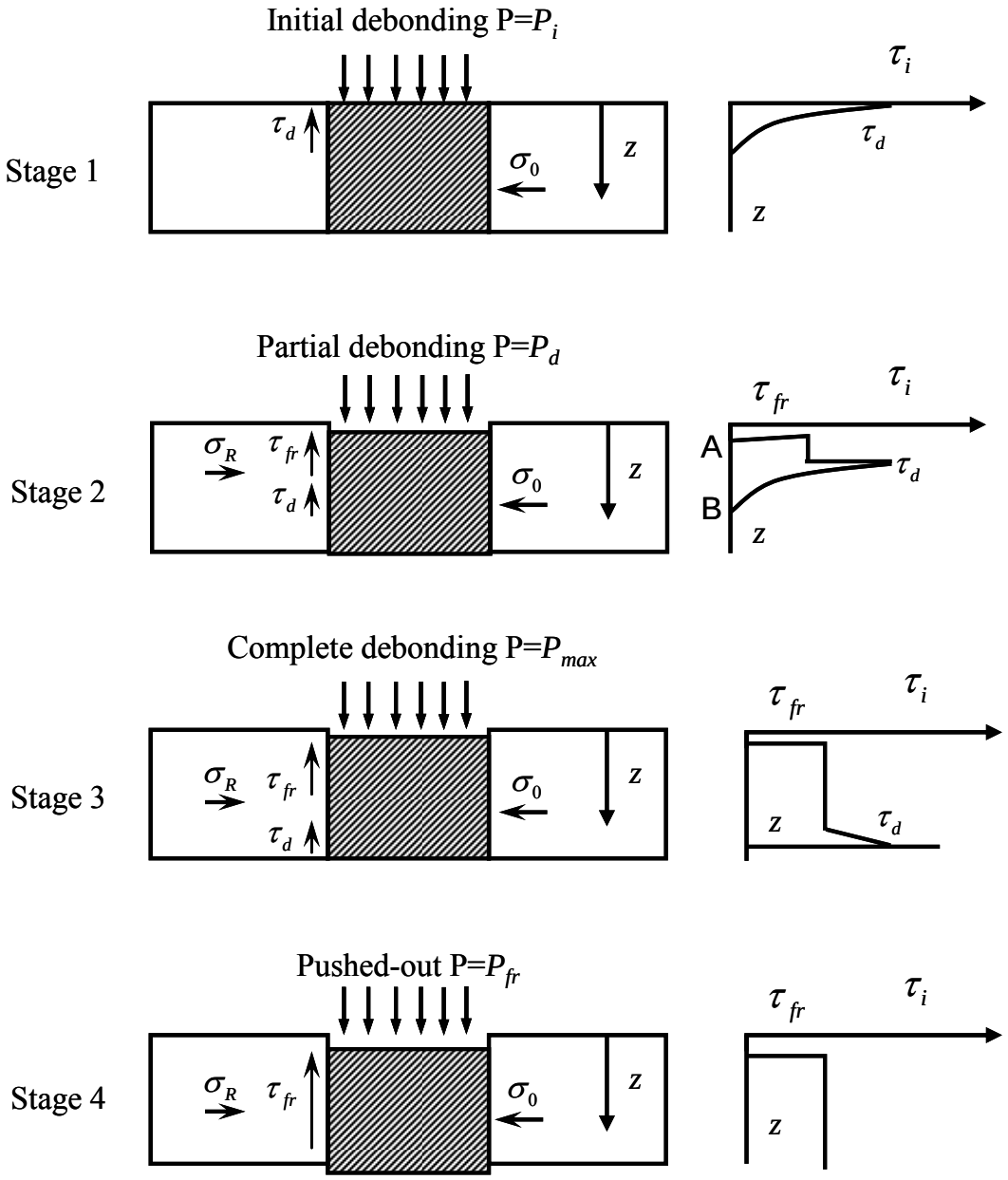

Figure 2.16. Illustration of stages in push-out test process [77]

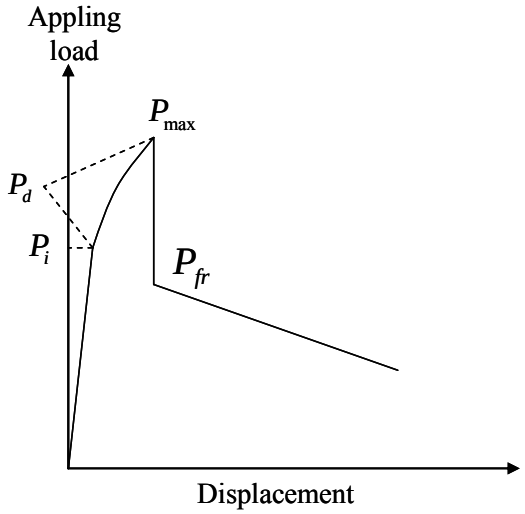

Figure 2.17. Schematic drawing of load-displacement curve in push-out test

Secondly, after the initiation of the cracking, cracking continues to propagate along the whole interface until the interface is completely debonded (stage 2, from P_i to P_d). The interfacial shear stress distribution in stage 2 contains two parts. One is the area which is bearing a steady friction stress (Fig. 2.16, stage 2, from the fiber end until point A) and the other is the area that starts from the debonding (cracking) end (point A), where the interfacial shear stress equals τ_d, until the shear stress decreases to 0 in a certain depth along the z direction (Fig. 2.16, stage 2, point B). The steady friction stress τ_{fr} is normally related to the asperity caused shear stress of the interface τ_R (sometimes associated by the residual shear stress τ_0) and the Poisson effect shear stress τ_P. It can be imagined that along with the debonding propagation, the area which is bearing a steady friction stress will be expanded and point A and point B will be shifted forward along the z direction. During this progressive debonding process, energy is dissipated both by frictional sliding and shear fracture. The applied load in this so-called progressive debonding process is normally called the partial debonding load.

Thirdly, when the crack is propagating close to the other free surface of the specimen, in front of the moving crack tip the shear stress profile has a maximum due to the fracture resistance and the stress concentration caused by free surface edges. As soon as the crack front has swept the full interface, the load drops abruptly since the contribution of the fracture resistance vanishes (stage 3, P_{max}). The applied load at the moment P_{max} is normally called maximum load or complete debonding load.

Finally, after debonding is complete, the fiber is sliding out of the matrix. The applied load is resisted by the friction stress generated along the debonded interface, which

diminishes gradually due to the decrease of the contact area (stage 4, after P_{fr}). The initial sliding load P_{fr} is normally called frictional sliding load.

The fact is that these 4 stages are not easily distinguishable from each other since the micromechanics of the push-out process is quite complicated and is affected by many practical aspects. For example, the initial debonding load cannot be detected if the sliding friction of the debonded interfaces is too large; the progressive debonding process would be not displayed when the cracking propagates very fast, which would be due to the small thickness of the specimen, inner defects of the interface and the stress concentration caused by free surfaces. The recorded displacement of the fiber end can deviate from the actual one due to the bending effects caused by the thin sample thickness.

Here we clarify several terms as follows.

P_i : initial debonding load

P_d : partial debonding load

$P_{\max}$: maximum debonding load

P_{fr} : frictional sliding load

These loads can be read directly from the load-displacement curve of a push-out test. They are strongly related to the interfacial parameters. A lot of effort had been spent to explore the interfacial parameters by interpreting the experimental push-out data within the framework of the theoretical models [85-110]. Some of these models were successfully adopted by many researchers to determine the interfacial fracture behaviors [111-145]. In this work, the interfacial parameters of each interface will be determined by interpreting the push-out data with specific models.

As discussed in chapter 2.1.2.4, the representative parameters of an interface are: the interfacial shear strength τ_d, interface radial stress σ_R, thermal residual stress σ_0, asperity caused shear stress τ_R, friction coefficient μ, and interfacial fracture energy (or critical energy release rate) Γ_i. In the case of the W_f/W_m composites, there exists no thermal residual stress since both the fiber and the matrix are of the same material and the contribution of the thin interface coating to the thermal residual stress may be ignored. Therefore, τ_d, σ_R, τ_R, and Γ_i are the critical parameters to determine the interfacial fracture behavior of the W_f/W_m composites. Their calibration procedures are discussed in the following.

(1) interfacial shear strength τ_d

Greszczuk and Lawrence had developed the earliest model which is related to interfacial shear strength τ_d by using shear-lag assumptions [81-83]. This model indicates that in pull-out test the maximum load $P_{\max}$ has a relationship with the

embedded fiber length L as

$$P_{\max} = \frac{2\pi r_f \tau_d}{\alpha_2} \tanh(\alpha_2 L) \tag{2.8}$$

where $P_{\max}$ is the applied load at the onset moment of interface debonding, r_f is the fiber radius, α_2 is a shear-lag parameter due to the interface shear modulus and thickness, and L is the initially embedded filament length. This equation can also be used for push-out tests by replacing L with the specimen thickness H. τ_d and α_2 can be determined by fitting the experimentally measured $P_{\max}$ - H data with this equation. To this end, extensive push-out tests have to be carried out for the different specimen thicknesses. The least-square method is used to obtain the optimum value of τ_d, leading to the best fit line to the experimental data. The details about the curve fitting principle are shown in Appendix A.

(2) Interface radial stress σ_R, friction coefficient μ, and asperity caused shear stress τ_R

Shetty [84] analyzed the frictional sliding problem using the shear-lag model and derived an equation that related the maximum friction sliding load P_{fr} and the embedded fiber length L:

$$P_{fr} = \frac{\pi r_f{}^2 \sigma_0}{k} [\exp(\frac{2\mu k L}{r_f}) - 1] \tag{2.9}$$

It was assumed that after complete debonding, the applied load P_{fr} was resisted only by the interfacial friction. In Shetty's original formulation, σ_0 denoted the residual clamping stress (normally compressive) due to the thermal expansion mismatch. μ is the friction coefficient at the debonded interface. k, a non-dimensional elastic parameter, $k = E_m \nu_f / [E_m(1-\nu_f) + E_f(1+\nu_m)]$, where ν and E represent the Poisson ratio and Young's modulus, respectively. The subscripts f and m indicate fiber and matrix. r_f is the fiber radius.

In the case of the W_f/W_m composites, σ_0 is neglectable. However, Eq. (2.9) can still find validity for the W_f/W_m composite when the clamping stress σ_0 is reinterpreted as interface radial stress σ_R. In the following we discuss this aspect in detail.

A schematic illustration of a push-out test in the final sliding stage is shown in Fig. 2.18. It is assumed that the applied pressure p is balanced entirely on the frictional shear stress τ_{fr} which can be expressed by the Coulomb friction law

$$\tau_{fr} = \mu \sigma_r \tag{2.10}$$

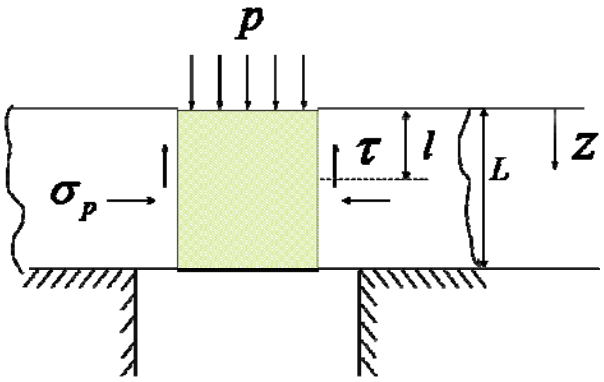

Figure 2.18. Schematic image of stresses distribution of the push-out process

In the absence of a thermal expansion mismatch stress, the (compressive) radial stress σ_r can be regarded as a superposition of the Poisson effect and the interface radial stress σ_R:

$$\sigma_r = \sigma_P + \sigma_R \tag{2.11}$$

The stress contribution due to the Poisson effect σ_P is given by

$$\sigma_P = k\sigma_z \tag{2.12}$$

where σ_z denotes the applied axial stress. In a push-out loading case, σ_P and σ_z are always compressive.

The force equilibrium condition based on the shear-lag model is expressed by

$$-\pi r_f^{\,2} d\sigma_z = 2\pi r_f \tau_{fr} dz \tag{2.13}$$

Substituting Eqs. (2.10), (2.11), and (2.12) into (2.13) and integrating with the boundary condition $\sigma_z = p$ at $z = 0$, one obtains the solution for the fiber axial stress:

$$\sigma_z = \frac{1}{k}(\sigma_R + kp)\exp(-\frac{2\mu kz}{r_f}) - \sigma_R \tag{2.14}$$

For a given applied pressure p, there is a finite fiber length $z = l$ at which the axial stress reduces to zero. This length is defined as the sliding length

$$l = \frac{r_f}{2\mu k}\ln(\frac{\sigma_R + kp}{\sigma_R}) \tag{2.15}$$

When the sliding length l is equal to the full embedded depth L, the applied load reaches its maximum–then the maximum load P_{fr} is given by the following equation which has a identical form as the Shetty's original solution except for the σ_R term:

2.3 Interfacial property identification

$$P_{fr} = \frac{\pi r_f{}^2 \sigma_R}{k}[\exp(\frac{2\mu kL}{r_f}) - 1] \tag{2.16}$$

To this end, σ_R and μ can be determined by curve fitting, by using the exponential relationship based on the measured P_{fr} - L data.

(3) Interfacial fracture energy Γ_i

Liang and Hutchinson [80] developed a model to estimate the interfacial fracture energy under push-out loading (mode II) which is expressed as

$$p_d = p_R + 2\sqrt{\frac{G_i E_f}{B_2 r_f}} e^{\xi} + \frac{\tau_0}{\mu B_1}(e^{\xi} - 1) \tag{2.17}$$

where

$\xi = 2\mu B_1 l / r_f$,

$B_1 = E_m \nu_f / [E_m(1-\nu_f) + E_f(1+\nu_m)]$,

$B_2 = 1 - 2\upsilon_f B_1$.

l denotes the fully embedded fiber length which is equal to specimen thickness H, while μ is the friction coefficient, τ_0 is the residual shear stress which is replaced by asperity caused shear stress τ_R in this work, G_i denotes the interfacial fracture energy under shear debonding mode which is assumed to be equal to Γ_i in this work , and p_d is the peak applied stress on the fiber which is equal to the maximum debonding load $P_{\max}$ divided by the cross section area of the fiber: $p_d = P_{\max} / \pi r_f^2$, p_R is the residual axial stress which is negligible for the W_f/W_m composite. Hence Eq. (2.17) can be simplified to

$$p_d = 2\sqrt{\frac{\Gamma_i E_f}{B_2 r_f}} e^{\xi} + \frac{\tau_R}{\mu B_1}(e^{\xi} - 1) \tag{2.18}$$

The second term in the Eq. (2.18) is exactly the transformative form of Eq. (2.16). The first term stands for the contribution of the interfacial fracture energy to the debonding resistance. It is possible to calibrate the value of Γ_i by means of the curve fitting method using Eq. (2.18) based on experimental p_d - H data when τ_R and μ are known.

At first glance, it may seem sensible to make a curve fitting using Eq. (2.16) to determine τ_R and μ, then make a curve fitting with Eq. (2.18) to obtain Γ_i. However, since these two theoretical models describe the interfacial properties on an equal footing,

there is no prerequisite to which parameter should be estimated first. Therefore, it is necessary to make a curve fitting on these two equations simultaneously.

To this end, a special curve fitting process–Bayesian parameter estimation with uniform priors based on so called rejection posterior sampling was applied. The interfacial parameters σ_R, μ, and Γ_i were obtained simultaneously. The details about the curve fitting program can be found in Appendix A.

Alternatively, Clyne [143] suggested an alternative model for the interface fracture energy based on an energy balance approach. This model yields a relationship between Γ_i and p_d:

$$\Gamma_i = \frac{r_f}{4E_f}\left(\left(p_d - \sigma_{z,\Delta T} \right) e^{-\frac{2\mu B_1 H}{r_f}} + \frac{\tau_{0,\Delta T}}{\mu B_1}(e^{-\frac{2\mu B_1 H}{r_f}} - 1) \right)^2 \tag{2.19}$$

where $\sigma_{z,\Delta T}$ represents the thermal mismatch radial stress, and $\tau_{R,\Delta T}$ is the total shear stress consisting of the asperity caused shear stress τ_R and the thermal mismatch stress $\tau_{\Delta T}$. Since the $\tau_{\Delta T}$ term is negligible in the present case, Eq. (2.19) reduce to

$$\Gamma_i = \frac{r_f}{4E_f}\left(p_d e^{-\frac{2\mu B_1 H}{r_f}} + \frac{\tau_R}{\mu B_1}(e^{-\frac{2\mu B_1 H}{r_f}} - 1) \right)^2 \tag{2.20}$$

Eq. (2.20) has exactly the same form as Eq. (2.18) except for the B2 factor. In Eq. (2.20), p_d and H can be read directly from the push-out test results, while μ and τ_R can be obtained through curve fitting. Therefore, Γ_i is calculable. Each specimen with a specific thickness can produce one Γ_i value. The average value represents the mean fracture energy of the interfaces.

Based on the obtained interfacial fracture energy, one can predict the crack deflection of the W_f/W_m composites, regarding the interfacial debonding criteria as discussed in chapter 2.1.2.3.

2.3.2 Push-back test

The push-back test is normally carried out on the specimen after a push-out test. In a push-back test, the load is applied at the opposite end (pushed out end) of the fiber on the specimen, the load and indenter displacement are recorded, generating a load-displacement curve, which indicates the friction contribution of the interface topography of the pushed out (debonded) interface. Several publications show that the push back test is helpful to analyze the radial stress caused by interfacial geometry mismatch (roughness) [146-148].

Figure 2.19 is a schematic drawing of an interface region in the fiber-reinforced composite. Before being pushed (debonding), the irregularies on the fiber and matrix are perfectly matching (Fig. 2.19 a). After the debonding event, as the fiber moves, the surfaces' misalignment causes a radial displacement of the matrix resulting in a compressive radial stress at the interface (Fig. 2.19 b). This compressive radial stress increases the frictional sliding stress of the interface, which eventually leads to an increase of the longitudinal applied load during push-out (back) process. When the pushed out specimen is subjected to a push-back test, the fiber is pushed back into its original position. When the fiber reaches the exact original place, the irregularities on the fiber and the matrix surface realign and the friction associated with the misfit of these irregularities vanishes. The longitudinal applied load would drop at this moment. As the fiber passes its original position, the surfaces begin again to deviate from their alignment and the load (friction) rises. Fig. 2.20 shows a push-back load-displacement curve detected by Jero and Kerans [146], which shows the seating process. The seating phenomenon began with an abrupt drop as the fiber began to traverse its origin, which was followed by a rise to a peak above the initial value then a return to almost the initial level.

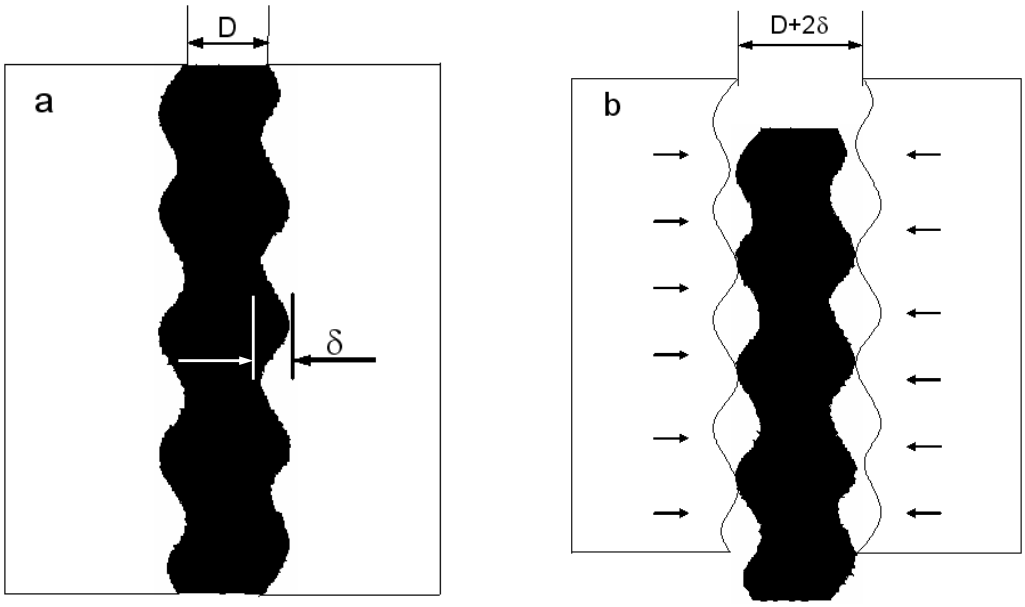

Figure 2.19. Schematis of an interface region: a) before debonding; b) after debonding [146]

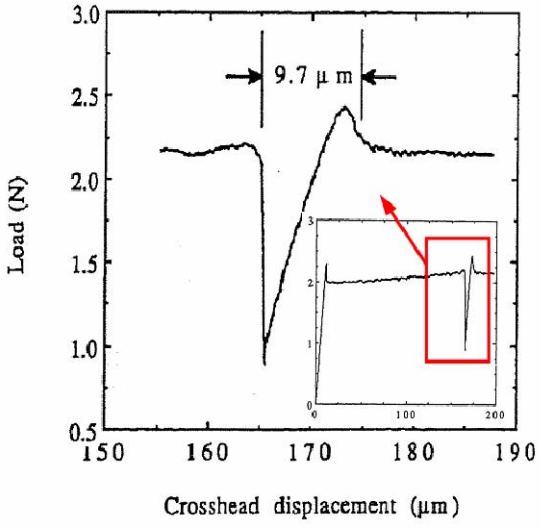

Figure 2.20. Push-back curve (reseat drop phenomenon) [146]

Further, apart from the "dropping gap" region, the rest part of the push-out (back) curve is also interesting. Cherouali [148] did analysis on "go and return" test (repeating push-out&back test). The interesting point of this result is that, the serrations of the curves progressively disappeared; this phenomenon is thought to be due to the abrasion of the surface roughness during the repeated sliding process. In this work, push-back test was applied as well.

2.3.3 Micromechanical test-three point bending test

In order to directly observe the interfacial debonding behavior, one miniaturized three-point bending (3PB) device was employed to provide the visual information about the crack deflecting along the interface when the interface was bearing a tensile load. Specimen with lengths from 4 mm to 30 mm can be tested using this 3PB device. This device consists of 3 main parts: loading supply system, which can provide a load up to 500 N; load-displacement recording system, which can record the values of the applied load and the displacement for calculating the fracture toughness of the specimen; an in-situ imaging system, to show the pictures of real time fracture behavior of the specimen. The in-situ imaging function is very important for this work, since it provides the possibility to observe the interfacial debonding behavior. When the sample is prepared as a half cylinder with half fiber in the half matrix, the interface between the fiber and matrix is visible. By setting a pre-cracking in the matrix and applying the load, the crack propagation along (or through) the interface is visible by utilizing the in-situ imaging. Fig. 2.21 shows the specimen holder of the device and the optimized design geometry of the testing sample.

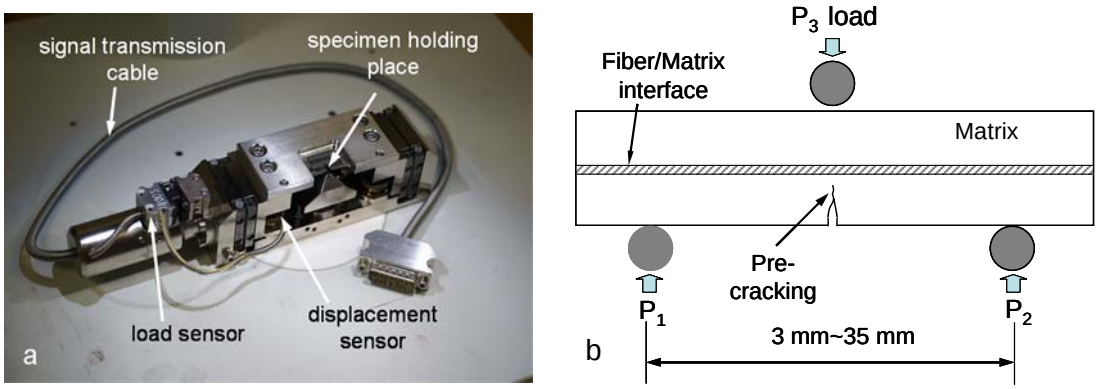

Figure 2.21. 3PB test equipment. a) image of the specimen holder of the 3PB device; b) designed geography of the testing sample, shaded part in the middle of the specimen is the fiber

2.4 Mechanical property prediction of composite with multiple fibers

When the properties of the fiber, matrix and interface are available, the mechanical properties of a composite with multiple fibers are predictable. Therefore, apart from the interfacial debonding criterion verification and the direct crack deflection observation, one can predict the mechanical property of W_f/W_m composites with multiple fibers based on the obtained interfacial parameters. The most important mechanical behavior for a composite is the stress-strain curve. As shown in Fig. 2.4 a, a typical stress-strain curve of the toughened composite contains following critical quantities:

1. σ_{mc} : matrix cracking stress
2. σ_{sat} : matrix cracking saturation stress
3. σ_y : composite yielding stress (requires fiber yielding stress $\sigma_{f-yield}$)
4. σ_u : composite ultimate stress (requires fiber ultimate stress σ_{f-u})

and their corresponding strains.

Therefore, the stress-strain curve of W_f/W_m composites can be predicted after estimating these quantities. The procedures are described in follows.

(1) Matrix cracking stress σ_{mc}

Considering an unidirectionally-aligned-fiber composite under tension containing a long matrix crack normal to the fiber direction, On can analyze the fiber-matrix interaction on the basis of a single composite cylinder. Fig. 2.22 shows the schematic image of the fiber and matrix [149]. Here, r_f is the fiber radius, c_f and c_m are the fiber and the matrix volume fractions, respectively, satisfying $c_f + c_m = 1$. A uniform axial strain is imposed at $z = \infty$, producing the far-field average fiber and matrix stresses

σ_f^∞ and σ_m^∞. Thus, the average composite stress $\sigma = c_f\sigma_f^\infty + c_m\sigma_m^\infty$ is resisted by the fiber stress σ / c_f at the matrix crack. Axial sliding occurs at the fiber-matrix interface in the interval $0 < z < l$, where the longitudinal shear stress is equal to the limiting frictional stress. This stress is caused by the asperity caused shear stress τ_R in the W_f/W_m composite. The magnitude of l, which could be zero, will come out from the solution.

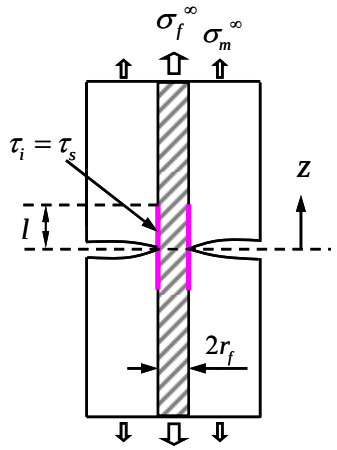

Figure 2.22. Single composite cylinder model, fiber and matrix [149]

According to the shear-lag solution, the average fiber and matrix tensile stresses $\sigma_f(z)$ and $\sigma_m(z)$, as well as the interface shear stress $\tau_i(z)$, are given in references [149, 150]:
for $0 < z < l$

$$\sigma_f(z) = \sigma / c_f - 2\tau_R z / r_f$$

$$\sigma_m(z) = (2c_f / c_m)\tau_R z / r_f$$

$$\tau_i(z) = \tau_R \tag{2.21}$$

for $z > l$

$$\sigma_f(z) = \sigma_f^\infty + \left[(c_m / c_f)\sigma_m^\infty - 2\tau_R l / r_f\right] e^{-\rho(z-l)/r_f}$$

$$\sigma_m(z) = \sigma_m^\infty - \left[\sigma_m^\infty - (2c_f / c_m)\tau_R l / r_f\right] e^{-\rho(z-l)/r_f}$$

$$\tau_i(z) = (\rho / 2)\left[(c_m / c_f)\sigma_m^\infty - 2\tau_R l / r_f\right] e^{-\rho(z-l)/r_f} \tag{2.22}$$

2.4 Mechanical property prediction of composite with multiple fibers

$$\rho = \left[\frac{2\zeta_m E_c}{c_m E_m E_f \log(\overline{R}/r_f)} \right]^{1/2},$$

$$\overline{R} = R - r_f \approx r_f / \sqrt{c_f} .$$

Here, ζ_m is the matrix shear modulus, $\zeta_m \approx E_m / [2(1+\nu_m)]$. ν_m is the matrix Poisson ratio; E_c is the Young's modulus of the composite, E_f and E_m are Young's modulus of the fiber and matrix, respectively; $\overline{R}$ is the effective matrix radius and R is the composite radius.

Two definitions are made:

1) sliding stress σ_S: applied stress which leads the interfacial shear stress at $z = 0$ reaches interfacial friction stress τ_{fr} (in W_f/W_m composite case $= \tau_R$).

Assuming the debonding energy to be 0, the debonded length l will remain equal to zero until the interface shear stress at $z = 0$ reaches the interfacial friction stress τ_R. This will happen when the applied stress σ reaches a critical value, σ_S. Appling $\sigma = \sigma_S$, $\tau_i(z) = \tau_R$, $z = 0$, and $l = 0$ to Eq. (2.22), One can get

$$\sigma_S = \left(\frac{2c_f E}{c_m E_m} \right) \frac{\tau_R}{\rho}.$$

2) debonding stress σ_D: in the frictionless case, the debonded zone is propagating under a critical value σ_D of the average applied stress σ at $z = \infty$. An elementary energy release calculation gives

$$\sigma_D = 2c_f \sqrt{\frac{E_f E_c \Gamma_D}{c_m E_m r_f}} .$$

where Γ_D is the debonding energy release rate (equal to the interfacial fracture energy Γ_i in W_f/W_m composite). Its corresponding interfacial shear stress is known as the cohesive shear strength of the interface τ_D.

$$\tau_D = \left(\frac{\rho c_m E_m}{2c_f E_c} \right) \sigma_D .$$

A general criterion for continued interface debonding with both friction and debonding energy is formulated as follows.

In order to propagate the debonding, the interfacial shear stress $\tau_i(l^+)$ at the debonding front needs to be $\tau_i(l^+) = \max(\tau_R, \tau_D)$. In the W_f/W_m composite case, $\tau_D > \tau_R$. Therefore, one can set $\tau_i(l^+) = \tau_D$ in Eq. (2.22) in order to calculate the debonding length l, arriving at

$$l/a = \left(\frac{c_m E_m}{c_f E}\right)\frac{\sigma - \sigma_D}{2\tau_R} \tag{2.23}$$

The matrix-cracked composite (see Fig. 2.23) is stretched uniformly at $z=\pm L'$ by an average stress σ. The same stress is applied to the spring model which consists of two homogenous slabs with the composite modulus E_c, connected by a spring that stretches by 2υ.

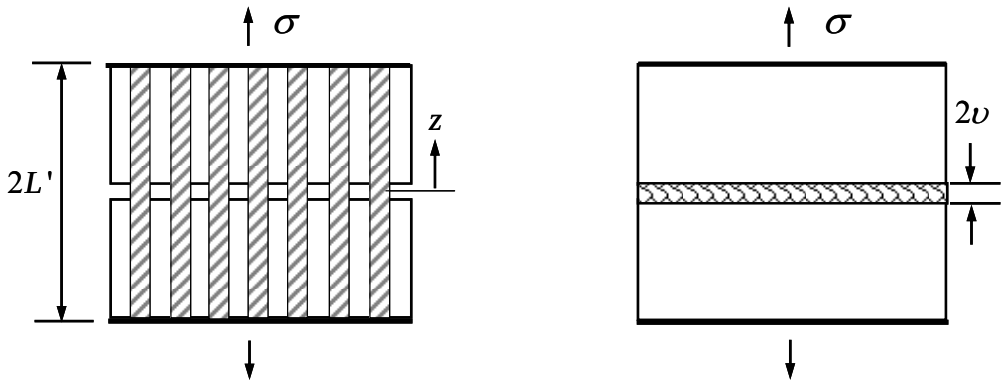

Figure 2.23. Fiber bridging prototype and spring model; the average applied stress is σ [149]

To allow for the identical final displacements in the model and the prototype, the spring stretch must satisfy

$$\upsilon = \int_0^{L'} \frac{\sigma_f(z)}{E_f} dz - \frac{\sigma L'}{E_c} \tag{2.24}$$

Applying Eqs. (2.21), (2.22), and (2.23) into Eq. (2.24), assuming $L' \to \infty$, one gets

$$\frac{\upsilon}{r_f} = 2\left(\frac{\sigma_S}{\sigma_A}\right)\left(\frac{\sigma}{\sigma_A}\right) \qquad \text{for } \sigma \le \sigma_D \tag{2.25a}$$

$$\frac{\upsilon}{r_f} = \left(\frac{\sigma}{\sigma_A}\right)^2 - \left(\frac{\sigma_D}{\sigma_A}\right)^2 + 2\left(\frac{\sigma_S}{\sigma_A}\right)\left(\frac{\sigma_D}{\sigma_A}\right) \qquad \text{for } \sigma \ge \sigma_D \tag{2.25b}$$

with $\sigma_A = \dfrac{2c_f E_c \sqrt{E_f \tau_R}}{c_m E_m}$.

The matrix cracking stress σ_{mc} is defined as the value of the far-field average stress σ needed to propagate a single, long matrix crack through the composite, and is readily obtained by setting the crack front energy release rate $c_m \Gamma_m$ equal to the rate of potential energy loss in the composite as the crack front advances. The potential energy release per unit crack advance is

$$Q(\sigma) = 2\int_0^{\sigma} \upsilon(\sigma) d\sigma \tag{2.26}$$

Combining Eq. (2.25) and Eq. (2.26) gives

$$Q(\sigma) = \frac{2r_f}{\sigma_A}[\sigma_S \sigma^2] \qquad \text{for } \sigma < \sigma_D \tag{2.27a}$$

$$= \frac{2r_f}{3\sigma_A^{\,2}}\left[\sigma^3 - 3\sigma\sigma_D(\sigma_D - 2\sigma_S) + \sigma_D^{\,2}(2\sigma_D - 3\sigma_S)\right] \qquad \text{for } \sigma > \sigma_D \tag{2.27b}$$

This is actually the complementary energy of the springs, and the matrix cracking stress σ_{mc} satisfies

$$Q(\sigma_{mc}) = c_m \Gamma_m \tag{2.28}$$

Combining Eqs. (2.27b) and (2.28) (with σ_{mc} larger than σ_D) one can obtains

$$\frac{2r_f}{3\sigma_A^{\,2}}\left[\sigma_{mc}^{\,3} - 3\sigma_{mc}\sigma_D(\sigma_D - 2\sigma_S) + \sigma_D^{\,2}(2\sigma_D - 3\sigma_S)\right] = c_m \Gamma_m \tag{2.29}$$

By solving Eq. (2.29), one can get the values of σ_{mc} for the W_f/W_m composite with each interface. The corresponding strain ε_{mc}, can be calculate by

$\varepsilon = \dfrac{\sigma_{mc}}{c_f E_f + c_m E_m}$.

(2) Matrix cracking saturation stress σ_{sat}

As multiple matrix cracking develops, the slip zones of neighboring cracks overlap and produce a shielding effect. When the shielding process is completed, a saturation crack density results. This occurs at a stress σ_{sat}, with an associated spacing $\overline{l_S}$ given by [45]

$$\overline{l_S}/r_f = \chi\left[\Gamma_m (1-c_f)^2 E_f E_m / c_f \tau_R^{\,2} E_c r_f\right]^{1/3} \tag{2.30}$$

where χ is the crack coefficient. It depends on the arrangement of the cracks (period, random, etc.); and was suggested to be 1.6 [45].

$$\sigma_{sat} = \frac{c_f E_c (\tau_R \overline{l_S} / r_f)}{(1-c_f) E_m} \tag{2.31}$$

The corresponding strain can be calculated via $\varepsilon_{sat} = \sigma_{sat} / c_f E_f$, since at that moment, the applied stress is resisted by the fiber.

(3) Composite yielding stress σ_y

The composite yielding stress is defined as a stress where the composite starts to fail. At this moment, cracks propagate through the entire matrix; the stress is sustained by the fibers. Therefore, the composite yielding stress is given by $\sigma_y = c_f \sigma_{f-yield} + \sigma_S$. The corresponding strain can be calculated by $\varepsilon_y = \sigma_{f-yield} / E_f$.

(4) Composite ultimate tensile strength σ_u

σ_u is steered by the fiber ultimate stress σ_{f-u} since the fiber is bearing the whole load at the failure stage. Hence the ultimate stress can be obtained by $\sigma_u = c_f \times \sigma_{f-u}$ and the ultimate strain is the failure strain of the W fiber.

2.5 Structure characterization method

2.5.1 Interface morphology characterization, SEM equipped with FIB

A high magnification scanning electron microscope (SEM), detecting secondary electrons (SE) and backscattered electrons (BSE), serves as a high resolution technique for studying the morphology and grain topography. With the additional feature of energy dispersive x-ray spectroscopy (EDXS), the composition of the surface structure can be determined. SEM images rely on imaging surfaces and 3D structures of the sample due to the high depth of the field and the brightness of tilted surface [73, 151].

The focused ion beam (FIB) uses a focused beam (beam size 4-6 nm) of gallium ions accelerated to an energy of 1-30 keV to sputter atoms from the substrate. Because the beam position, dwell time and size are well controlled, it can be applied to remove material locally in an accurately controlled manner, down to the nanometer scale. The FIB in combination with SEM is a great innovation in microscope technology. First, the FIB is used to cut and mill the desired location of the specimen, and then SEM images are taken. These images show the fresh section of the specimen and avoid any inaccurate

information cause by the damage from mechanical polishing, which happens quite often in conventional polishing technology. Besides which the cutting location is flexible, it can reveal the structure of a specific area, which is extremely convenient to analyze the interface between fiber and matrix. In this thesis, SEM images obtained after FIB processes are intensively used to demonstrate the microstructure of the interfaces.

2.5.2 Interface chemical characterization, EDXS, SIMS

Energy dispersive x-ray spectroscopy (EDXS) is an analytical technique used for the elemental analysis or chemical characterization of a sample. As a type of spectroscopy x-rays emitted by the sample in response to being hit with charged particles are analyzed with respect to their energy. Its characterization capabilities are due to the fact that each element has a unique electronic structure allowing x-rays that are characteristic of an element's atomic structure to be identified.

Most EDXS analysis systems are combined with SEM. The electron beam serves to excite characteristic x-rays from the area of the specimen being probed; a detector is used to convert the x-ray energies into voltage signals; this information is sent to a pulse processor, which measures the signals and passes them onto an analyzer for data display and analysis. In this thesis, SEM-EDXS analysis is used to detect the elemental composition of the interface.

Secondary ion mass spectrometry (SIMS) is a technique used in materials science and surface science to analyze the composition of solid surfaces and thin films by sputtering the surface of the specimen with a focused primary ion beam and collecting and analyzing ejected secondary ions. These secondary ions are measured with a mass spectrometer to determine the elemental, isotopic, or molecular composition of the surface. The SIMS primary ion beam can be focused to less than 1 μm in diameter. Controlling where the primary ion beam strikes the sample surface provides the microanalysis. SIMS has the ability to provide chemical information on polymers and composites by detection of ionized fragments [62]. In this thesis, the SIMS profile was adopted to investigate the chemical compositions of magnetron sputtering deposited interface coatings.

Chapter 3

Material and Experiment

3.1 Material

3.1.1 Fiber

Commercial tungsten (W) wire (see Fig. 3.1 a) was used as the reinforcement (fiber). The material parameters of W fiber are shown in Table 3.1.

Table 3.1. Material parameters of W fiber.

Diameter, d_f (μm)	Fracture energy, Γ_f (J/m^2)	Young's modulus, E_f (GPa)	Poisson ratio, ν_f	Yield strength, $\sigma_{f-yield}$ (MPa)	Ultimate strength, σ_{f-u} (MPa)	Ultimate strain, ε_{f-u} (%)
150	360	400	0.28	1727	2593	2.1

The fracture energy of the W fiber was taken from reference [152]: the fracture toughness K_f of the commercial W wire is about 12-14 MPa·m$^{1/2}$. It can be converted into fracture energy via $\Gamma_f = K_f^2 / E_f$ with E_f =400 GPa, yielding a value of 360 J/m^2.

The yield strength, the ultimate strength, and the ultimate strain of fiber were obtained by a tensile test. These values are comparable to the literature data [152-154].

3.1.2 Interface

The interface of W_f/W_m composites were deposited by magnetron sputter deposition. The W fiber was wound on a stainless steel frame (Fig. 3.1 b) with a spacing of 3 mm to avoid coalescence during deposition. The wound frames were cleaned in an ultrasonic acetone bath. Then the complete frames were coated in a magnetron sputtering device with varying interface materials (Fig. 3.1 c). Every frame was pre-sputtered for cleaning by an argon (Ar) plasma. Also the sputter targets were pre-cleaned with a closed shutter. The oxide coatings were deposited by the introduction of oxygen as a reaction partner for the sputtered metal atoms. The oxidation reactions are as follows:

$$Zr + O_2 \rightarrow ZrO_x \quad (3.1)$$

$$Er + O_2 \rightarrow ErO_x \quad (3.2)$$

Since the deposited oxide coatings are non-stoichiometric containing unknown oxygen content they are labeled ZrO_x and ErO_x instead of ZrO_2 and Er_2O_3.

With every interface deposition a cleaned piece of a silicon wafer was placed beside the frame. This reference coating provides the information about its corresponding interface.

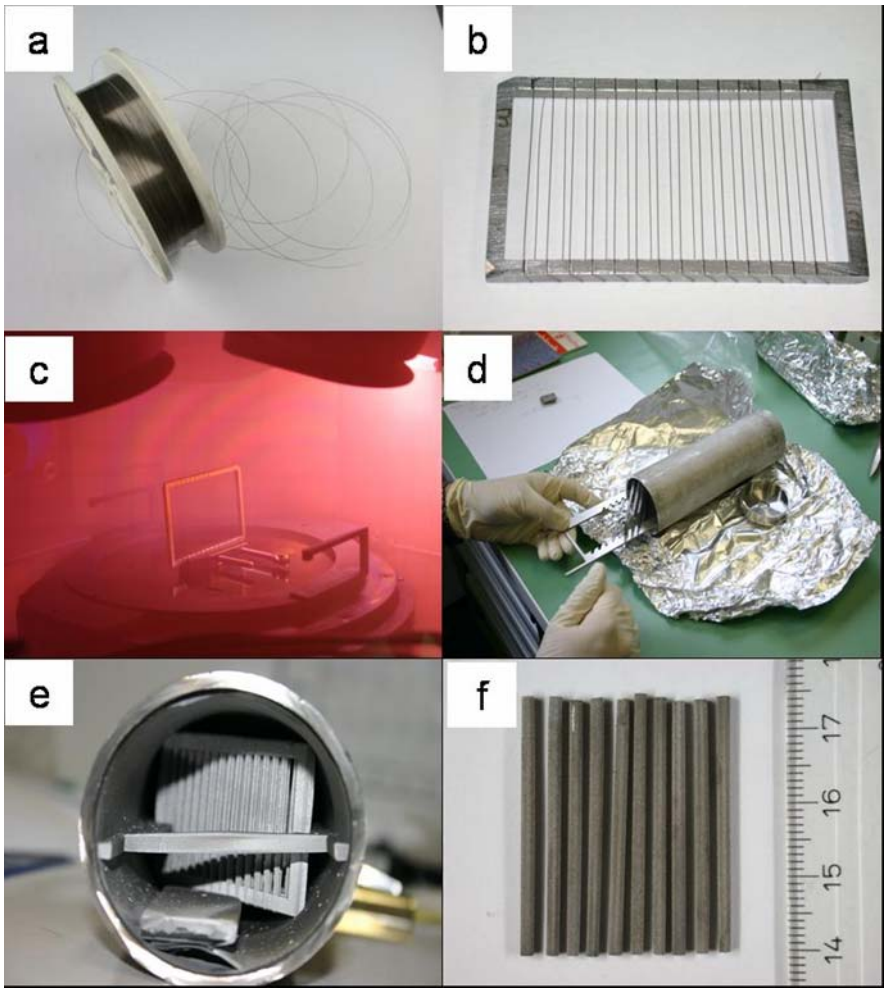

Figure 3.1. W_f/W_m composite synthesization process: a), commercial W wire; b), W wire wound on frame; c), interface was deposited by magnetron sputtering; d), frames were emplaced in the chamber; e), frames after CVD deposition; f), W_f/W_m composites

Some interfaces were deposited with an additional 100 nm W layer to protect the coating from oxidation (eg. The ZrO_x/Zr m, the Cu 480, the carbon, etc…interfaces).

Table 3.2 shows the information of the layer arrangement and deposition condition of each interface.

Table 3.2. Interface arrangement and depositing condition: the diameter of the targets is 15 cm; the background chamber pressure is 5×10^{-6} Pa; the rotation speed of the substrate holder is 6 upm. *: Gas Severing indicates the injected gas and amount; Power supply indicates the plasma creation and substation source; Pressure indicates the chamber pressure during the deposition; Voltages was the power supply of the magnetron sputtering device.

Interface name	Layer arrangement: material and thickness (nm)	Depositing conditions*				Total interface thickness (nm)
		Gas Serving (sccm)	Power supply	Pressure (Pa)	Voltage, DC (V)	
ZrO_x 150	ZrO_x , 150	Ar 160 O_2 10	600 W bipulse	0.67	405	150
ZrO_x 450	ZrO_x , 450	Ar 160 O_2 10	600 W bipulse	0.47	405	450
ZrO_x 950	ZrO_x , 950	Ar 60 O_2 10	600 W bipulse	0.46	405	950
ZrO_x&W 260	ZrO_x, 125	Ar 10 O_2 6	300 W RF, bias: 20 V	0.58	296	260
	W , 130	Ar 40	300 W DC	1.8	387	
ErO_x 600	ErO_x , 600	Ar 160 O_2 10	600 W bipulse	0.46	467	600
ErO_x 1000	ErO_x , 1000	Ar 160 O_2 10	600 W bipulse	0.46	463	1000
ZrO_x/Zr m	ZrO_x , 55×5	Ar 10 O_2 6	300 W RF, bias: 20 V	0.58	301	640
	Zr , 35×5	Ar 10	200 W RF, bias: 20 V	0.33	286	
	W , 190	Ar 40	300 W DC	1.9	393	
ZrO_x/W m	ZrO_x , 100×5	Ar 160 O_2 10	600 W bipulse	0.47	405	900
	W , 100×4	Ar 160	300W DC	0.46	407	
ErO_x/W m	ErO_x ,100×5	Ar 160 O_2 10	600 W bipulse	0.47	455	900
	W , 100×4	Ar 160 O_2 10	300 W DC	0.46	401	
Er/W m	Er , 100×4	Ar 20	500 W DC	0.93	390	900
	W , 100×5	Ar 20	500 W DC	0.93	430	

Table 3.2. (continue).

Interface name	Layer arrangement: material and thickness (nm)	Depositing conditions*				Total interface thickness (nm)
		Gas Serving (sccm)	Power Suppy	Pressure (Pa)	Voltage, DC (V)	
Cu/W m	Cu , 55×4	Ar 20	500 W DC	0.93	400	770
	W , 110×5	Ar 20	300 W DC	0.93	470	
Cu 170	W , 100	Ar 20	500 W DC	0.93	400	370
	Cu , 170	Ar 20	300 W DC	0.94	470	
	W , 100	Ar 20	500 W DC	0.93	400	
Cu 480	W , 100	Ar 20	500 W DC	0.93	400	680
	Cu , 480	Ar 20	300 W DC	0.94	470	
	W , 100	Ar 20	500 W DC	0.93	400	
carbon (C) quadplex	C , 100	Ar 20	200 W DC	0.95	750	1050
	W , 150	Ar 20	500 W DC	0.93	390	
	C , 600	Ar 20	500 W DC	0.95	750	
	W , 200	Ar 20	500 W DC	0.93	390	

In Table 3.2, the numbers after the coating names refer to the thicknesses of each interface and the “m” behind the coating names indicates that they are multilayer structures. For example, ‘ZrO_x 150’ means that it has a single layer structure and its thickness is 150 nm; ‘ZrO_x/Zr m’ means that it has a multilayer structure and contains the alternating ZrO_x and Zr layers (5 ZrO_x layers and 5 Zr layers, see Fig. 3.2).

The microstructure images of each deposited interface are shown and discussed in chapter 4.1.

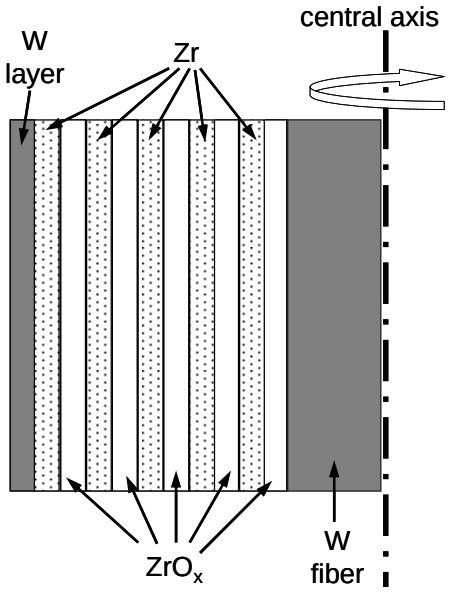

Figure 3.2. The designed layer arrangement of ZrO_x/Zr m interface

3.1.3 Matrix

The matrix was deposited via chemical vapor deposition (CVD) by Archer Technicoat Ltd., England.

The frames after interface deposition were placed in a specially designed tube (Fig. 3.1 d) for the W matrix deposition. The tube had two pipe connections on the opposite ends as inlet and outlet for the reactive gases. The gas flow direction was alternated frequently during the deposition for a more homogeneous coating along the assembly. Tungsten hexafluoride (WF_6) as the tungsten precursor and hydrogen are guided through the reaction chamber which was heated to a temperature of 550 °C. The chemical reaction of the process is

$$WF_6 + 3H_2 \xrightarrow{550\,^{\circ}C} W + 6WF \tag{3.3}$$

After a processing time of 30 hours a W layer with a thickness of 1-1.5 mm was deposited on the fibers. The assembly was carefully cut open by wire erosion (Fig. 3.1 e). From every frame originated 35 mm long W_f/W_m sticks (Fig. 3.1 f) with the same nominal interface between fiber and matrix.

The material parameters of the W matrix are shown in Table 3.3. The density of W matrix was measured by Archimedes method. The fracture energy is calculated by a three point bending test (see chapter 4.4.2). The optical microscopy images (see Fig. 3.3) of W matrix shows that the CVD-deposited W matrix is dense and without any pores.

Table 3.3. Material parameters of W matrix deposited by CVD.

Density (g/cm^3)	Fracture energy, Γ_m (J/m^2)	Young's modulus, E_m (GPa)	Poisson ration, ν_m
19.3±0.2	114	400	0.28

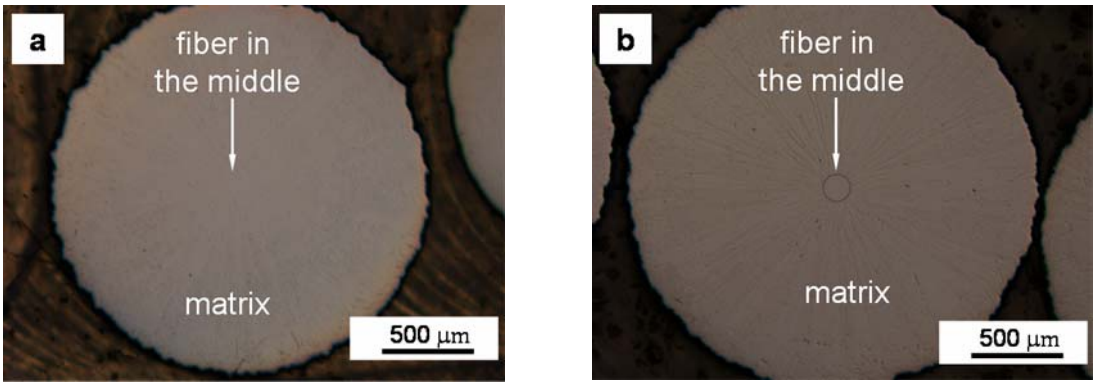

Figure 3.3. Top-views of a W_f/W_m composite specimen: a) grinded by 2 µm-grinding paste; b) lightly etched by potassium ferricyanide ($K_3[Fe(CN)_6]$) solution

3.2 Testing specimen preparation

3.2.1 Push-out (back) test specimen preparation

The push-out test was carried out utilizing a cylindrical tungsten carbide punch (diameter of 120 µm) as indenter to apply the load. The tungsten carbide punch had the maximum applicable load of 65 N and thus limited the specimen thicknesses below 0.35 mm. In order to prepare such thin specimens, the W_f/W_m composites were cut into thin slices by a diamond saw. These slices were then glued on to a specially designed polishing holder that had a stepped surface with a difference of 50 µm per step. It allowed for the preparation of the polished samples with a difference in thickness of 50 µm. The samples were glued with a polymer wax which can easily be dissolved in propanone without any damage to the polished surface. The slices were polished on both sides.

In order to clearly identify the interface location, the polished surfaces were slightly eroded by Potassium ferricyanide (K_3 [Fe(CN) $_6$]) solution (see Fig. 3.3 b).

Figure 3.4 is a schematic drawing of the push-out test specimen.

The pushed out samples were turned upside down with the protruded fiber carefully placed under the punch in order to carry out the push-back tests.

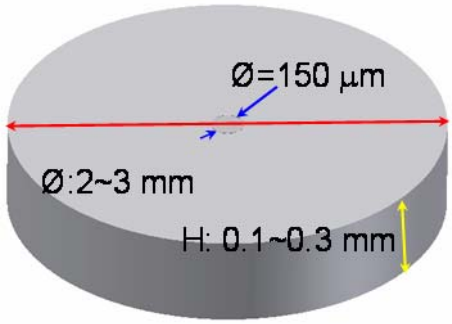

Figure 3.4. Schematic drawing of a push-out test specimen

3.2.2 Three point bending test specimen preparation

Figure 3.5 shows the process of preparing the three point bending (3PB) test specimens. Firstly, the W_f/W_m composite was cut into a cylinder with the length of 5 mm (Fig. 3.5 a); after that, the material of the up and downside of the cylinder was polished away resulting in two parallel planes (Fig. 3.5 b); subsequently, half of this cylinder was precisely removed by polishing under 90 degree to the applied planes with exactly half of the fiber remaining (Fig. 3.5 c); finally, a notch was grinded by a diamond wire in the middle of the half cylinder. The width of the notch was around 70 µm while the depth was 250~300 µm (Fig. 3.5 d). Fig. 3.5 e is the front view optical micrograph of a specimen with the notch. It can be seen that the remaining fiber width is 150 µm and the depth of the notch is 280 µm.

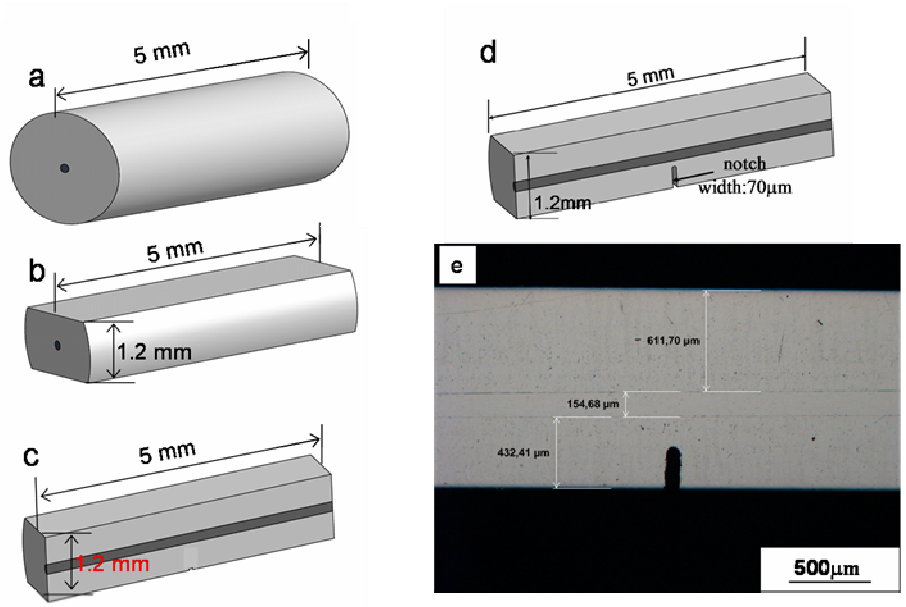

Figure 3.5. Preparation processes of the 3PB testing specimen

As the notch cut by the diamond grinding would not be sharp enough to create a well-defined initial crack location, a pre-crack was formed by a focused ion beam (FIB) on the bottom of the wire grinded notch. Figs. 3.6 a and b show the images of a notch with and without a pre-crack on the bottom, respectively.

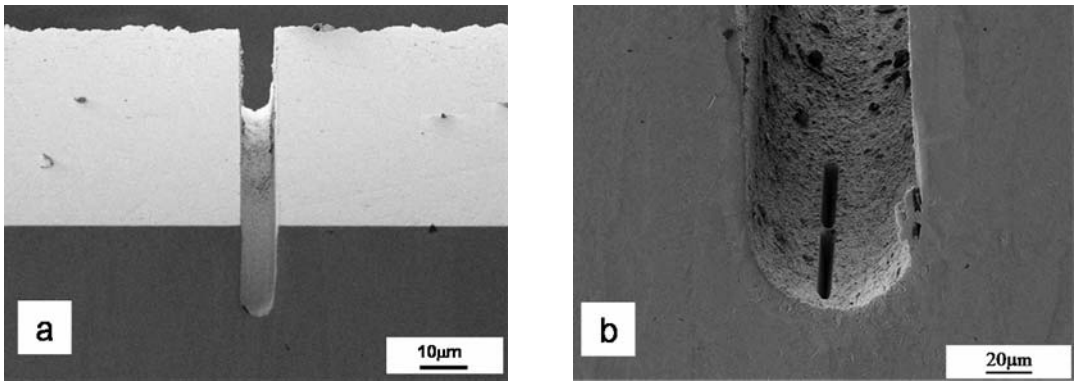

Figure 3.6. Notch bottom views of the specimens for 3PB test: a) a notch without pre-cracking; b) a notch with pre-cracking

3.3 Mechanical property investigation

3.3.1 Push-out test

Figure 3.7 is the image of the push-out device. The push-out testing system is installed on an instrumented macro-indentation device (< 2 kN). The device was equipped with an optical microscope (Fig. 3.7 a), positioning system (X-Y-table) (Figs. 3.7 b and c) and a load sensing unit (a standard load cell capable of a maximum load of 200 N) (Fig. 3.7 a).

The specimen was fixed on a specially designed holder under the assistance of the optical microscope concentrically over a 400 µm hole by a metallic spring. The holder with the fixed specimen was then put on an X-Y-table below the indenter. With the positioning system it was ensured that the indenter would be placed concentrically over the fiber (Fig. 3.8 a). Starting the automated measurement the indenter moved gradually down against the fiber with a speed of 1 µm/s (Figs. 3.8 b and c). Load, time and machine displacement were recorded by a computer program. The time interval between the two sampling points was 0.02 seconds. The fiber displacement (indenter-head displacement) was calculated by eliminating the contribution of the machine compliance. The machine compliance was measured by pressing the indenter on a stiff tungsten carbide plate using the same indentation system. The estimated device compliance was

1 μm/N. The push-out test was manually terminated when the fiber was pushed out 40%~60% of the specimens' thickness.

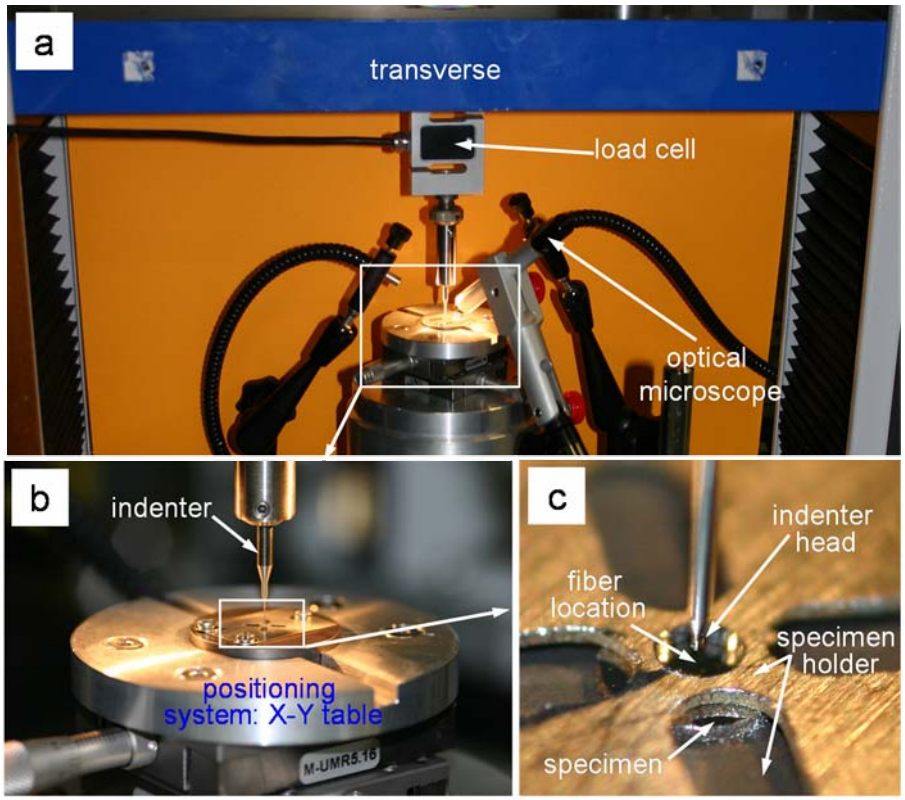

Figure 3.7. Images of push-out device

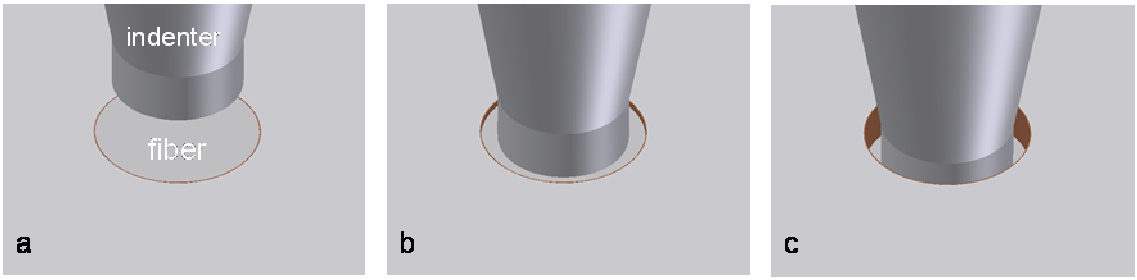

Figure 3.8. The processes of the push-out test

Figure 3.9 shows the detailed structure of the push-out setup. The indenter diameter d_i was 120 μm (subjected to the W fiber diameter of 150 μm) ensuring that the indenter head would not touch the interface region when it was pushing the fiber. D_f, the diameter of the hole where the pushed out fiber went through, was designed as 400 μm to avoid any bending effects during the push-out process (details refer to Hutchinson [80]).

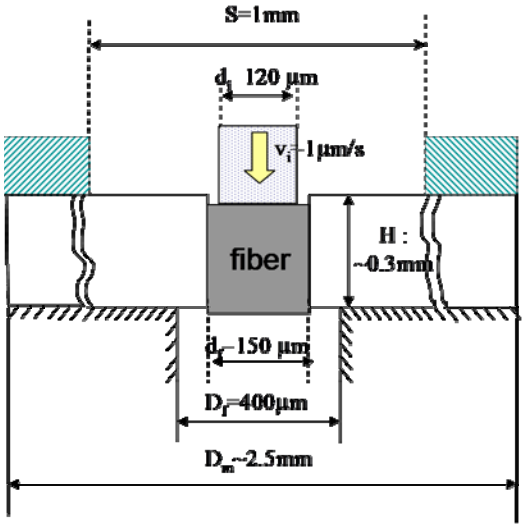

Figure 3.9. Dimensions of the push-out set

3.3.2 Push-back test

The pushed out specimen was taken out of the specimen holder of the push-out test (Fig. 3.10 a.) and turned over leaving the pushed out fiber on the top side (Fig. 3.10 b), then followed the same steps as for the push-out test (Fig. 3.10 c).

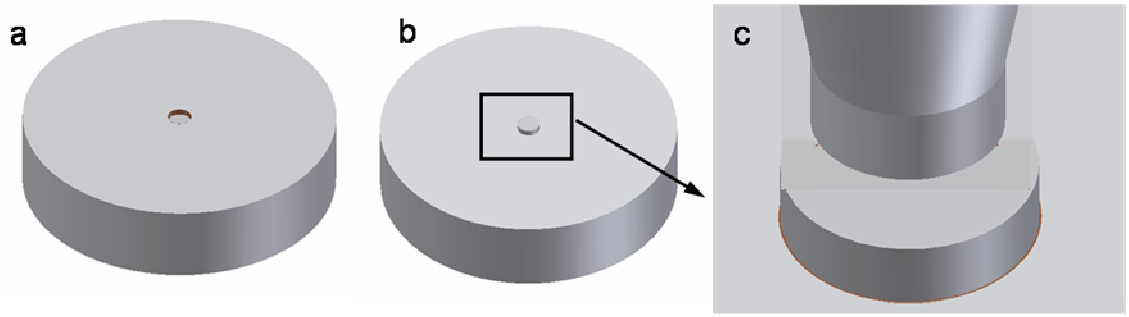

Figure 3.10. The processes of the push-out test

3.3.3 Three point bending test

The three point bending (3PB) tests were carried out in a miniaturized testing setup inside a scanning electron microscope (SEM). The specimen was fixed in the specimen holder and then introduced to the vacuum chamber of the SEM. Fig. 3.11 shows the image of a specimen being held by 3 supporting points of the holder. P_3 was motionless while P_1 and P_2 were movable. The loading system moved up the P_1 & P_2 platform gradually applying a load to the sample. The applied load and the corresponding displacement of the platform were recorded by a computer program. During the testing SEM-pictures were taken.

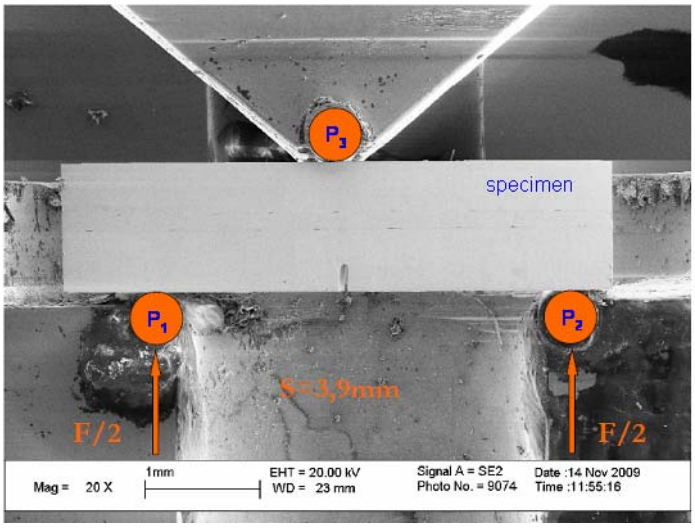

Figure 3.11. One specimen was held by supporting points of the holder in 3PB test

3.4 Thermal stability investigation

The specimens were put into a vacuum furnace for heat treatment. The chamber pressure was below 1×10^{-6} Pa. A temperature of 800 ºC was reached with a heating rate of 60 K/min and was held for 10 hours. The specimens cooled down by furnace cooling at room temperature. The schematic image of the temperature curve is shown in Fig. 3.12.

The heat treated specimens were also push-out tested as previously described.

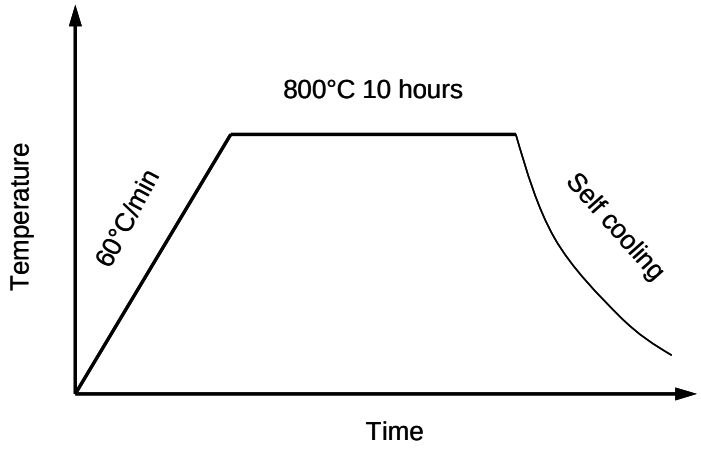

Figure 3.12. Schematic figure indicating the temperature arrangement in heat treatment process

3.5 Material microstructure and component investigation

Two scanning electron microscopes (XL 30 ESEM from FEI operated at 20 kV and Helios Nanolab 600 from FEI operated at 10 kV, both equipped with EDXS) were used to analyze the interface morphology and chemical composition. The Helios device additionally offers a focused ion beam (FIB) equipment.

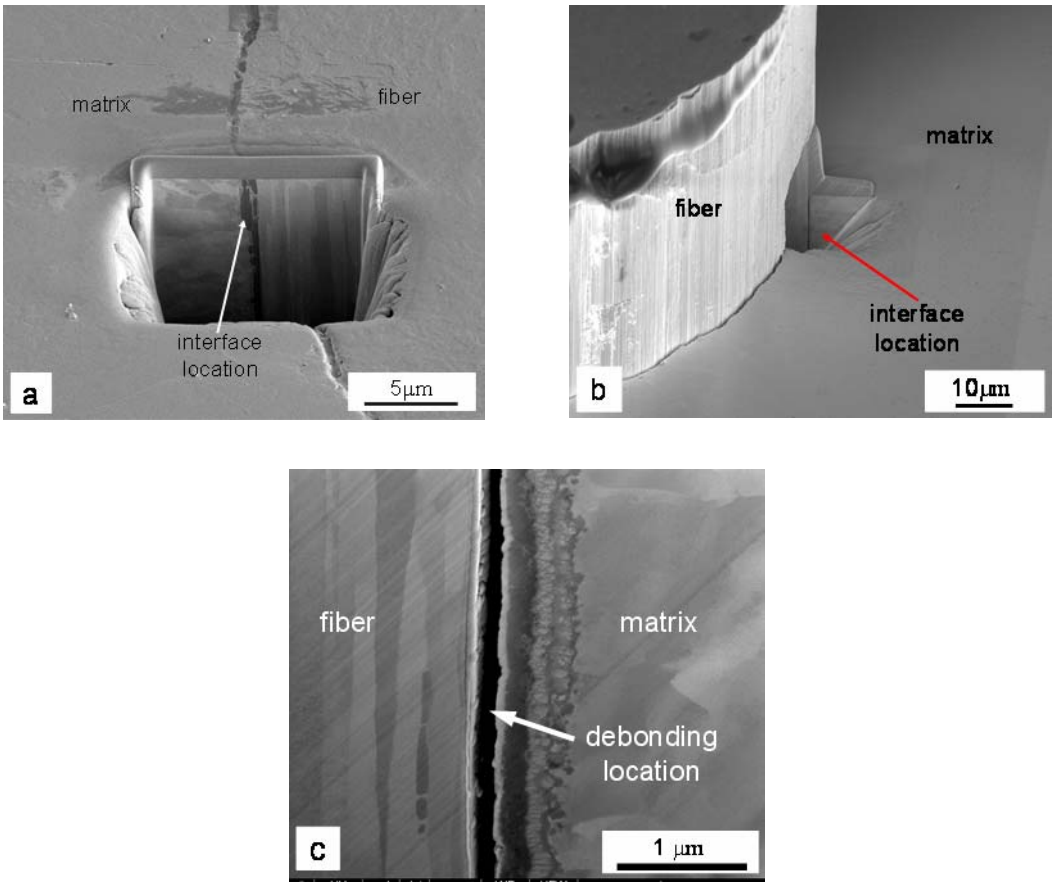

Figure 3.13. FIB cutting locations. a) cutting location before push-out; b) cutting location after push-out; c) magnified image of the cross-section in Fig. 3.13 b

Preparations of cross-sections of the interface were performed using FIB. Fig. 3.13 a shows the FIB cutting location of the interface between fiber and matrix before the push-out test while Fig. 3.13 b shows that after the push-out test. Fig. 3.13 c is the magnified image of the interface marked in Fig. 3.13 b. Subsequently, these cross-sections were analyzed by EDXS (including line scan, point scan, and area scan (mapping)). These images will be discussed extensively in chapter 4. The elemental compositions in some of the interfaces were cleared by SIMS (Atomika SIMS 4000). The results will also be illustrated in chapter 4.

Chapter 4

Results

4.1 Microstructure and chemical composition of the interface

The interface can be sorted into four groups due to their structure type: oxide interface, multilayer interface, Cu interface, and carbon (C) interface. The results of microstructure and chemical composition of them are discussed separately in the following.

4.1.1 Oxide interface

Figure 4.1 shows cross-section images of the ZrO_x interfaces with different thicknesses.

Figure 4.1 a shows that the ZrO_x 150 was deposited with desired thickness and density. Some knobs were present on the outer side (facing to the CVD W) leading to the mechanical bonding between the ZrO_x 150 coating and the W matrix. Figs. 4.1 b and c are SEM images of the ZrO_x interface with thickness of 450 nm and 950 nm, respectively. Both of these layers were deposited with the expected thickness and density. A few pores are found in the coatings together with small amounts of W (white particles). Another ZrO_x-based interface consists of one 125 nm ZrO_x layer and one 135 nm W layer, denoted as ZrO_x&W 260. A SEM image of this specimen is shown in Fig. 4.1 d. It can be seen that the interface has two layers, the brighter and the darker; both of these layers are dense and well-arranged. The EDXS point scan results indicate that the brighter layer consists of W (see Fig. 4.1 e) and the darker layer consists of ZrO_x (Fig. 4.1 f).

Figures 4.2 a and c show SEM images of the ErO_x interfaces with a thickness of 600 nm and 1000 nm, respectively: the interfaces are homogenous and dense; no porosity is found in the coatings. There are some bright phases regularly arranged in the ErO_x layers. The SIMS results (Figs. 4.2 b and d) (the SIMS analysis were done with the reference coatings deposited on the silicon substrates) indicate that there is W present in the ErO_x layers.

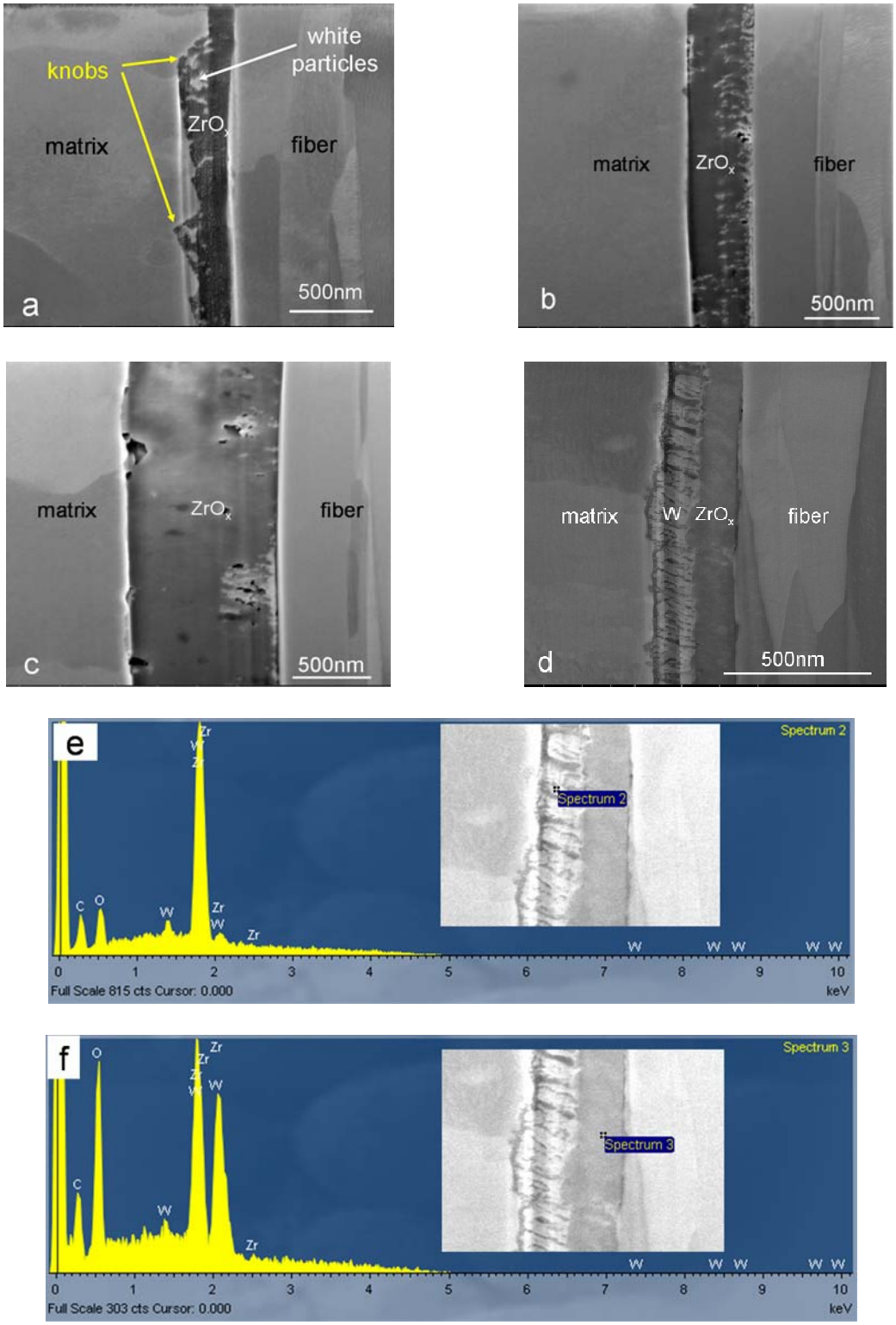

Figure 4.1. Microstructure and EDXS results for the ZrO_x interfaces: a) SEM image of the ZrO_x 150 interface; b) SEM image of the ZrO_x 450 interface; c) SEM image of the ZrO_x 950 interface; d) SEM image of the ZrO_x&W 260 interface; e) EDXS spectrum of ZrO_x in Fig. 4.1 d; f) EDXS spectrum of W in Fig. 4.1 d

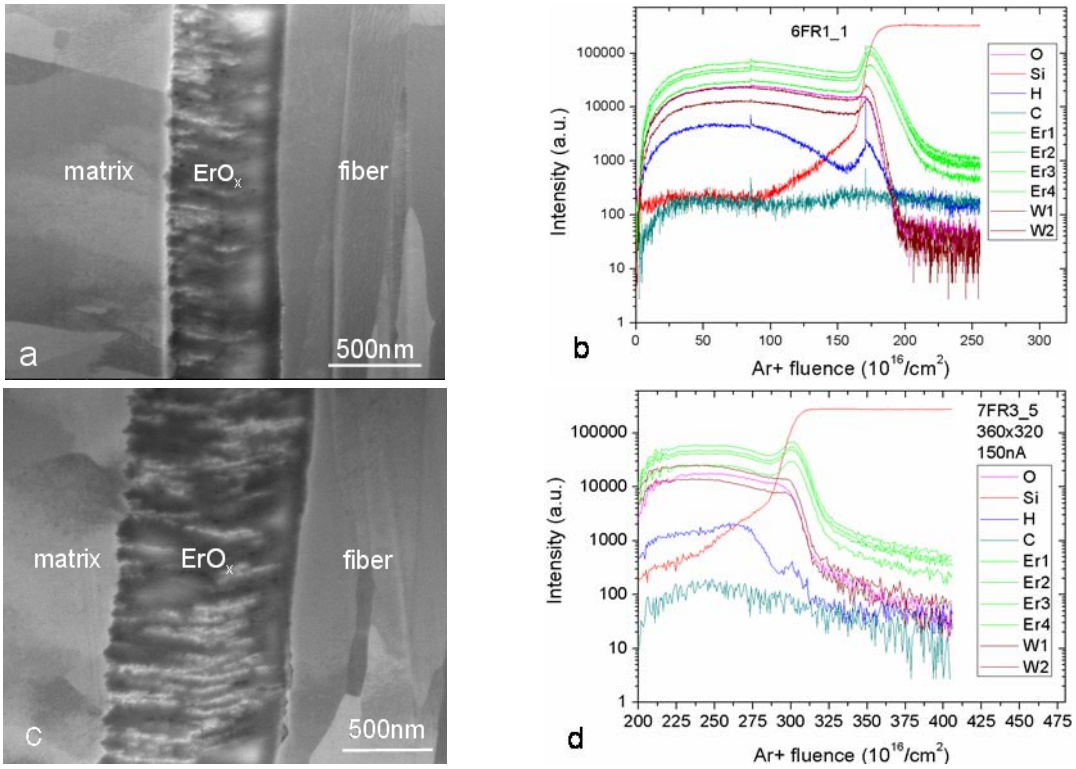

Figure 4.2. Microstructure and SIMS results of the ErO_x interfaces: a) cross-section image of the ErO_x 600; b) SIMS spectra of ErO_x 600 with deposition of the 1st 16 min; c) cross-section image of the ErO_x 1000; d) SIMS spectra of the ErO_x 1000

4.1.2 Multilayer interface

A SEM image of the ZrO_x/Zr multilayer interface is shown in Fig. 4.3 a. The multilayer consists of five ZrO_x films (each 55 nm) and five Zr films (each 35 nm) in alternating way; the brighter layers are ZrO_x while the darker ones are Zr. The layer arrangement is in line with the design (see Fig. 3.2). The EDXS results also confirm the multilayer arrangement. In the Fig. 4.3 b, the yellow line indicates the EDXS scan location; the zirconium (blue) and the oxygen (red) spectra show alternative changes in the peak locations indicating the alternating distribution of ZrO_x and Zr.

Similar layer arrangements are found in the ZrO_x/W multilayer (Fig. 4.3 c, darker layers are ZrO_x , brighter layers are W), ErO_x/W multilayer (Fig. 4.3 d, darker layers are ErO_x, brighter layers are W), Er/W multilayer (Fig. 4.3 e) and Cu/W multilayer (Fig. 4.3 f).

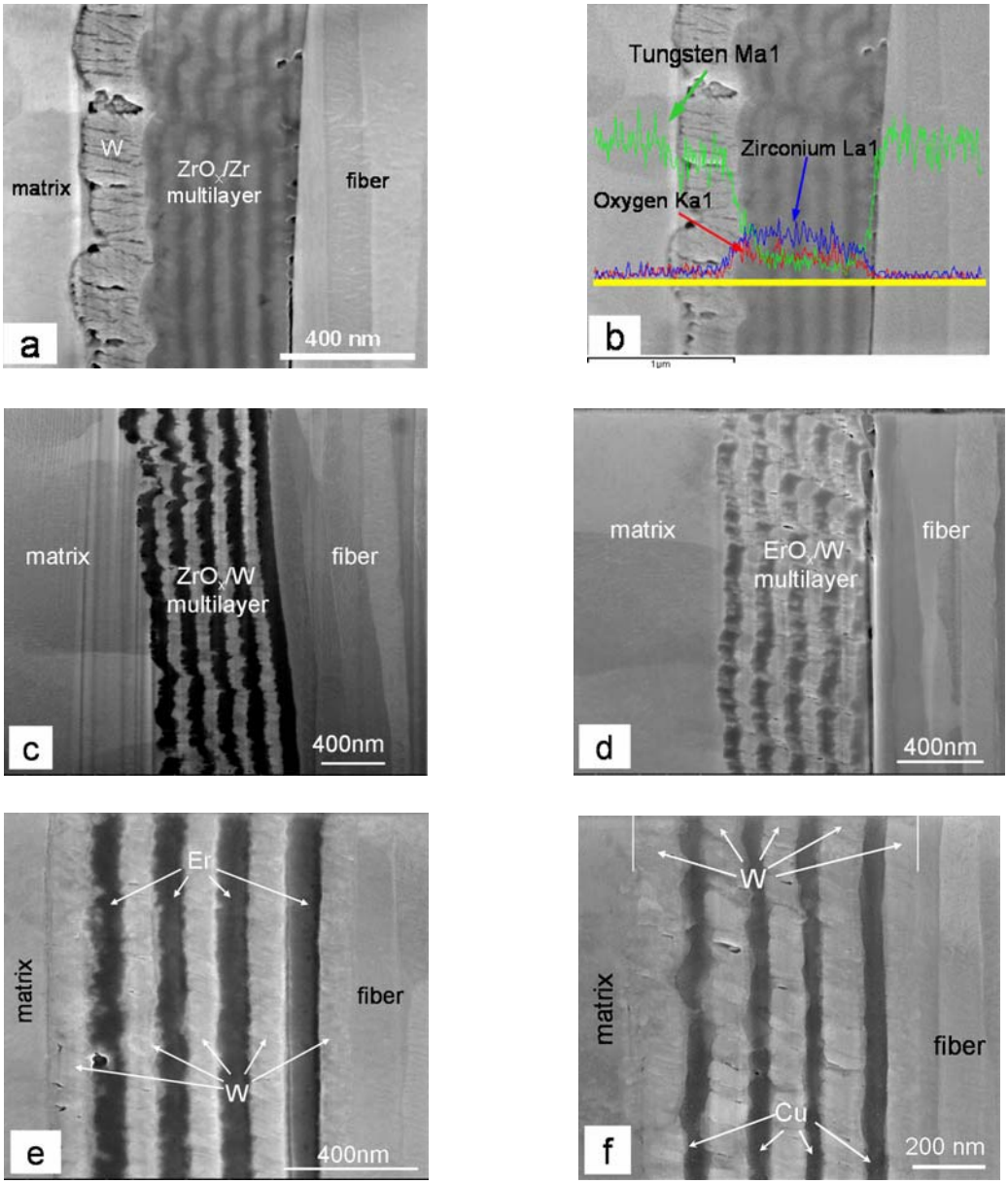

Figure 4.3. SEM images of multilayer interfaces: a) ZrO_x/Zr m; b) EDXS results of the ZrO_x/Zr m; c) ZrO_x/W m; d) ErO_x/W m; e) Er/W m; f) Cu/W m

4.1.3 Cu interface

Figures 4.4 a and b show SEM images of the Cu interface with thickness of 170 nm and 480 nm, respectively. On both sides of the Cu coating, a W layer was deposited (100 nm). There is no obvious porosity found in either the Cu layers or the W layers.

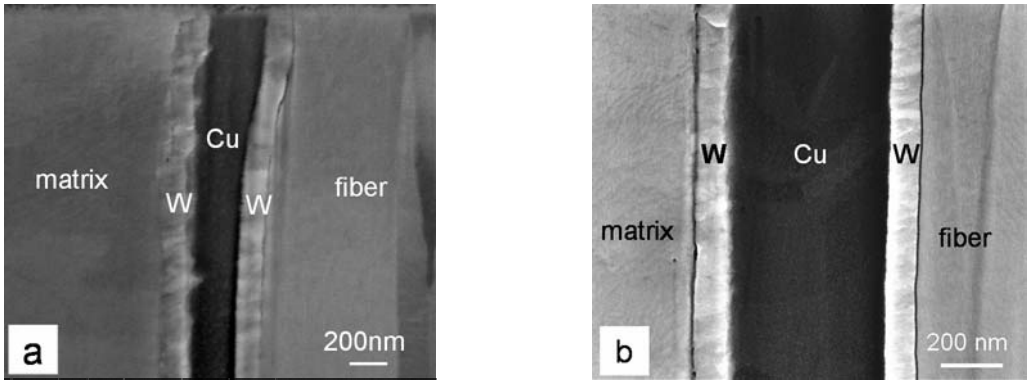

Figure 4.4. SEM images of Cu interfaces: a) Cu 170; b) Cu 480

4.1.4 Carbon interface

Figure 4.5 a shows a SEM image of the carbon (C) interface. The C interface contains four layers: pre-sputtered C (80 nm); pre-sputtered W (100 nm); main C (480 nm); and protection W (100 nm). The EDXS results (Figs. 4.5 b and c) also indicate chemical changes in the different layers.

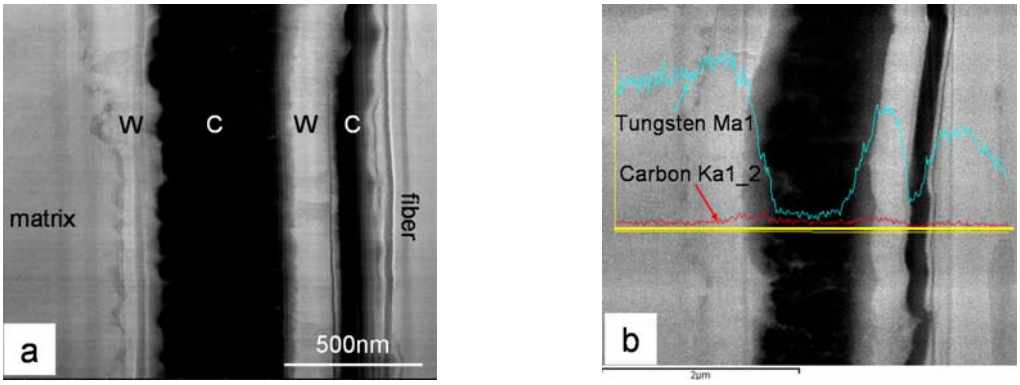

Figure 4.5. SEM images of carbon interface: a) cross-section image of carbon interface coatings; b) EDXS spectra of the carbon interface

4.2 Push-out test

4.2.1 General description of the push-out curve of W_f/W_m composite

The push-out test produced typical data was recorded and is plotted in Fig. 4.6 (curve 1). The corrected curve (see Fig. 4.6, curve 2) is produced by subtracting the equipment compliance (1 μm/N) from the original curve. A typical view of the pushed-out fiber after the push-out test is also included in Fig. 4.6. The dashed lines indicate that no data was detected by the computer recording program at those moments. This lack of data sampling was attributed to the time lag in the load control unit working in a

displacement-controlled mode being unable to catch up with the fast speed of the indenter movement.

The push-out process can be divided into four phases (stages).

In the initial loading phase, the response is nearly linear elastic until the load reaches the maximum P_{max} at point B (phase 1). There is no noticeable change in slope prior to point B. This indicates that interfacial cracks were initiated upon reaching P_{max}, and rapid brittle rupture was triggered immediately. The 'partial debonding' stage (stage 2, as discussed in chapter 2.3.1) is not identifiable on this curve. From A to B, energy was stored due to the elastic deformation of the indenter and the interface. Subsequently, the stored strain energy was released in sudden bursts, causing the dynamic push-out movement from B to C until the fiber was fully decelerated by the frictional resistance (phase 2). The characteristic of this phase is similar to that of the 'complete debonding' stage (stage 3, as discussed in chapter 2.3.1), except a distinct displacement is present. The displacement d_0 produced by the dynamic event is 32 μm (duration is 0.04 seconds). A slight load raise is observed from C to D (phase 3) prior to the quasi-static progressive sliding stage. Beyond point D progressive frictional sliding of the filament continued (phase 4) – P_{fr} denotes the peak friction load (frictional sliding load). The load decreases gradually with the remaining contact area. This phase is the same as the 'pushed-out' stage (stage 4) as discussed in chapter 2.3.1.

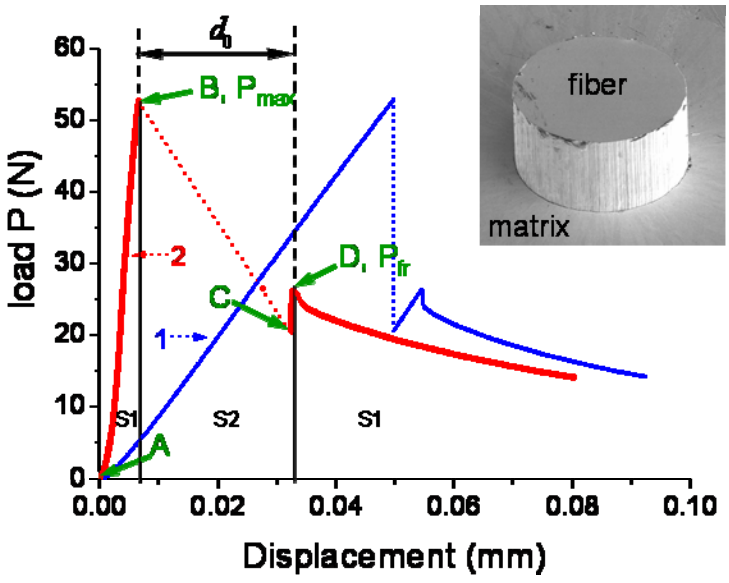

Figure 4.6. Push-out curves, original and corrected

During the push-out process, apart from the equipment compliance, the specimen bending effect can be significant [80, 120]. Fig. 4.7 shows the schematic view of a

specimen loaded by the indenter. The bending effect is strong when the specimen is thin. Very thin specimens can even cause the specimen to be crushed during the push-out test. Fig. 4.8 a shows a crushed Cu 480 specimen with thickness 0.11 mm: cracks appeared on the back side of the specimen. On the other hand, a very thick specimen can also cause problems. Fig. 4.8 b is the fiber surface image of a thick specimen after the push-out test: an indentation is clearly visible. This indentation was formed during the push-out test process since the indenter-head made a dent on the contacting area of the fiber when it was transforming the load to the fiber; the dent is larger when the load is bigger (thicker specimen). Therefore, specimens with moderate thickness can represent the true behavior of the interface during the push-out test. However, specimens of the same thickness also have several percent differences in the characteristic values (such as the maximum debonding load $P_{\max}$, frictional sliding load P_{fr}).

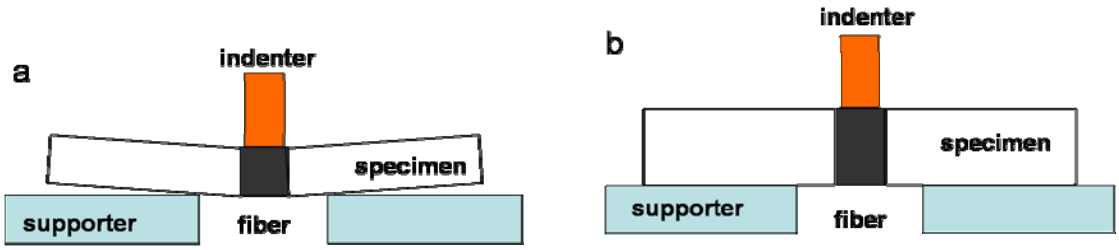

Figure 4.7. Bending effect during the push-out test: a) a thin specimen; b) a thick specimen

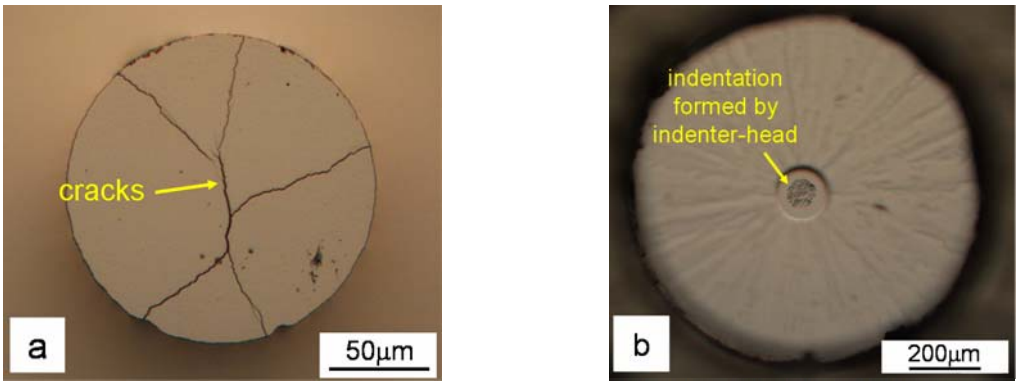

Figure 4.8. Top view images of specimens after the push-out test: a) thin specimen smashed during test; b) indentation on the fiber of the thick specimen

The area below the curves corresponds to the total amount of work done by the applied load, which is the total amount of energy consumed in the push-out process. The average energy absorption Δ can be roughly estimated by dividing the consumed energy by the respective contacting area. The push-out curve can be divided into three parts, S1, S2, and S3 (see Fig. 4.6). The area of S1 can be estimated by approximating it

to a triangle. In the similar way, the area of S2 can be estimated by attributing it to a trapezoid. For S3, a cubic polynomial function can be used for fitting and integrating to estimate the area of S3. The total consumed energy S=S1+S2+S3. The contacting area can be generate by $2\pi r_f H$, where r_f is the fiber radius, and H is the specimen thickness. Then, the average energy absorption $\Delta = S / 2\pi r_f H$.

Apart from the average energy absorption estimation, the interface parameters—interfacial shear strength τ_d, interface radial stress σ_R, friction coefficient μ, asperity cause shear stress τ_R, and interfacial fracture energy Γ_i— can be calibrated using a curve fitting method introduced in chapter 2.3.1.

In the following, the push-out test results comprising of the push-out curve and the average energy absorption, the interfacial parameter calibration, and the microstructure analysis of the interface after push-out test, are sorted into four groups—oxide interface, multilayer interface, Cu interface, and carbon interface— and discussed one by one.

4.2.2 Oxide interface

4.2.2.1 Push-out curve

Figure 4.9 shows the load-displacement curves of the oxide interfaces.

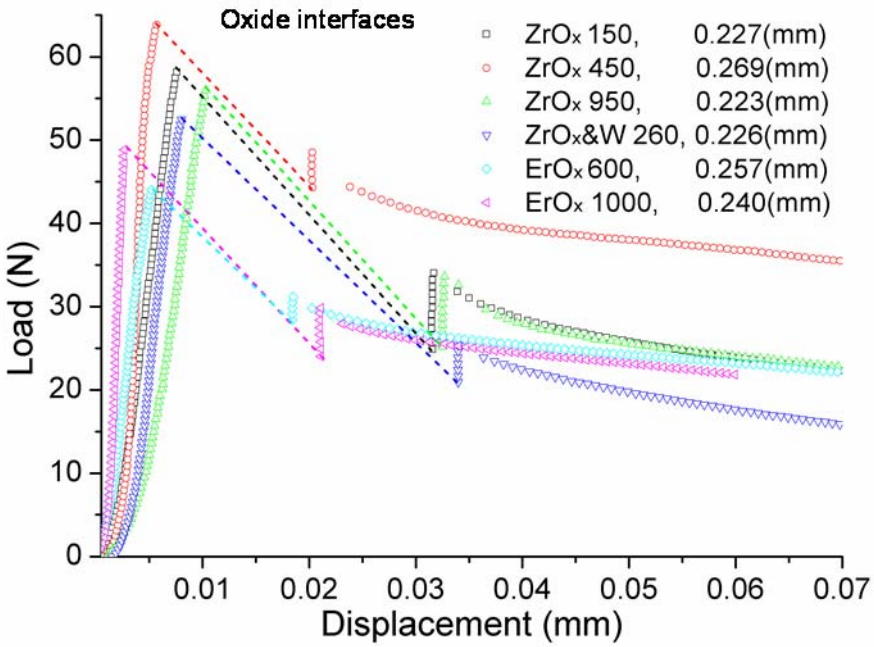

Figure 4.9. Push-out curves for the oxide interfaces

In order to distinguish the curves from one to another, curves of the ZrO_x 450, ZrO_x 950 and ZrO_x&W 260 interfaces were shifted 0.0005 mm, 0.001 mm, and 0.0015 mm along the displacement axis, respectively. It can be seen that all of the curves are of similar shape and exhibit comparable maximum loads.

Some difference are found in the slopes of the first phase among the curves as well as in the frictional sliding loads P_{fr}. The average energy absorption Δ was estimated according to the corresponding curve for each interface. The results are shown in Table 4.1, together with the specimen thickness H, the maximum debonding load $P_{\max}$, the frictional sliding load P_{fr}, and the dynamic displacement d_0. It can be seen that the ZrO_x interfaces have a higher average energy than the ErO_x interfaces.

Table 4.1. The specimen thickness H, the maximum debonding load $P_{\max}$, the frictional sliding load P_{fr}, the dynamic displacement d_0, and the average energy absorption Δ of oxide interfaces.

Interface	H (mm)	$P_{\max}$ (N)	P_{fr} (N)	d_0 (μm)	Δ (kJ/m^2)
ZrO_x 150	0.227	58.2	34.5	23	20.7
ZrO_x 450	0.269	63.8	48.6	15	23
ZrO_x 950	0.223	56	33.6	23	20.5
ZrO_x&W 260	0.226	52.4	25	25	17.3
ErO_x 600	0.257	44	31.6	13	15.6
ErO_x 1000	0.240	49	29	18	16.7

4.2.2.2 Interfacial parameter calibration

(1) Interfacial shear strength τ_d

The interfacial shear strength τ_d can be calibrated by curve fitting using Eq. (2.8). To describe the fitting procedure, the ZrO_x&W 260 interface case is discussed as an example: more than 20 pairs of $P_{\max}$ - H data were collected and plotted in Fig. 4.10. For each thickness, at least five tests were done. The least-square method was used to obtain the optimum value of τ_d, leading to the best fit line to the experimental data. The deviation σ_i is set according to a cluster distribution (blue scatters). The calibrated τ_d value of the ZrO_x&W 260 interface is 385 MPa. The best fit line is shown in Fig. 4.10 (red line), as well.

4.2.2 Oxide interface

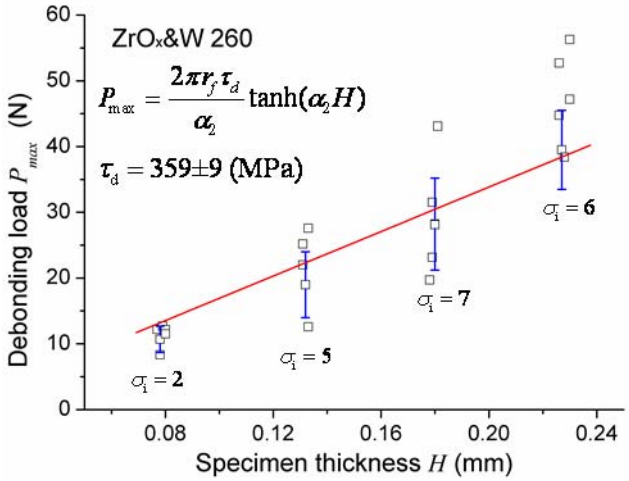

Figure 4.10. The collected complete debonding load P_{max} vs. specimen thickness H, and curve fitting result for the ZrO_x&W 260 interface

Using the same curve fittings procedure, τ_d values were calibrated for all other oxide interfaces. A comparison of the results is shown in Fig. 4.11. The average interfacial shear strength τ_d of oxide interfaces lies around 400 MPa. The highest τ_d is observed from the ZrO_x 450 interface, with a value of 441 MPa, and lowest τ_d is found from ZrO_x&W 260 interface, which is 359 MPa. The fact is that all of the oxide interfaces have the comparable shear strength, indicating the comparable bonding.

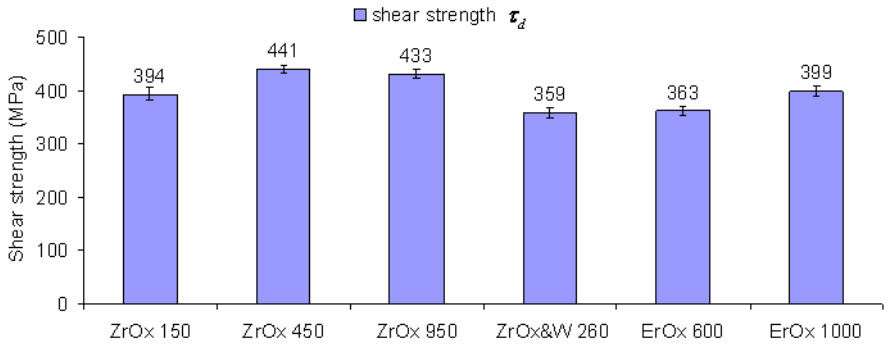

Figure 4.11. Curve fitting results of the interfacial shear strength τ_d for the oxide interfaces

(2) Interface radial stress σ_R, friction coefficient μ, asperity cause shear stress τ_R, and interfacial fracture energy Γ_i

The interfacial parameters σ_R, μ, and Γ_i were obtained simultaneously by curve fitting using Eqs. (2.16) and (2.18) as introduced in chapter 2.3.1.

Below, the results for the ZrO_x&W 260 interface are discussed exemplarily. The P_{fr} - L data are collected and plotted in Fig. 4.12 a; the data of p_d - H are collected and plotted in Fig. 4.12 b. In principle, there is no limitation in the range of each parameter in

the curve fitting process. However, in order to save computation time, the parameters' value ranges were specified assuring a 'good fit' quality. The limit ranges for each parameter were chosen as follows: μ : 0~3; σ_R : 0~500; Γ_i : 0~50.

The optimum values and the best fits (red lines) are shown in the corresponding figures. The results are as follows: the interface radial stress σ_R is 297 MPa; the interfacial friction coefficient μ is 1.29; the asperity caused shear stress τ_R can be calculated as $\tau_R = \sigma_R \times \mu$ =1.29×10^6=136.7 MPa; the fracture energy Γ_i is 2.99±0.4 J/m^2. Following the same procedure, the curve fitting for the interfacial parameters, σ_R, μ, and Γ_i was applied to experimental data of all other oxide interfaces. The results are shown in Fig. 4.13.

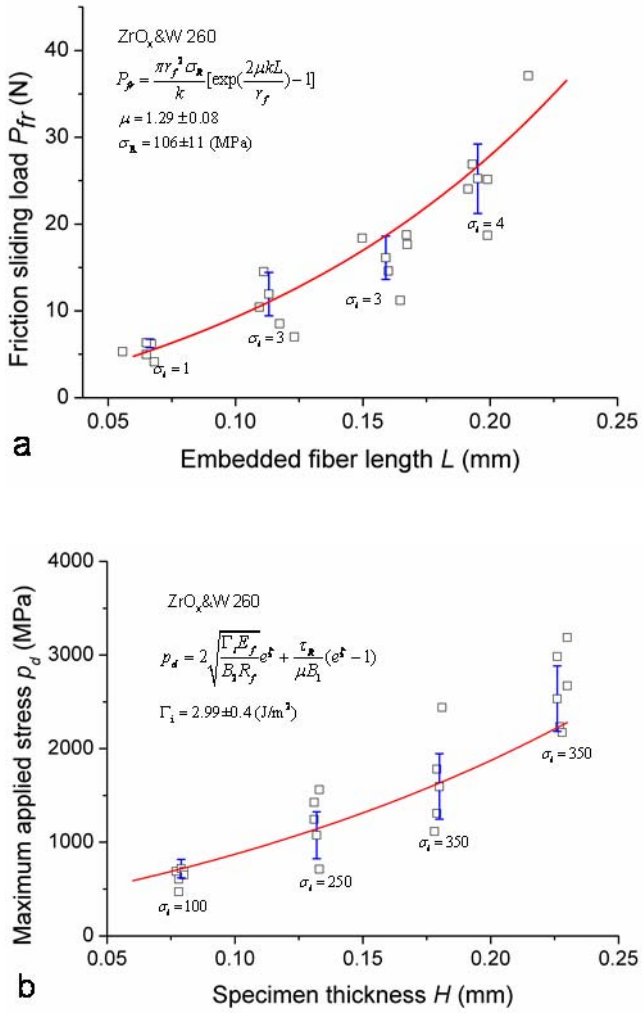

Figure 4.12. Curve fitting results of the interfacial parameters σ_R, μ, and Γ_i based on the push-out data: a) recorded P_{fr} - L data and curve fitting results of μ and σ_R; b) recorded p_d - H data and curve fitting result of Γ_i

4.2.2 Oxide interface

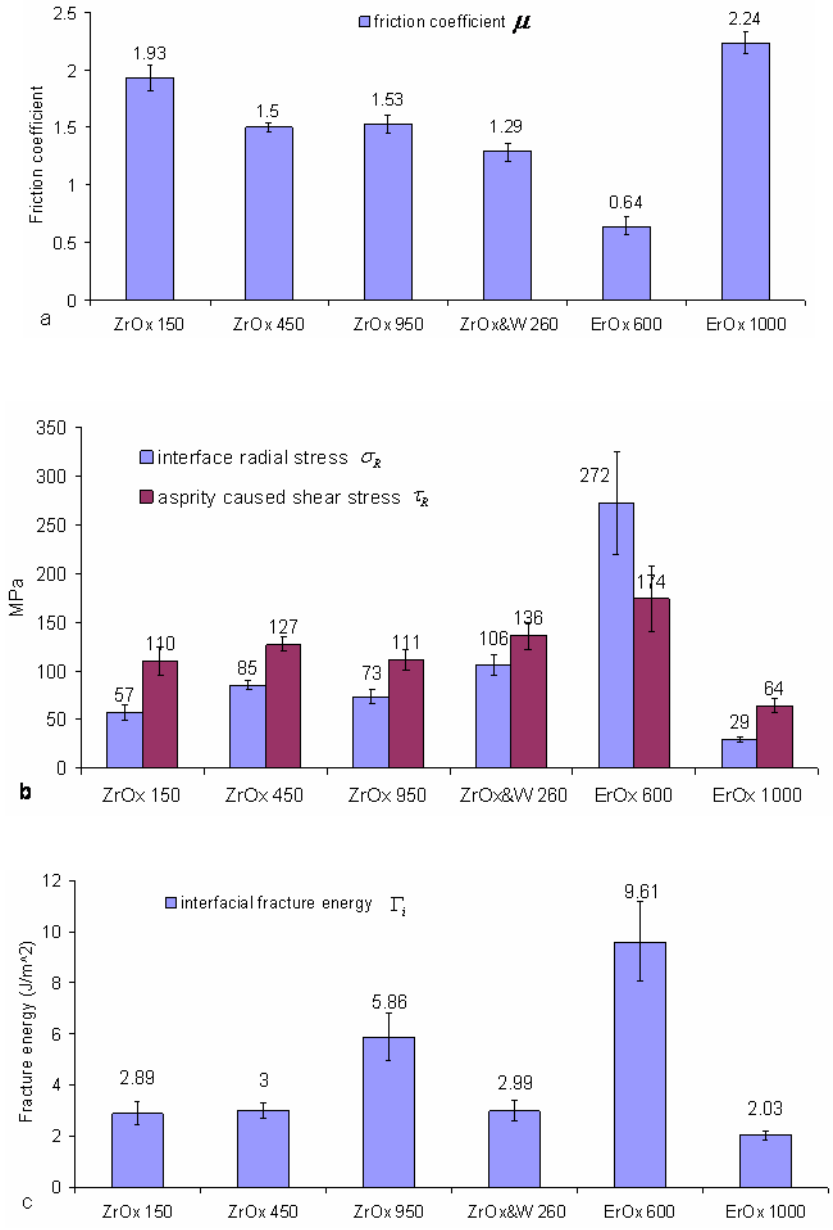

Figure 4.13. Curve fitting results for the oxide interfaces: a) friction coefficient μ; b) interface radial stress σ_R and asperity caused shear stress τ_R; c) interfacial fracture energy Γ_i

In Fig. 4.13 a: lowest friction coefficient μ is found from the ErO_x 600 interface (0.64) while the largest μ is observed from ErO_x 1000 (2.24); ZrO_x interfaces have friction coefficient larger than 1.5. In Fig. 4.13 b: the ErO_x 600 interface has the highest interface radial stress σ_R (272 MPa) and asperity caused shear stress τ_R (174 MPa), while ErO_x 1000 has the lowest σ_R (29 MPa) and τ_R (64 MPa). The σ_R of all the ZrO_x interfaces lie around 70 MPa, while the τ_R of them range from 110 MPa to 127 MPa. In Fig. 4.13 c: the ZrO_x 150, ZrO_x 450, and ZrO_x&W 260 interfaces have very

similar fracture energy Γ_i which is around 3 J/m^2, ZrO_x 950 has a Γ_i of 5.96 J/m^2. The ErO_x 600 interface contains the largest Γ_i (9.61 J/m^2) among all the oxide interfaces, while the ErO_x 1000 interface has the smallest Γ_i (2.03 J/m^2).

4.2.2.3 Microstructure of the interface after the push-out test

Interfacial fracture energy is strongly related to the interfacial debonding behaviors, such as the debonding location, the fracture or deformation of interface coating, or the path of crack propagation. In the following, the microstructure analysis results of the oxide interfaces are shown to describe the debonding behaviors.

(1) ZrO_x interfaces

Figure 4.14 shows SEM images of the ZrO_x 150 interface after the push-out test. Fig. 4.14 a shows that the ZrO_x 150 interface had a typical brittle fracture. The broken coating is partly attached to the fiber and partly to the matrix. The coating on the fiber shows a dusty structure without any plastic deformation. From the cross-section image of the interface (see Fig. 4.14 b), one can see that the debonding location lies in the ZrO_x 150 layer (close to the fiber side); the interface between the ZrO_x coating and the matrix is not smooth; and defects in the coating may be the initial debonding sites for the rupture of ZrO_x 150 coating. These findings indicate that the bonding strength of the W fiber and the ZrO_x coating, the ZrO_x coating and the W matrix, as well as the fracture strength of the ZrO_x coating itself are comparable.

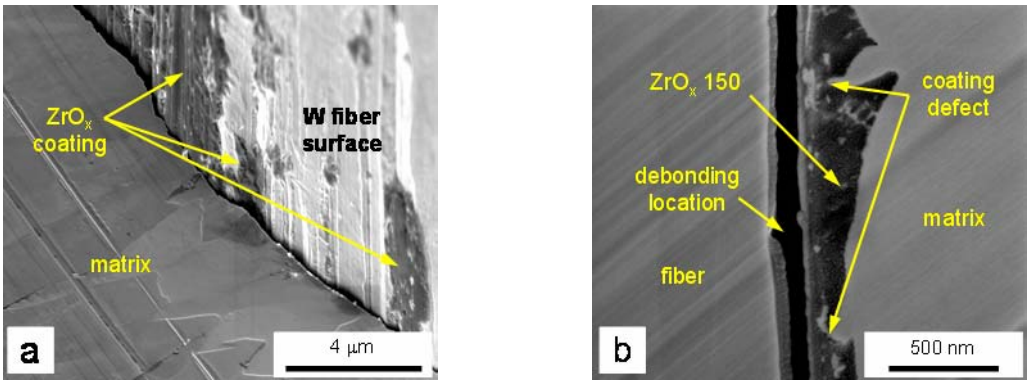

Figure 4.14. SEM images of ZrO_x 150 specimen after the push-out test: a) the ZrO_x coating on the fiber shows a dust structure; b) the debonding location lies in the ZrO_x coating

Figure 4.15 shows microstructure images of the ZrO_x 450 interface after the push-out test. Compared to the ZrO_x 150 interface, the ZrO_x 450 interface definitely shows a clear difference in the debonding location. Fig. 4.15 a indicates that the pushed out fiber has a clean surface, and the surface shows a typical W wire surface structure. There is no ZrO_x

dust attached to the fiber. The main coating remains at the matrix side and exhibits no plastic deformation (see Fig. 4.15 a). From the cross-section images shown in Fig. 4.15 b, it becomes clear that, the debonding location lies between the W fiber surface and the ZrO_x 450 coating; the coating itself was deposited with higher quality compared to the ZrO_x 150 interface case; the coating contains fewer defects, and the side facing to the W matrix is smooth. The ZrO_x layer and the W matrix are well-bonded, although there is some small-scale porosity in this region (see Fig. 4.15 b). These phenomena indicate that an increase of the ZrO_x thickness leads to a stronger ZrO_x coating and better bonding between the ZrO_x coating and the W matrix. The deposition quality of ZrO_x 450 coating is better than that of the ZrO_x 150 coating, which may also lead to the observed strength increase. On the other hand, the debonding location dominates the interface between the W fiber and the ZrO_x coating which implies that the bonding strength of the W fiber and the ZrO_x coating is weaker than that of the ZrO_x coating and the W matrix.

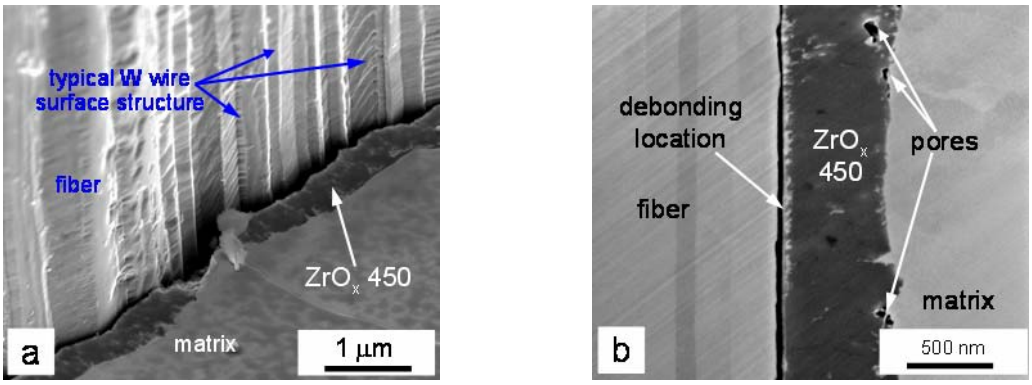

Figure 4.15. SEM images of ZrO_x 450 specimen after the push-out test: a) the ZrO_x coating stays in the W matrix and shows no dust structure; b) the debonding location lies between the W fiber and the ZrO_x coating

However, although the ZrO_x 150 interface and the ZrO_x 450 interface show different debonding locations, the fracture energy of these two are the same according to the curve fitting results (Γ_i =2.89 ± 0.5 J/m^2 for ZrO_x 150 and Γ_i =3 ± 0.3 J/m^2 for ZrO_x 450). This indicates that the fracture energy of the debonding in the ZrO_x 150 coating is comparable to that of the debonding between the W fiber and the ZrO_x 450 coating.

Figure 4.16 shows microstructure images of the ZrO_x 950 interface after the push-out test.

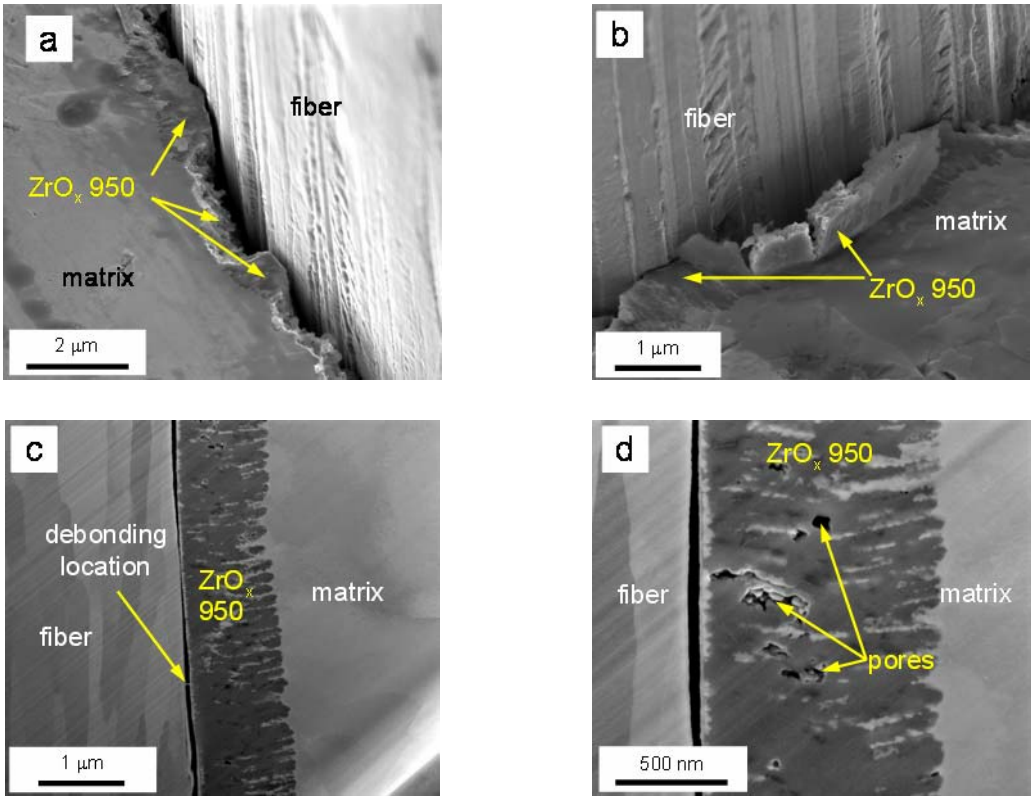

Figure 4.16. SEM images of ZrO_x 950 specimen after the push-out test: a) and b) the ZrO_x 950 coating was damaged during the push-out process; c) the debonding location lies between the W fiber and the ZrO_x coating; d) the porosity in ZrO_x coating

In Fig. 4.16 a and b, it can be observed that the pushed-out fiber has a clean surface, which exhibits the typical W wire surface structure (the same as shown in the ZrO_x 450 case). The cross-section images show that the debonding location lies between the W fiber and the ZrO_x coating (see Fig. 4.16 c). These facts indicate the weakest bonding location in the ZrO_x 950 interface is between the W fiber and the ZrO_x 950 coating (the same as in ZrO_x 450 interface). However, the ZrO_x 950 interface shows significantly more damage in the coating than the ZrO_x 450 interface: on the surface of the matrix, the damage of the ZrO_x 950 coating can be observed (see Figs. 4.16 a and b). This damage is attributed to the porosity in the ZrO_x 950 coating (see Fig. 4.16 d) which have caused many weak locations leading the crack propagation in the ZrO_x 950 coating. Thus, during the push-out process, apart from the debonding of the W fiber and the ZrO_x 950 coating, the cracks and damage were formed inside of the ZrO_x 950 coating, which consumed a great amount of energy. Therefore, the ZrO_x 950 interface has a higher fracture energy than the ZrO_x 450 interface, which is in agreement with the curve fitting results (5.86±0.92 J/m^2 for ZrO_x 950 interface and 3±0.3 J/m^2 for ZrO_x 450 interface).

4.2.2 Oxide interface

Figure 4.17 shows microstructure images of the ZrO_x&W 260 interface after the push-out test. This interface contains one 125 nm layer with ZrO_x and one 135 nm layer with W. The 135 nm W layer was specially designed for the comparison of interfacial properties between the single and double layers structures. In Fig. 4.17 it can be observed that the ZrO_x&W 260 interface shows a similar debonding situation as the ZrO_x 450 interface: the main debonding occurs between the W fiber and the ZrO_x coating (see Fig. 4.17 b); while no obvious plastic deformation of the interface is observed (see Fig. 4.17 a). This is in accordance with the curve fitting result, which shows that these two interfaces have a similar fracture energy (2.99±0.4 J/m^2 for ZrO_x&W 260 interface and 3 ± 0.4 J/m^2 for the ZrO_x 450 interface). Obviously, the adoption of the W layer did not notably affect the debonding behavior.

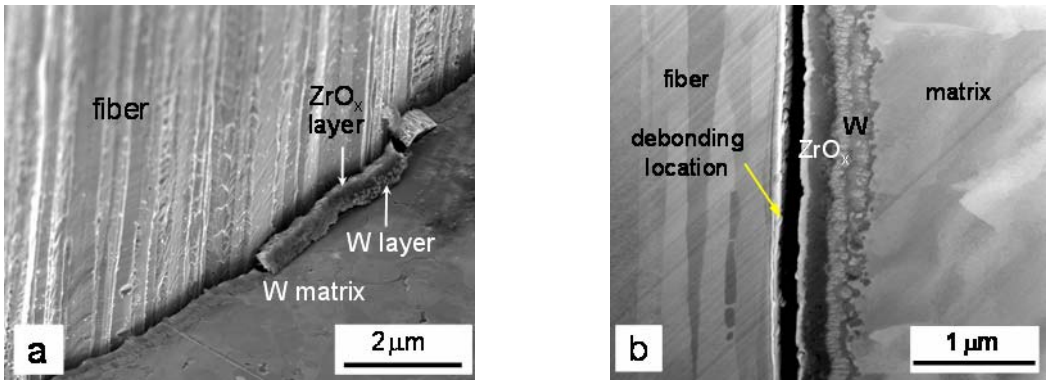

Figure 4.17. SEM images of ZrO_x&W 260 specimen after the push-out test: a) ZrO_x &W 260 coating remained in the W matrix; b) the debonding location lies between the W fiber and the ZrO_x coating

(2) ErO_x interfaces

Figure 4.18 shows microstructure images of the ErO_x 600 interface after the push-out test, and Fig. 4.19 shows those of the ErO_x 1000 interface. The ErO_x 600 and ErO_x 1000 interfaces have similar debonding locations, situated between the W fiber and the ErO_x coating (see Fig. 4.18 b and Fig. 4.19 b). Their debonding behavior is also similar to that of the ZrO_x interfaces. From the cross-section images, it is found that the gap between the fiber and the ErO_x 600 coating (see Fig. 4.18 b) is much smaller than that between the fiber and the ErO_x 1000 coating (see Fig. 4.19 b). This may indicate that, the contact of the debonded interfaces is tighter in the ErO_x 600 interface than in the ErO_x 1000 interface, leading to a larger friction and fracture energy. The results of asperity caused shear stress τ_R and interfacial fracture energy Γ_i which were obtained by curve fitting method indeed indicate that the ErO_x 600 interface had a higher τ_R and Γ_i than the other interfaces (see Fig. 4.13).

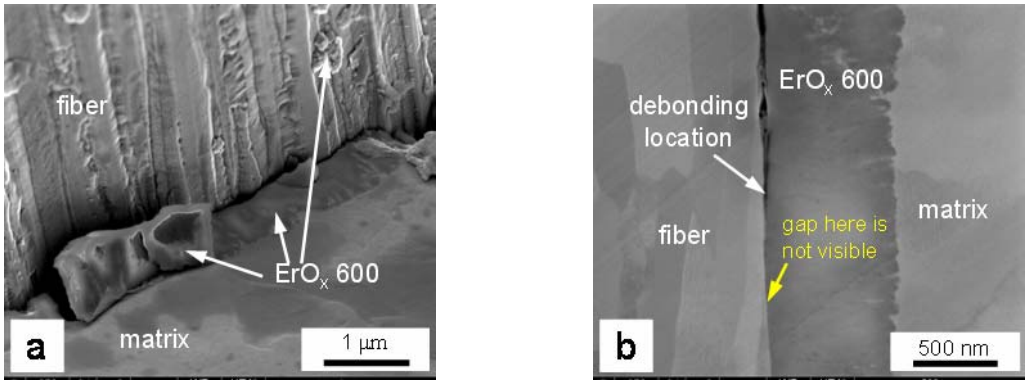

Figure 4.18. SEM images of ErO_x 600 specimen after the push-out test. a) ErO_x 600 coating damage; b) the debonding location lies between the W fiber and the ErO_x coating

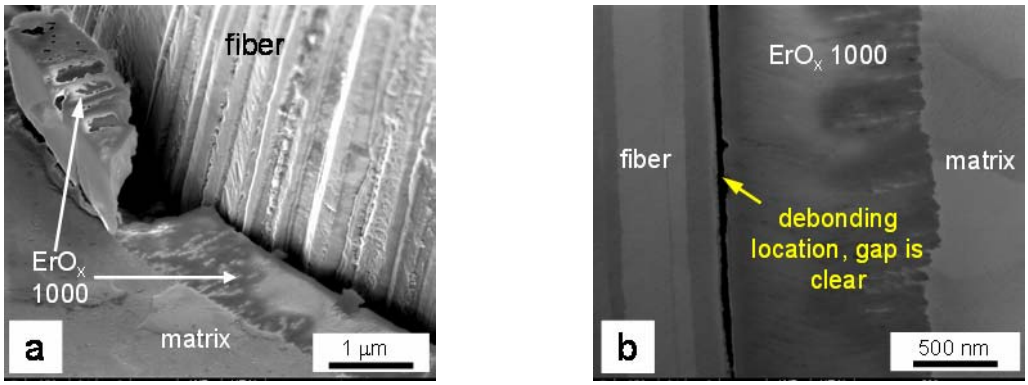

Figure 4.19. SEM images of ErO_x 1000 specimen after the push-out test. a) ErO_x 1000 coating damage; b) the debonding location lies between the W fiber and the ErO_x coating

Thus, it can be concluded as following: during the push-out process, specimens with oxide interfaces show a similar debonding behavior; the debonding locations lie mainly between the W fiber and the oxide coatings; the microcracks were formed in the oxide coatings due to the porosity and particles. The interfacial debonding and microcrack formation caused energy consumption. These results are in accordance with the interface design motivation (fit types b 1), b2), and c)).

4.2.3 Multilayer interface

4.2.3.1 Push-out curve

Similarly to the oxide interfaces, push-out curves for the multilayer interfaces are plotted in Fig. 4.20. The estimated results of the average energy absorption Δ, as well as the specimen thickness H, the maximum debonding load P_{max}, the frictional sliding load P_{fr}, and the dynamic displacement d_0 are shown in Table 4.2.

4.2.3 Multilayer interface

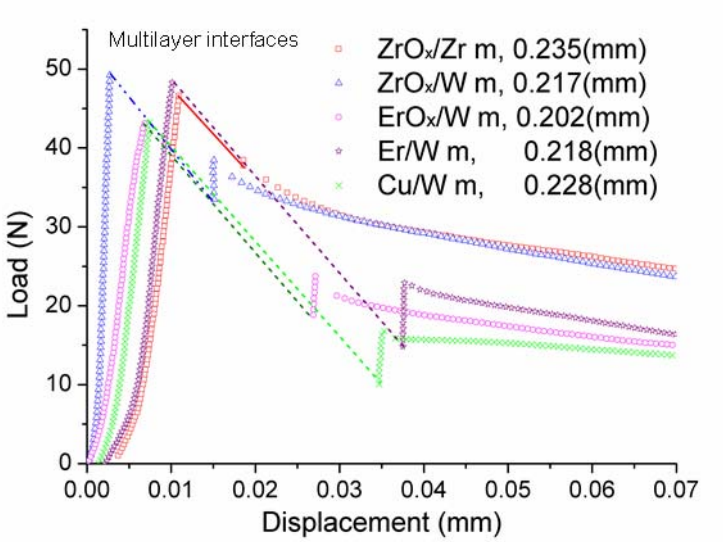

Figure 4.20. Push-out curves for the multilayer interfaces

Table 4.2. The specimen thickness H, the maximum debonding load P_{max}, the frictional sliding load P_{fr}, the dynamic displacement d_0, and the average energy absorption Δ of multilayer interfaces.

Interface	H (mm)	P_{max} (N)	P_{fr} (N)	d_0 (μm)	Δ (kJ/m^2)
ZrO_x/Zr m	0.235	46.3	37.8	7	18.3
ZrO_x/W	0.217	49.2	38.3	12	21.9
ErO_x/W m	0.202	42.8	23.5	21	16
Er/W m	0.218	48.3	22.9	27	16.8
Cu/W m	0.228	43.5	16.8	28	13.1

The multilayer interfaces have a similarity to the push-out curves of the oxide interfaces. The maximum debonding loads of all multilayer interface specimens are comparable, the friction loads P_{fr} are different. The ZrO_x/Zr m and ZrO_x/W m interfaces have much higher friction loads P_{fr} than the other multilayer interfaces. The displacements d_0 produced by the dynamic events of the ZrO_x/Zr m and ZrOx/W m interfaces are much smaller than the others. Further more, the third phase of the push-out process is not visible in the curve of ZrO_x/Zr m interface (red squares). This could be due to the large roughness of the debonded interfaces. The ZrO_x-based multilayer interfaces have larger average energy absorption than the ErO_x ones. Cu/W multilayer has the lowest average energy absorption among the multilayer interfaces.

4.2.3.2 Interfacial parameter calibration

The interfacial parameters of multilayer interfaces were calibrated using the same procedure as discussed in chapter 4.2.2.2.

(1) Interfacial shear strength τ_d

The results of interfacial shear strength of multilayer interfaces are shown in Fig. 4.21. The average shear strength τ_d of the multilayer interfaces is 350 MPa. Cu/W multilayer interface and the ZrO_x/W multilayer interfaces have the highest two τ_d, 429 MPa and 413 MPa, respectively. The other multilayer interfaces have τ_d of around 330 MPa. The τ_d of the multilayer interfaces are comparable to that of the oxide interfaces.

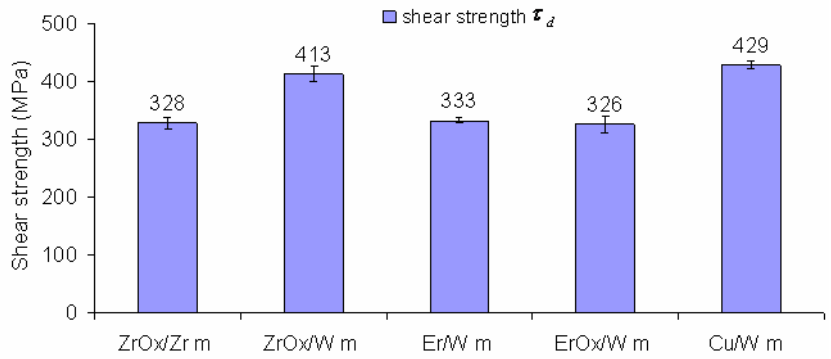

Figure 4.21. Curve fitting results of the interfacial shear strength τ_d for the multilayer interfaces

(2) Interface radial stress σ_R, friction coefficient μ, asperity caused shear stress τ_R, and interfacial fracture energy Γ_i

The calibrated results of the interface radial stress σ_R, the friction coefficient μ, the asperity caused shear stress τ_R, and the interfacial fracture energy Γ_i for the multilayer interfaces are shown in Fig. 4.22.

All of the multilayer interfaces have μ larger than 1 (see Fig. 4.22 a). The ErO_x/W m interface have a μ larger than 2. ZrO_x/W 260 interface had the lowest μ among the multilayer interfaces, which is 1.2. The μ of the multilayer interfaces are relatively larger than those of the oxide interfaces.

The highest σ_R and τ_R are found in the ZrO_x/W m interface, while other multilayer interfaces have comparable σ_R (around 60 MPa) and τ_R (around 100 MP) (see Fig. 4.22 b)

The Cu/W m interface has the highest fracture energy among the multilayer interfaces, which is 7.66 J/m^2, comparable to the ErO_x 600 interface. The other multilayer interfaces

have fracture energy lying around 3 J/m^2, which is similar to that of the ZrO_x interfaces (see Fig. 4.22 c).

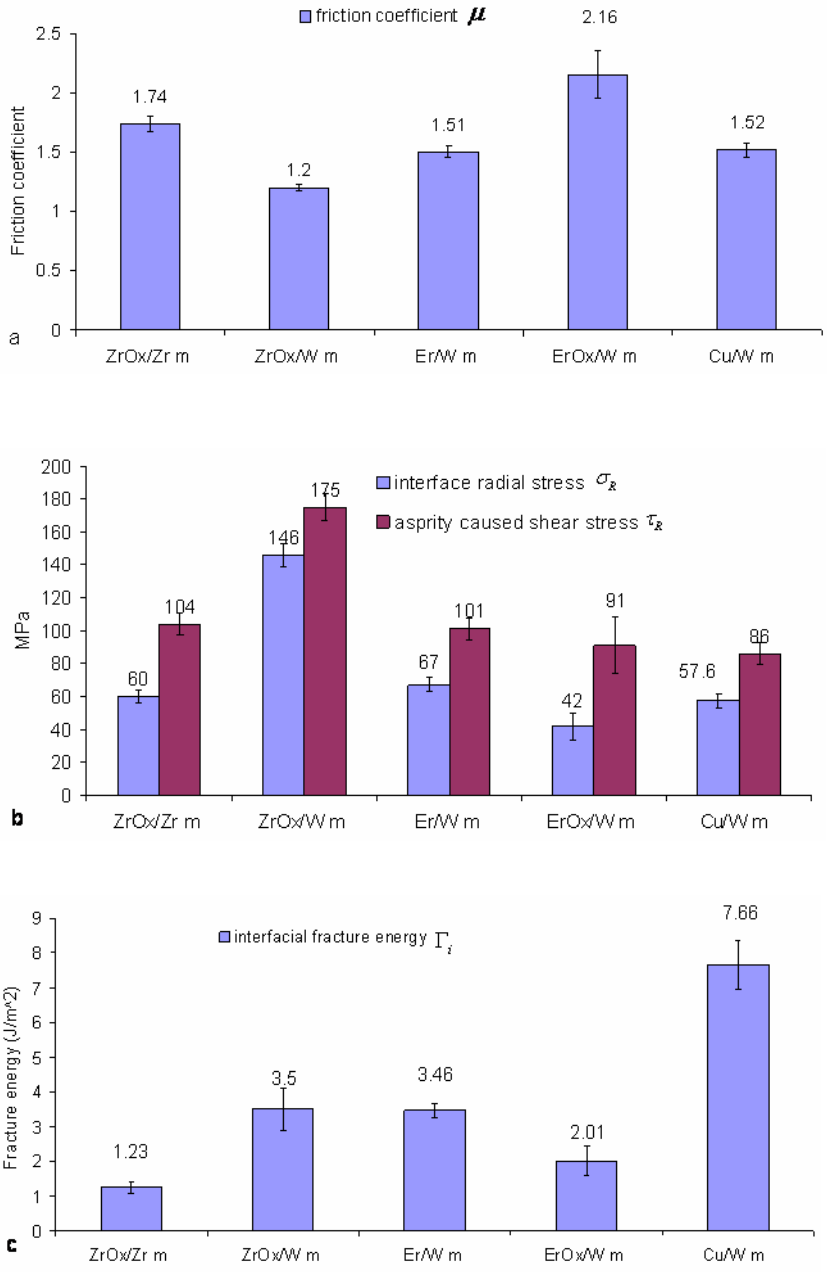

Figure 4.22. Curve fitting results for the multilayer interfaces: a) the friction coefficient μ; b) the interface radial stress σ_R and the asperity caused shear stress τ_R; c) the interfacial fracture energy Γ_i

4.2.3.3 Microstructure of the interface after the push-out test

Figure 4.23 shows microstructure images of the ZrO_x/Zr multilayer interface after the push-out test. Figs. 4.23 a and b are the cross-section images at different cutting locations,

showing different debonding locations. One debonding location lies between the W fiber and the interface coating (see Fig. 4.23 a) while another location lies between the interface coating and the W matrix (see Fig. 4.23 b). This finding is confirmed by the overview image of the ZrO_x/Zr multilayer interface after the push-out test (see Fig. 4.23 c). Fig. 4.23 c shows that debonding happened on both sides of the ZrO_x/Zr multilayer coating and that the interface coating underwent a brittle fracture during the push-out process.

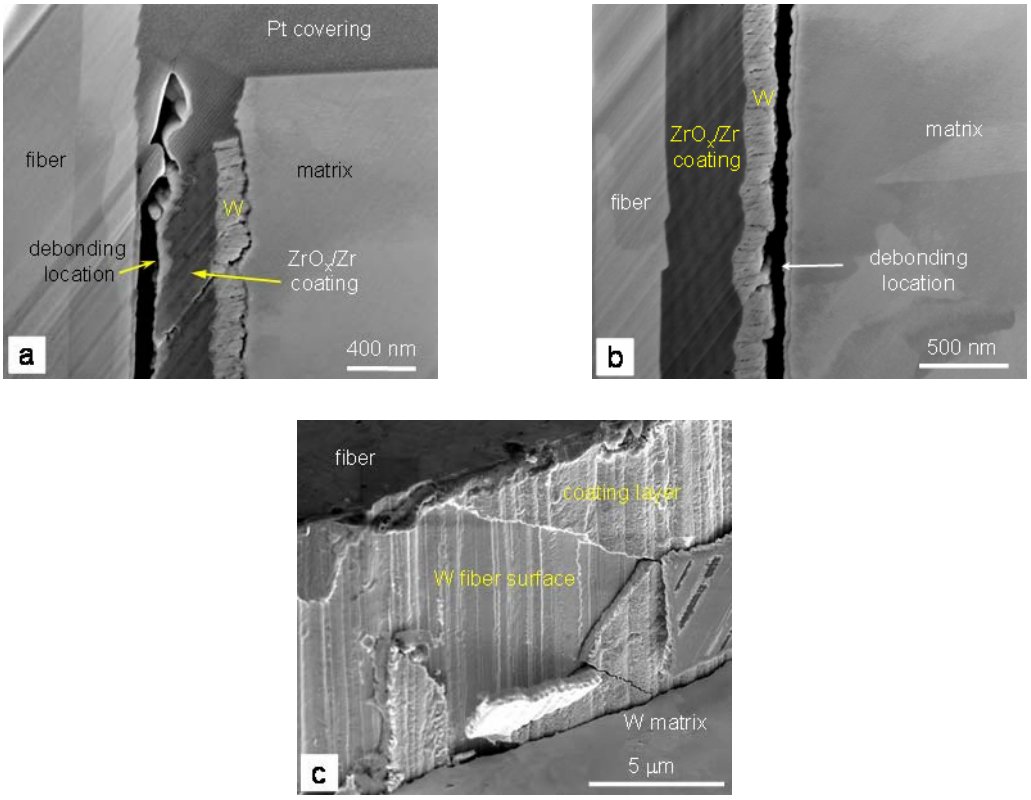

Figure 4.23. SEM images of ZrO_x/Zr m specimen after the push-out test: a) the debonding location is between the W fiber and the ZrO_x/Zr m coating; b) the debonding location is between the ZrO_x/Zr m coating and the W matrix; c) ZrO_x/Zr m coating is flaked away from W fiber

Figure 4.24 shows microstructure images of the ZrO_x/W m interface after the push-out test. Its debonding feature is relatively similar to that of the ZrO_x/Zr m interface (see Figs. 4.24 a and b). There are also some cracks present in the ZrO_x /W multilayer coating (see Figs. 4.24 c and d).

The ErO_x/W m interface shows a debonding behavior quite similar to that of the ZrO_x/W m interface (see Fig. 4.25), while the Er/W m interface shows a different one (see Fig. 4.26): the debonding location lies mainly in one Er layer; the crack extends

through the multilayer changing the debonding path from one Er layer to another, which indicates that the Er layer is the weakest layer in the Er/W multilayer coating.

The debonding behavior of Cu/W m interface is discussed in the next chapter.

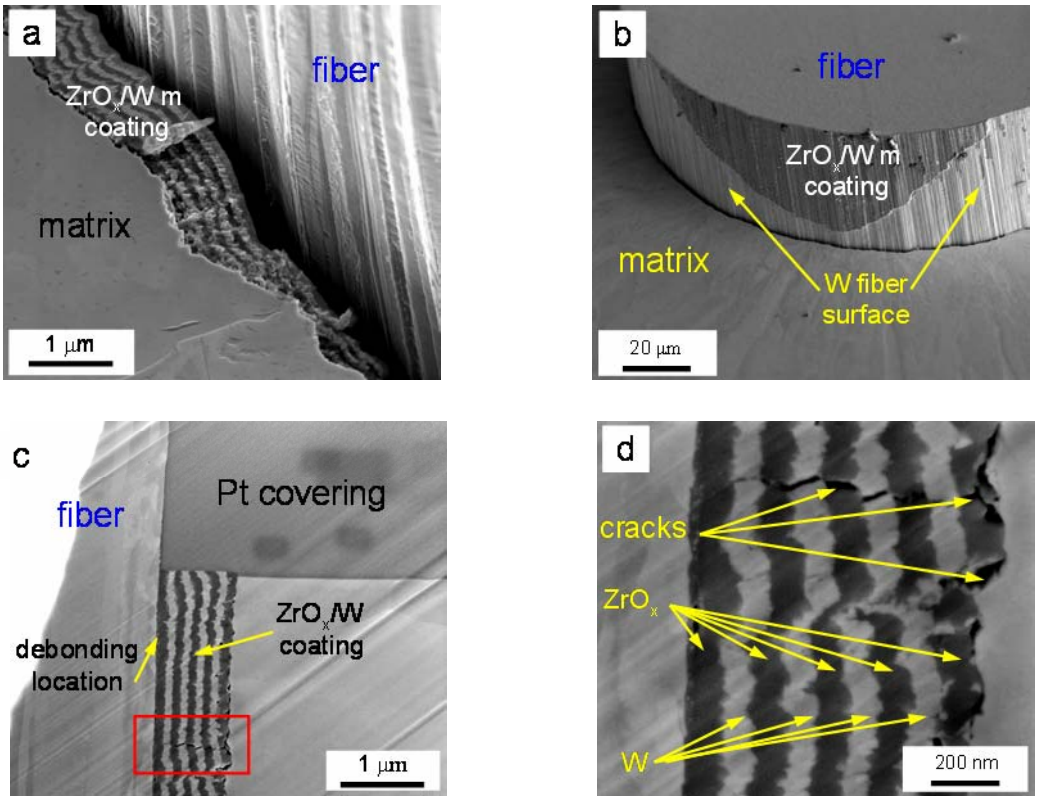

Figure 4.24. SEM images of ZrO_x/W m interface specimen after push-out test: a) ZrO_x/W m coating remained in the W matrix; b) part of the ZrO_x/W m coating attached to the W fiber; c) the debonding location lies between the W fiber and the ZrO_x/W m coating; d) micro-cracks in the ZrO_x/W m

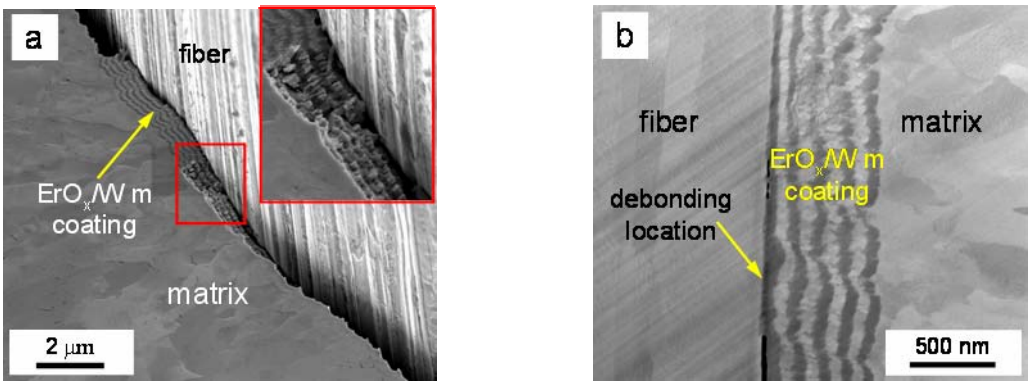

Figure 4.25. SEM images of ErO_x/W m interface specimen after the push-out test: a) step-like structure in the ErO_x/W m coating; b) the debonding location is between the W fiber and the ErO_x/W m coating

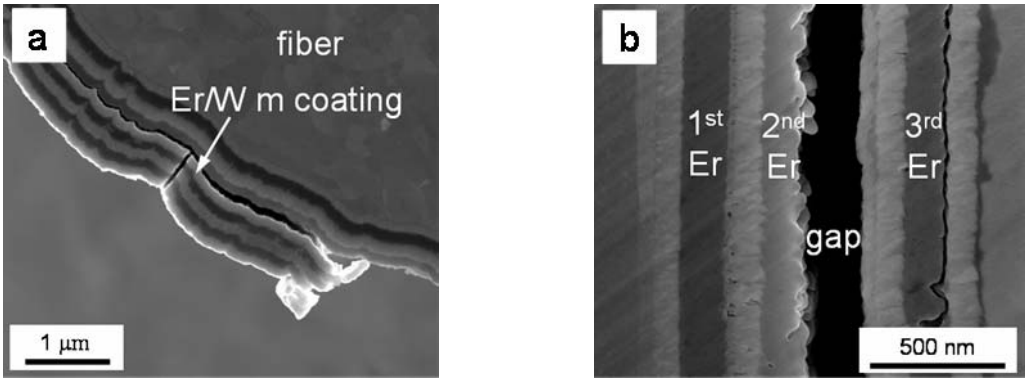

Figure 4.26. SEM images of Er/W m specimen after the push-out test: a) cracks lie in the Er/W multilayer coating; b) the debonding location lies in 2nd Er layer

Thus, it can be concluded that during the push-out process, specimens with multilayer interfaces (ZrO_x/Zr m, ZrO_x/W m, and ErO_x/W m) have similar debonding locations, which are either lying between the W fiber and the interface coating or between the interface coating and the W matrix; crack deflection (step-like structure) occurred in the multilayers. These interfacial fracture behaviors coincided with the motivation of the interface design (fit types b2) and d)). The Er/W m interface specimen contains crack propagation in the multilayer coating and the debonding in the Er layers, which fits to types b 1) and d).

4.2.4 Cu interface

4.2.4.1 Push-out curve

Figure 4.27 shows the push-out curves of specimens with the Cu interfaces, which include Cu 170, Cu 480, and Cu/W m. Table 4.3 shows the information about average energy absorption Δ, the specimen thickness H, the maximum debonding load P_{max}, the frictional sliding load P_{fr}, and the dynamic displacement d_0 of each Cu interface. In the initial loading phase (see Fig. 4.27), the three interfaces showed similar linear responses to that of the oxide interfaces and multilayer interfaces. The Cu 170 and the Cu/W m interfaces have steeper slopes than the Cu 480 interface. The copper coatings were annealed in the CVD fabrication process and are thus supposed to be very soft. Therefore, a great plastic flow is expected in the load bearing process. Since the fiber displacement includes the compliance of the specimen, the shear strain of the coating layers, as well as the deformation or fracture of the coating. The Cu 480 interface had a large plastic deformation leading to a low slope in the first loading phase. The Cu 170 and Cu/W m interfaces did not undergo a large plastic flow as that of the Cu 480

interface due to the limited thickness of the Cu coatings (170 nm for the Cu 170 and 100 nm for the Cu/W m). The yield stress of the copper film increases by several orders of magnitude when its thickness is reduced below micrometer range due to the severely limited dislocation movement in the thickness direction [73].

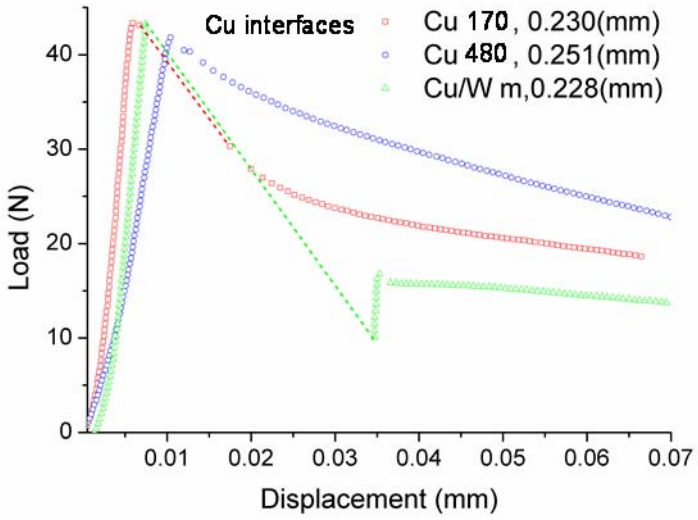

Figure 4.27. Push-out curves for the Cu interfaces

Table 4.3. The specimen thickness H, the maximum debonding load P_{max}, the frictional sliding load P_{fr}, the dynamic displacement d_0 and the average energy absorption Δ of Cu interfaces.

Interface	H (mm)	P_{max} (N)	P_{fr} (N)	d_0 (μm)	Δ (kJ/m^2)
Cu/W m	0.228	43.5	16.8	28	13.1
Cu 170	0.230	43.1	30.45	11.5	15.8
Cu 480	0.251	42	-	-	17.2

After the complete debonding event, the curve of Cu/W m interface shows a characteristic which is typical of the oxide interfaces. The friction load P_{fr} is clearly distinguishable. It indicates that Cu/W m interface has a brittle fracture behavior although it contains Cu (Fig. 4.27 green triangles). The characteristic shape of the curve suggests that the capability of the plastic flow of the Cu in the Cu/W multilayer coating was strongly restricted by the size effect. The Cu 170 interface has another curve shape. It has a limited dynamic movement but no load rise. This phenomenon is believed to be due to the plastic deformation of the Cu coating which consumed a lot of stored energy. However, the Cu 480 interface shows a unique curve shape: it has no dynamic movement, and its sliding load is difficult to distinguish from the debonding load. Such behavior would be caused by a strong deformation of Cu both before and after complete

debonding. The explanations given above are supported by the microstructure investigation results. Fig. 4.28 shows SEM images of the Cu interfaces after the push-out test.

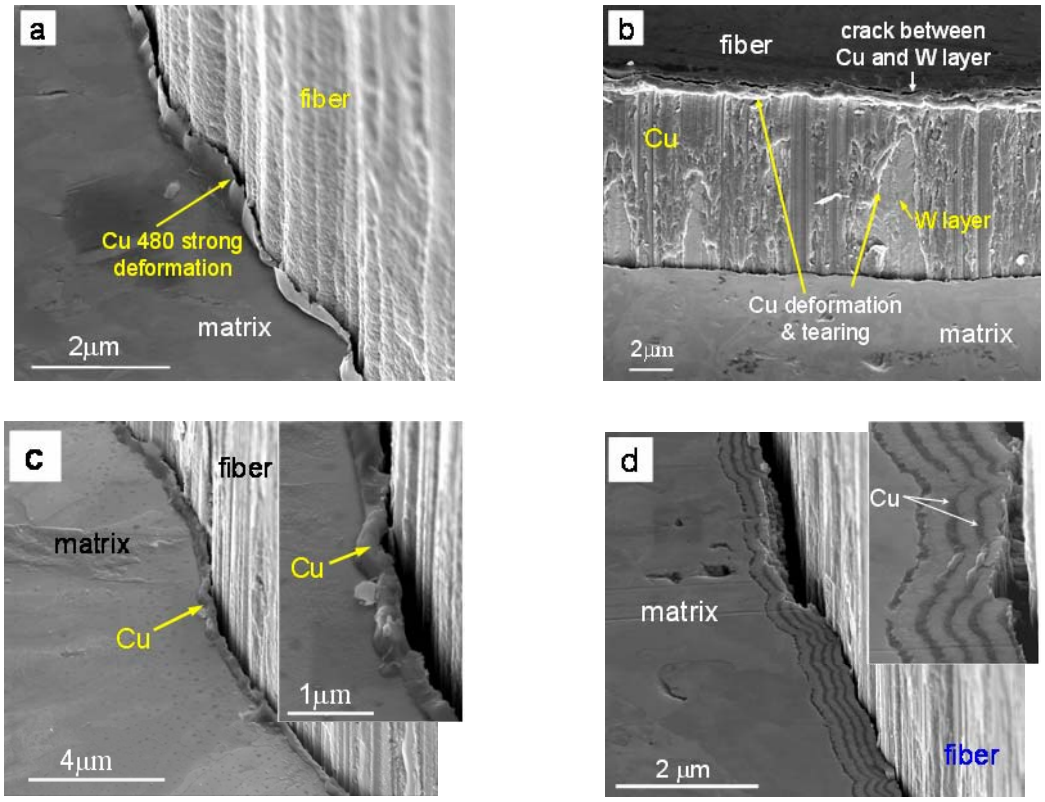

Figure 4.28. SEM images of the specimens with Cu interfaces after the push-out test: a) strong deformation of the Cu 480 layer; b) teared Cu 480 layer; c) moderate deformation of Cu 170; d) limited deformation of the Cu layer in Cu/W m interface

The Cu in the Cu 480 (see Figs. 4.28 a and b) specimen shows strongest plastic deformation and the Cu in the Cu 170 (see Fig. 4.28 c) specimen shows a moderate plastic deformation, while the Cu deformation in the Cu/W m specimen (see Fig. 4.28 d) is greatly restricted.

The microstructure investigation results are also in agreement with the average energy absorption Δ estimation results. The different amount of Cu deformation caused different average energy absorption (17.2 kJ/m^2 for Cu 480, 15.8 kJ/m^2 for Cu 170, and 13.1 kJ/m^2 for Cu/W m interfaces).

4.2.4.2 Interfacial parameter calibration

The curve fitting results of the interfacial shear strength τ_d, the interface radial stress σ_R, the friction coefficient μ, the asperity caused shear stress τ_R, and the interfacial fracture energy Γ_i of the Cu interfaces are shown in Fig. 4.29.

4.2.4 Cu interface

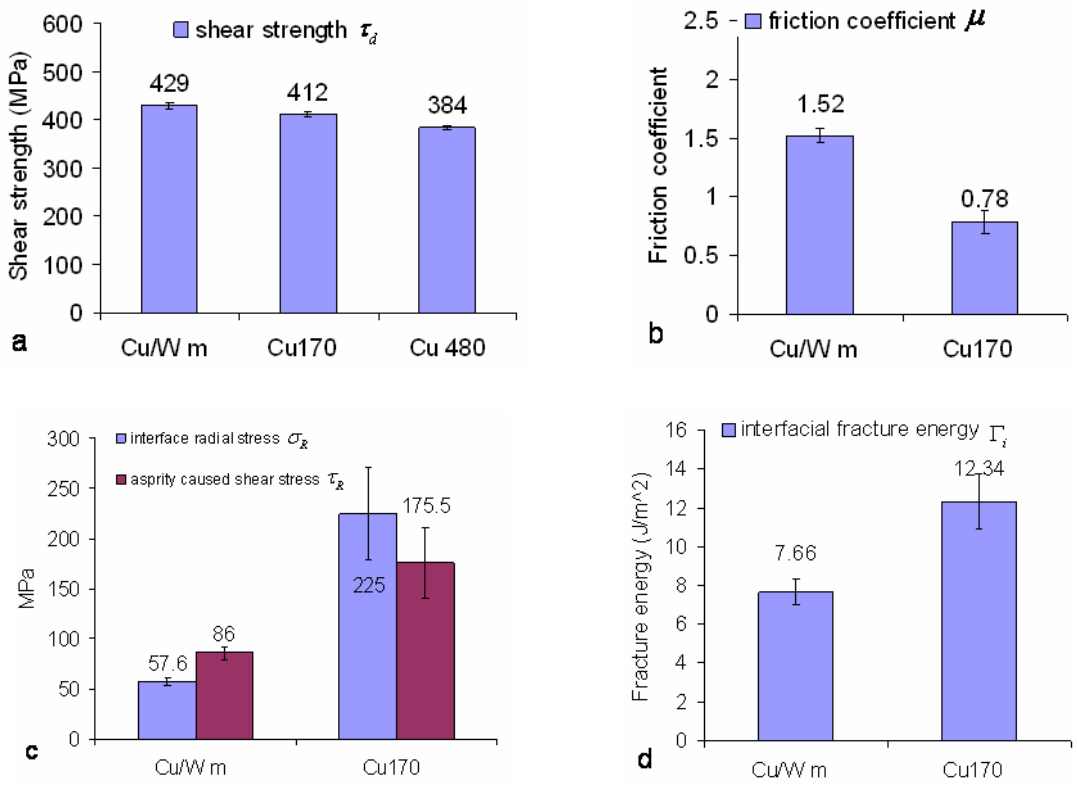

Figure 4.29. The curve fitting results for Cu interfaces: a) the interfacial shear strength τ_d; b) the friction coefficient μ; c) the interface radial stress σ_R and the asperity caused shear stress τ_R; d) the interfacial fracture energy Γ_i

Since the Eqs. (2.16) and (2.18) were derived within the framework of the linear elastic fracture mechanics and elastic shear-lag assumption, its validity is limited within a small scale yielding case. Thus this approach is less adequate for the Cu 480 interface due to the large scale plastic flow. Therefore, the σ_R, μ, τ_R, and Γ_i were only calibrated for Cu/W m and Cu 170 interfaces. The lowest load bearing ability is found in Cu 480 interface due to the large deformation of Cu (shear strength τ_d is 384 MPa). The Cu/W m and Cu 170 interfaces have relatively high τ_d, 429 MPa and 412 MPa, respectively. All Cu interfaces have much higher interfacial fracture energy compared to the oxide interfaces and multilayer interfaces. Cu 170 has extremely high fracture energy which is 12.34 J/m^2. Cu/W m has a fracture energy of 7.66 J/m^2, which is two times larger than the average fracture energy of the oxide interfaces (3 J/m^2).

4.2.4.3 Microstructure of the interface after the push-out test

Figure 4.30 shows SEM images of the Cu 170 specimen after the push-out test. The debonding location is in the Cu layer (see Fig. 4.30 a); the Cu layer was split due to the shear stress, part of it attached to the fiber while the other part of it remained in the

matrix (see Fig. 4.30 b); and the Cu coating close to the sample surface was squeezed out when it was subjected to a strong shear stress due to its ductile property (see Fig. 4.30 c). All these findings indicate that a great mount of energy absorption is required for the failure of Cu during the push-out process. It can be concluded that the high interfacial fracture energy of the Cu 170 may be due to the deformation and rupture of the Cu.

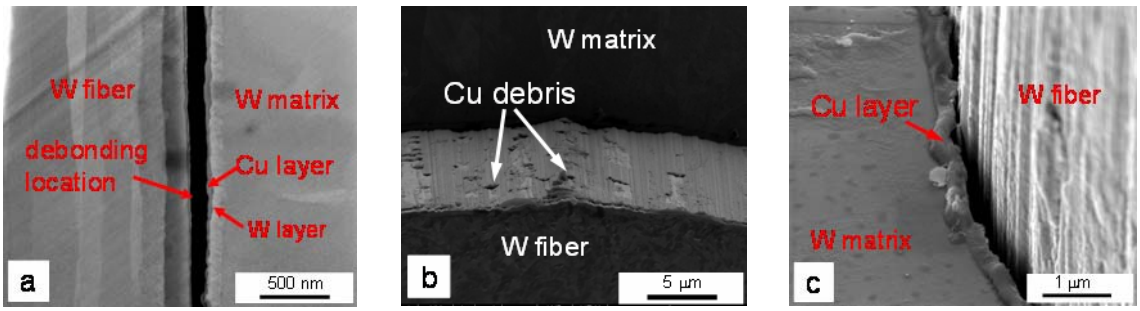

Figure 4.30. SEM images of the Cu 170 specimen after the push-out test: a) the debonding location lies in the Cu layer; b) debris on the fiber; c) Cu layer is squeezed out

Figure 4.31 shows SEM images of the Cu/W multilayer specimen after the push-out test. Fig. 4.31 a shows a cross-section image of the interface indicating that the debonding location is in the first Cu layer (counting from the fiber side). However, the debonding location changes from one Cu layer to another (see Fig. 4.31 b). This is also confirmed by the step-like structure of the Cu/W multilayer interface shown in Fig. 4.28 d. The deformation of the Cu is relatively limited due to the small width of the Cu layer (see Fig. 4.31 c). Nevertheless, crack progression in the multilayer, as well as fracture and deformation of the Cu layer, cause relatively large amounts of energy absorption.

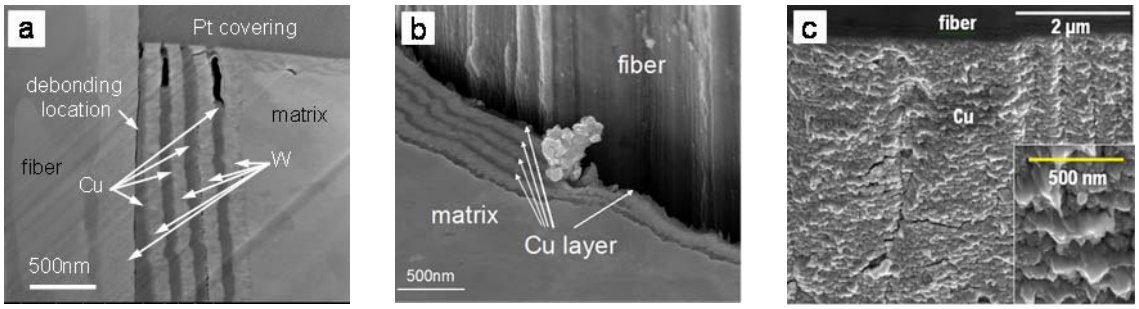

Figure 4.31. SEM image of the Cu/W m specimen after the push-out test: a) the debonding location lies in the 1st Cu layer; b) the debonding location changed from the 1st Cu layer into the 4th Cu layer; c) limited deformation of the Cu layer

The specimens with Cu interfaces show expected interfacial fracture behavior which are in accordance to the interface design motivation (fit types b) and d)).

4.2.5 Carbon interface

4.2.5.1 Push-out curve

A push-out curve of the carbon (C) coating is shown in Fig. 4.32. The curve shape is similar to that of the other brittle debonding case. However, the values of maximum debonding load $P_{\max}$ (40.5 N) and the maximum friction load P_{fr} (14.2 N) are much smaller than the other interfaces. The average energy absorption Δ and dynamic displacement d_0 of the C interface specimen are 9.8 kJ/m^2 and 30 μm, respectively. Since magnetron-sputtered carbon is amorphous, which is much softer than the oxide coating, a lower load bearing capability is expected.

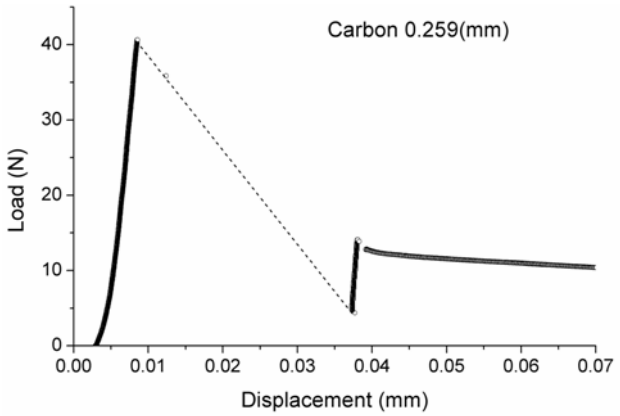

Figure 4.32. Push-out curve for the specimen with carbon interface

4.2.5.2 Interfacial parameter calibration

The calibrated results of interfacial parameters for the carbon interface are shown in Table 4.4.

Table 4.4. The calibrated results of interfacial parameters of the C interface.

Interfacial shear strength, τ_d (MPa)	Friction coefficient, μ	Interface radial stress, σ_R (MPa)	Asperity caused shear stress, τ_R (MPa)	Interfacial fracture energy, Γ_i (J/m^2)
284±5	1.04±0.06	71±8	74±8	7.4±0.7

It can be found that the C interface has relatively low shear strength and asperity caused shear stress but very high fracture energy compared to the other interfaces discussed above.

4.2.5.3 Microstructure of the interface after push-out test

The microstructure images of the C interface after the push-out test show that the interlayers were delaminated during the push-out process (see Fig. 4.33 a), indicating that the bonding is not strong between the layers. Due to the lubricating property of carbon, there is no dust or debris in the delaminated layers. The debonding mainly happened along the carbon layers (see Fig. 4.33 b). The fiber was sliding out in this lubricating environment, and therefore, the friction coefficient was low. The large fracture energy may be due to the interlayer delamination and the rupture of the C coating. The interfacial debonding behavior of C interface fits to the type b 1) (see Fig. 2.8).

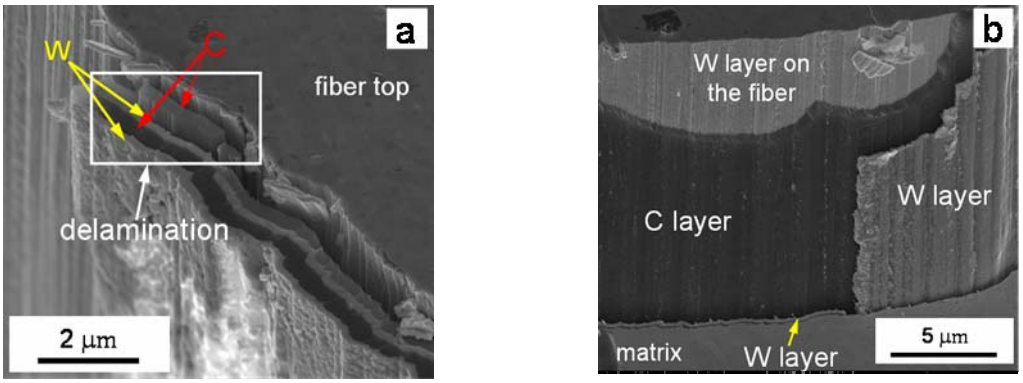

Figure 4.33. SEM image of carbon interface specimen after the push-out test: a) delamination of the interface coating; b) the debonding location lies along the carbon layer rather than in the carbon layer

4.3 Push-back test

The representative push-back curves for each interface type are shown in Fig. 4.34. For comparison, the corresponding push-out curves are also included.

Figure 4.34 a shows the result for the ZrO_x&W 260 interface. The push-back curve shows a similar linear load-displacement relationship as the one for the push-out until the load reaches a certain value (point A). The load decreases slightly after point A (due to the change from static to dynamic friction) and remains at a certain value until the fiber is pushed into its original position (point B). The load has a small hump up at point B since the fiber has to move over the originally matched position (at point B) and begin to under go a new mismatch (after point B). The average sliding load (see Fig. 4.34 a) represents the friction of the interfaces when the fiber was sliding in the matrix. The value of the average sliding load is approximately equal to the load value of the final stage of the push-out test. This coherence is due to the identical embedded length in the two cases.

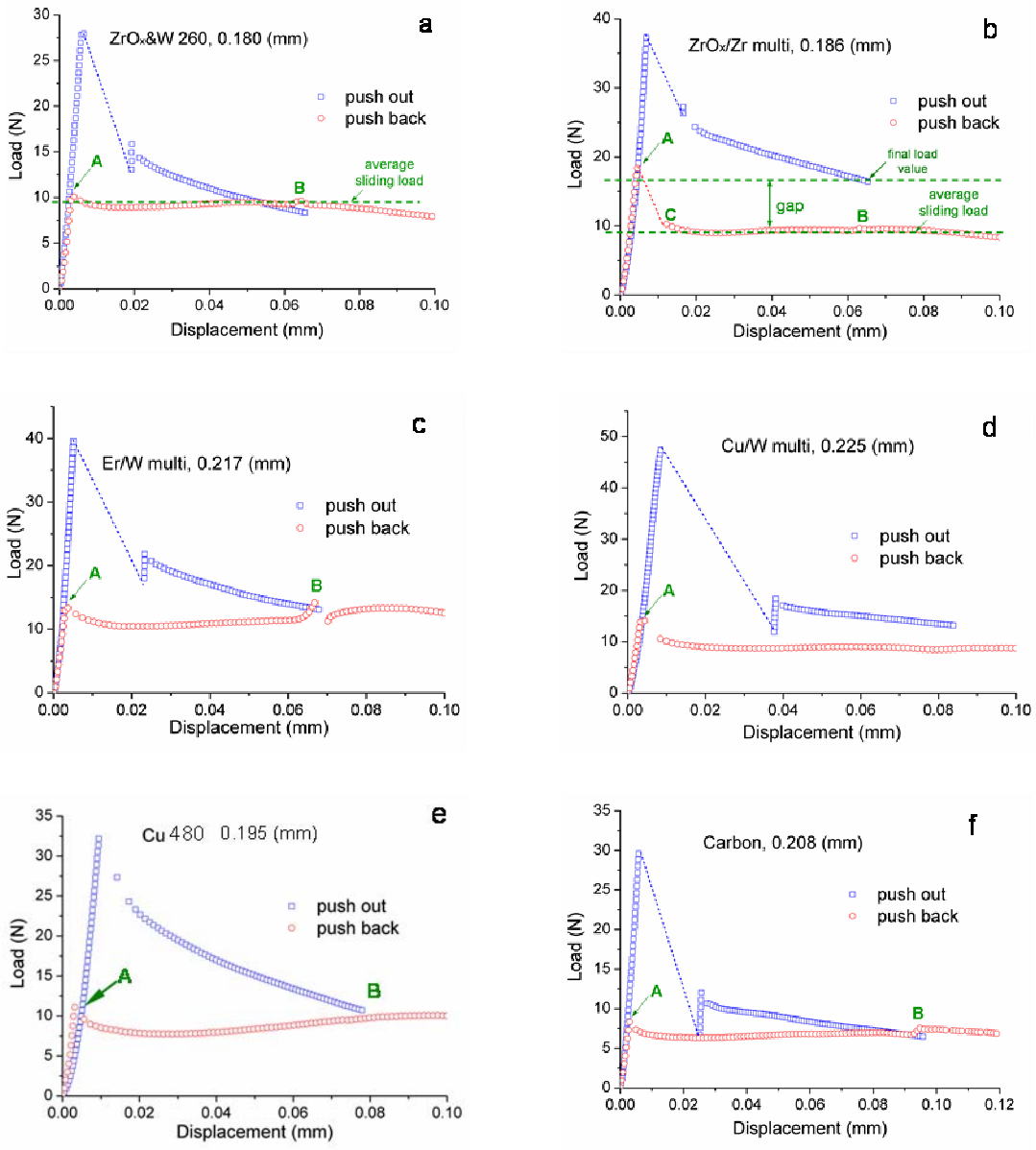

Figure 4.34. Push-back test results: a) ZrO_x&W 260 interface; b) ZrO_x/Zr multilayer interface; c) Er/W multilayer interface; d) Cu/W multilayer interface; e) Cu 480 interface; f) carbon interface

Figure 4.34 b shows the push back result of the ZrO_x/Zr m interface specimen. There is an obvious load drop after having reached point A. The average sliding load value (see Fig. 4.34 b) did not reach the final load value of the push-out test: the gap between the two values is larger than 6 N. This may be explained as follows. When the fiber was moving along in the opposite direction after the push-out test, it caused heavy damage to the debonded interfaces. The load drop after point A is an indication of a second

debonding, after which, the interfaces are damaged more severely, leading to a smaller friction roughness at these debonded interfaces.

The Er/W multilayer interface (see Fig. 4.34 c) shows push-back behavior similar to that of the ZrO_x&W 260 interface specimen.

The Cu interfaces (Cu/W m in Fig. 4.34 d and Cu 480 in Fig. 4.34 e) show a different behavior. There is no obvious load change when the fiber reaches its original position; it is difficult to detect point B. This phenomenon is caused by the plastic deformation of the Cu coating, which produced similar friction values for both the matched or non-matched positions.

The carbon interface (Fig. 4.34 f) shows push-back behavior similar to that of the ZrO_x&W 260 interface specimen.

There is no obvious reseating drop in any of the W_f/W_m composites.

According to the push-back curves, the average sliding stress $\tau_{sliding}$ of the debonded interfaces can be estimated by dividing the average friction loads by their corresponding contacting area. The estimated values are shown in Table 4.5. It is found that specimens with the brittle interfaces (ZrO_x&W 260, ZrO_x/Zr m and Er/W m) have similar average sliding stress whereas the carbon interface specimen has the smallest sliding stress and the Cu interfaces (Cu/W m, Cu 480) specimens have a moderate sliding stress.

Table 4.5. Average sliding stress $\tau_{sliding}$ calculated according to push-back test curves.

Interface	Sliding length (mm)	Average sliding load (N)	Average sliding stress, $\tau_{sliding}$ (MPa)
ZrO_x&W 260	0.180	9.2	108
ZrO_x/Zr m	0.186	9.2	105
Er/W m	0.217	10.8	106
Cu/W m	0.225	8.8	83
Cu 480	0.195	8.7	95
carbon	0.208	6.7	68

4.4 Three points bending test

4.4.1 Direct demonstration of the crack deflection

The direct observation of the crack deflection was performed using in-situ SEM imaging during the three points bending (3PB) test. The load and the corresponding platform displacement were recorded to generate the load-displacement curve.

Figure 4.35 shows the W_f/W_m composite with an oxide interface (ZrO_x&W 260) during the 3PB test.

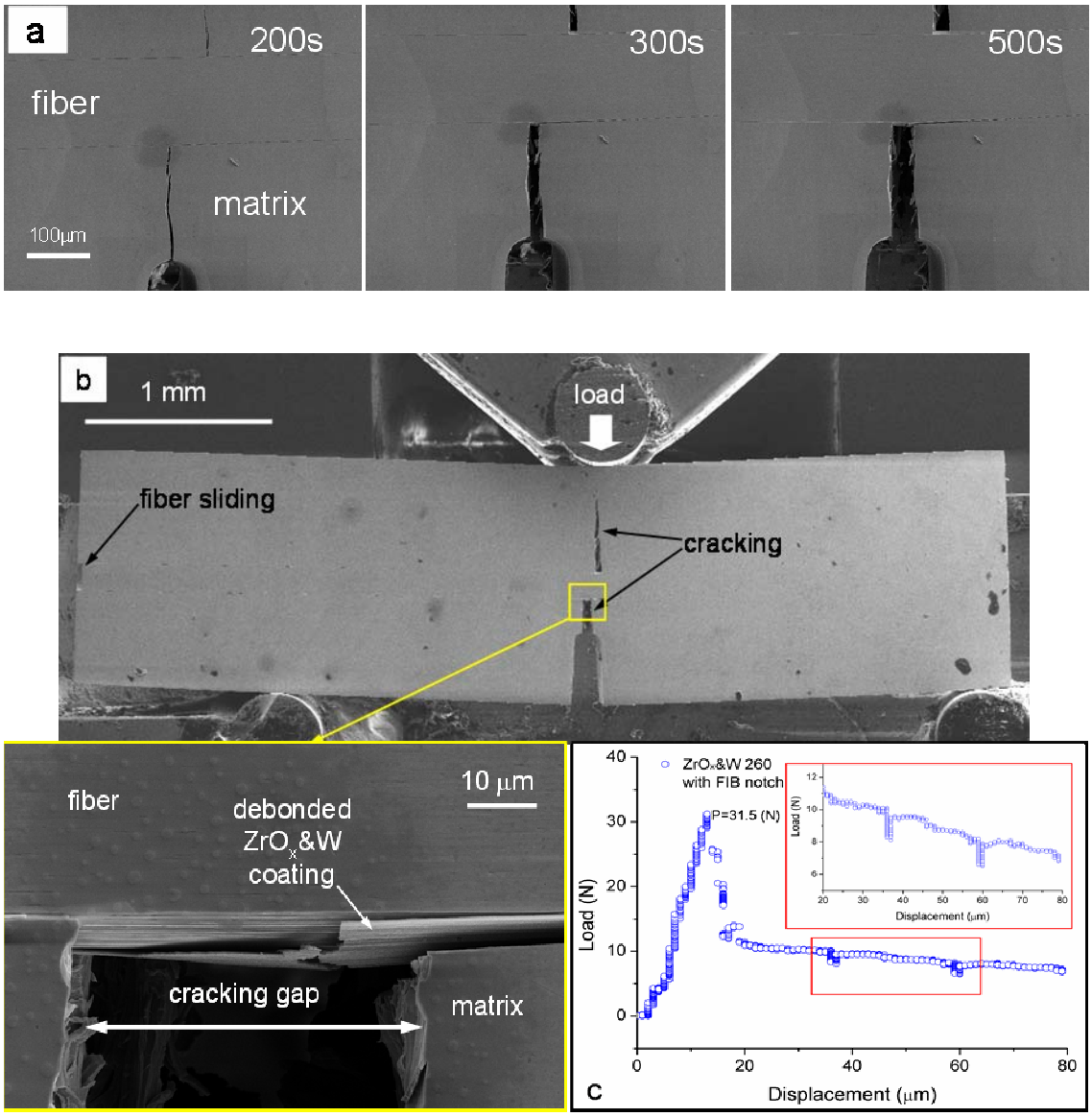

Figure 4.35. SEM images of W_f/W_m composite with the ZrO_x&W 260 interface during the 3-point bending test: a) the crack propagation; b) the interfacial debonding; c) the load-displacement curve

In order to introduce a precise initial crack and well-defined crack propagation, a sharp notch was cut via the FIB technique on the bottom of the diamond-grinded notch (see chapter 3.2.2). Fig. 4.35 a shows the crack propagation process (images were taken at different testing times), while Fig. 4.35 b shows images at the end of the test. The load-displacement curve of this specimen is included as well (see Fig. 4.35 c).

The crack deflected along the interface when it met the interface (see Fig. 4.35 b). The fiber contained neither crack nor clear deformations. At one end of the specimen, the fiber glided into the interior from the original location (pull-in), which indicates that the interfacial debonding propagated through the entire half of the specimen (see Fig. 4.35 b). The interface debonding and fiber sliding led to the limited fiber strain. The interfacial debonding behavior was also supported by the load-displacement curve result. In Fig. 4.35 c, the applied load raised until 31.5 N then dropped to 10 N. indicating the initial propagation of the crack. Then, the crack propagated progressively causing gradual decrease of the load (see Fig. 4.35 c).

Figure 4.36 a and shows the SEM images of W_f/W_m composite with a multilayer interface (ZrO_x/Zr m) after the 3PB test while Fig. 4.36 b contains the load-displacement curve.

For comparison, the initial crack of ZrO_x/Zr m specimen was introduced by diamond grinding with a notch width of 70 μm.

The crack propagation process was not observed during the test. Until the applied load reached the rupture value (110 N) there was no sign of any failure (see Fig. 4.36 b). When the load reached 110 N, a transverse crack was abruptly produced from the notch root and propagated rapidly in opening mode perpendicular to the specimen axis but without cutting the fiber. The sharp crack plane extended though the matrix surrounding the fiber. This abrupt rupture was in accordance with the load-displacement curve result—no gradual load decrease was observed after the fracture. The crack in the matrix is typical of an intergranular type (see Fig. 4.36 a). No crack or clear deformation was found in the fiber, while fiber pull-in was observed at one end of the specimen (see Fig. 4.36 a), which is exactly the same as the ZrO_x&W 260specimen case. The ZrO_x&W 260 specimen and the ZrO_x/Zr m specimen had similar interfacial debonding behavior during the 3PB test, while the FIB notch had introduced the progressive crack propagation.

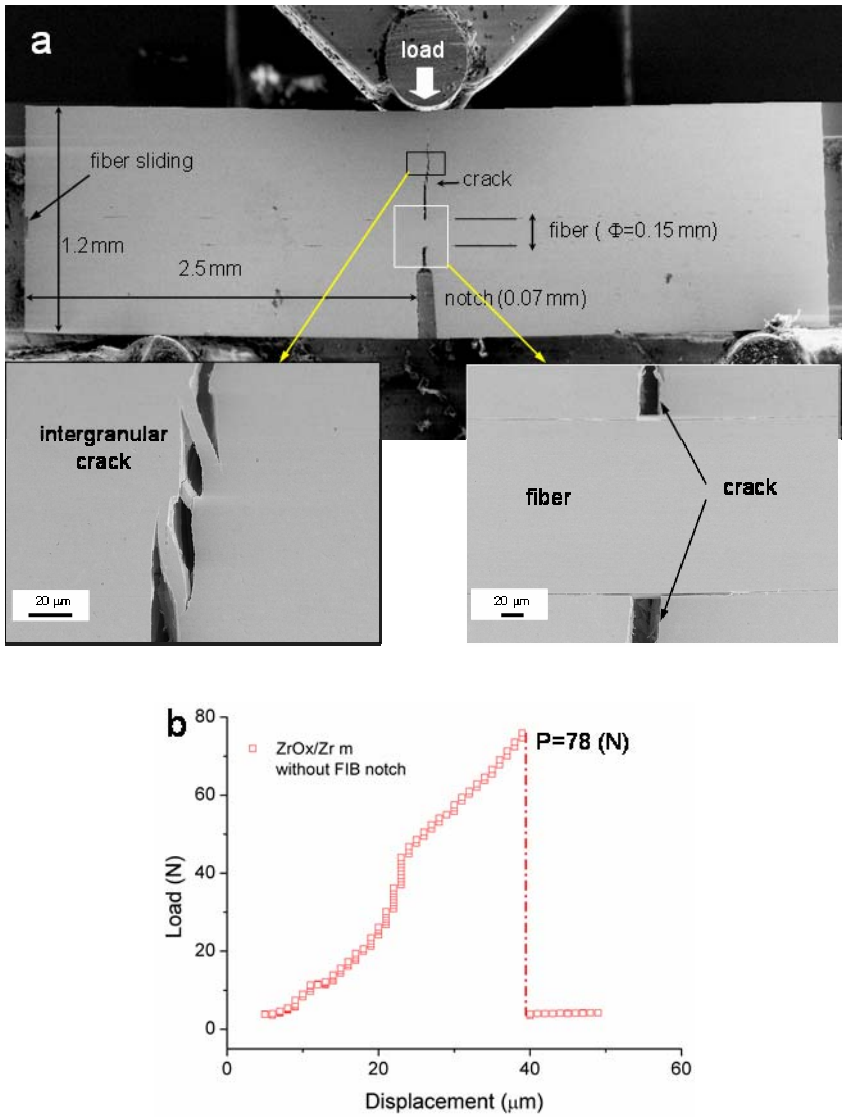

Figure 4.36. a) SEM images of W_f/W_m composite with the ZrO_x/Zr multilayer interface after the 3PB test; b) the load-displacement curve

Figures 4.37 a and b show SEM images of Cu 480 interface specimen during the 3PB test while Fig. 4.37 c illustrates the load-displacement curve. The initial crack was created via the FIB technique on the bottom of the diamond grinding notch. Therefore, the crack propagation was also observed (see Fig. 4.37 a). Fig. 4.37 b shows images at the end of the test which indicates that: the interfacial debonding occurred during 3PB test; the crack started at the bottom of the notch, then extented around the fiber and finally appeared on the other side of the matrix; there is no obvious cracking in the fiber. Unlike the brittle interface specimen, the Cu 480 interface specimen has no fiber dislocation at the specimen end, but a rather strong fiber deformation in the specimen center.

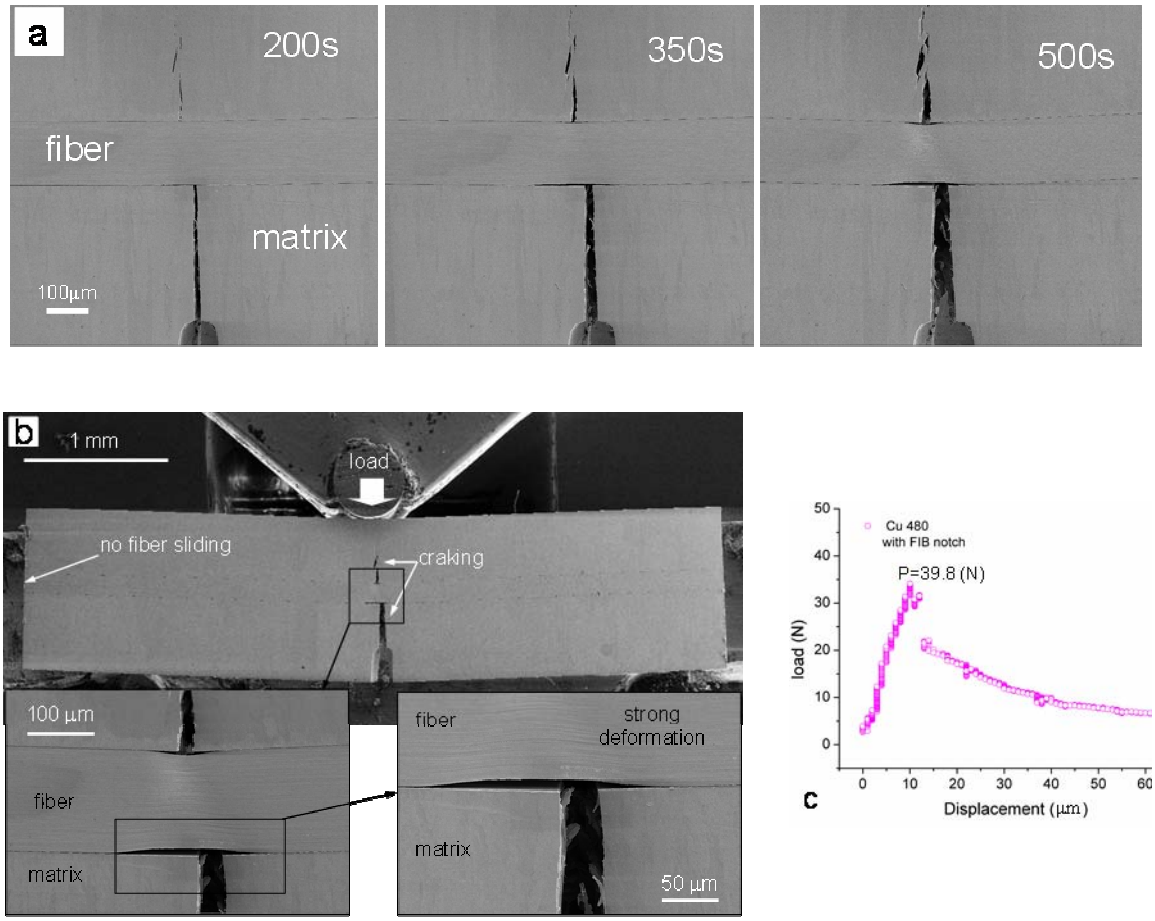

Figure 4.37. SEM images of W_f/W_m composite with the Cu 480 interface during the 3PB test: a) the crack propagation; b) the interfacial debonding and strain in the fiber; c) the load-displacement curve

4.4.2 Load-displacement curve—W matrix fracture toughness

The load-displacement curve contains information about the fracture toughness of the specimen.

The 3PB test is widely used to measure material fracture toughness when specimens are prepared according to certain dimension requirements [155]. The fracture toughness of the specimen can be calculated using the maximum bearing load as well as the specimen dimension data. Five specimens were subjected to the 3PB test. The calculated fracture toughness K_1 of each specimen are shown in Fig. 4.38: the average value is 6.76 MPa·$m^{1/2}$. In the W_f/W_m composite, the specimen was held by the W fiber at the end of the 3PB test; the maximum applied load was sustained mainly by the matrix. Therefore, the obtained fracture toughness represents the fracture toughness of the W matrix. Indeed, this calculated value is consistent with results obtained in other works [156]. Converted to a fracture energy, it becomes 114 J/m^2.

Therefore, the fracture energy of the W matrix in this thesis is determined to be 114 J/m^2.

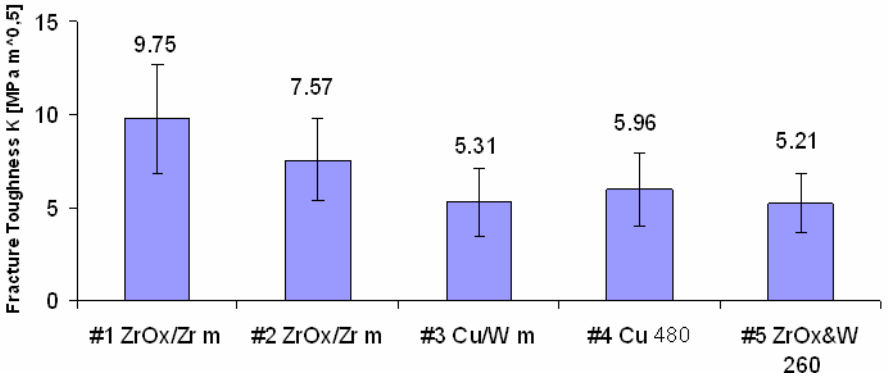

Figure 4.38. Fracture toughness K_I of W_f/W_m composites obtained by the 3PB test

4.5 Thermal stability investigation

In order to examine the thermal stability of these W_f/W_m composites, some specimens were selected and put into a vacuum furnace for 10 hours at 800 °C.

The same push-out test and curve fitting method were applied to the specimens after the heat treatment. The results are shown in Fig. 4.39, together with the results of the specimens without heat-treatment.

Most interfaces exhibit no significant changes in terms of interface shear strength τ_d and asperity caused shear stress τ_R, although there are some changes where the interface radial stress σ_R and friction coefficient μ are concerned. The Er/W m interface, the ZrO_x&W 260 interface and the ZrO_x/Zr m interface show very similar fracture energy Γ_i compared to the corresponding interface without heat treatment, while the Cu/W m interface and the carbon interface show clear changes compared to the ones without heat treatment. These phenomena can be explained with the assistance of a microstructure investigation.

The cross-section images of the Er/W multilayer, the ZrO_x&W 260, and the ZrO_x/Zr multilayer interfaces are shown in Figs. 4.40, 4.41, and 4.42, respectively, including the images with and without heat treatment. It is apparent that similar debonding locations occurred in the three interfaces both with and without heat treatment although the grain growth was found in the Er/W multilayer and ZrO_x&W 260 interfaces; and diffusion occurred in the ZrO_x/Zr multilayer interface. These findings indicate that apart from the few changes in terms of the microstructure, these three interfaces have a good thermal stability in terms of the debonding location, and eventually in terms of the fracture energy.

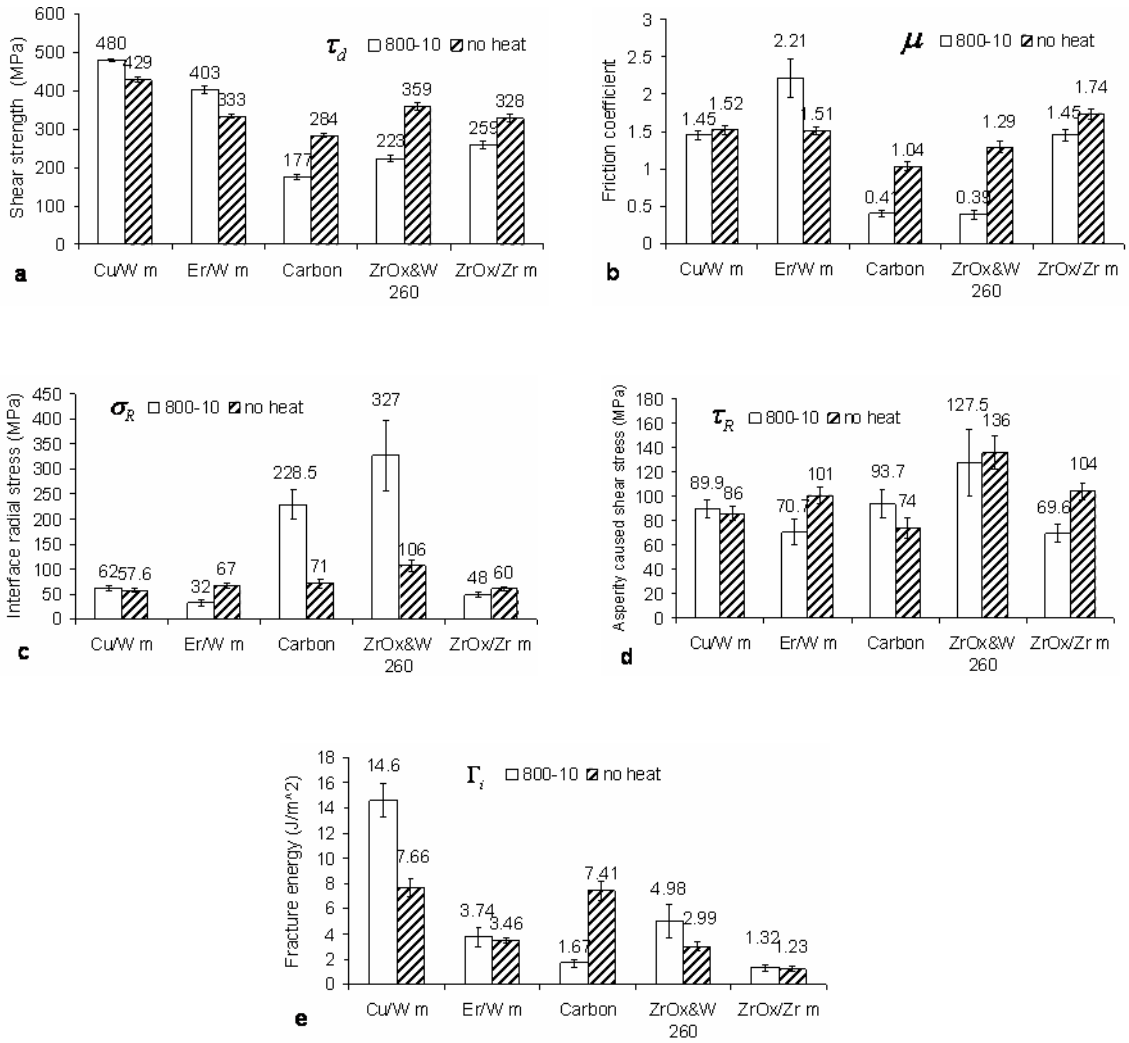

Figure 4.39. Comparisons of interfacial parameters of specimens with and without heat treatment: a) the interfacial shear strength τ_d; b) the friction coefficient μ; c) the interface radial stress σ_R; d) the asperity caused shear stress τ_R; e) the interfacial fracture energy Γ_i

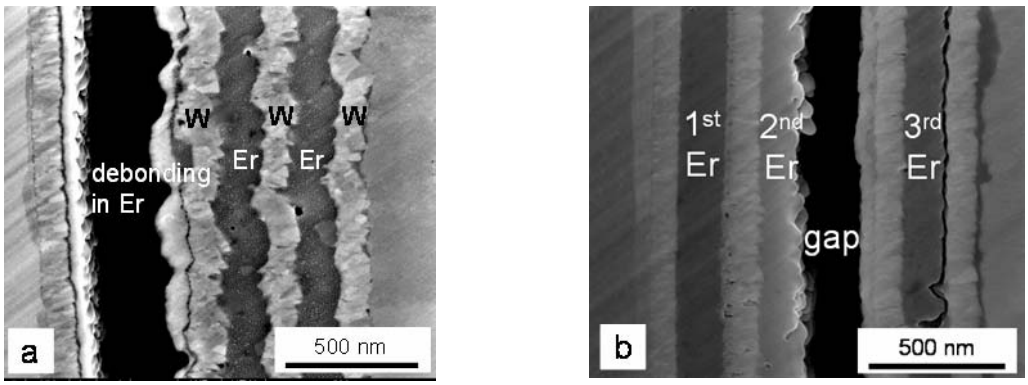

Figure 4.40. SEM images of Er/W m interface: a) with heat treatment; b) without heat treatment

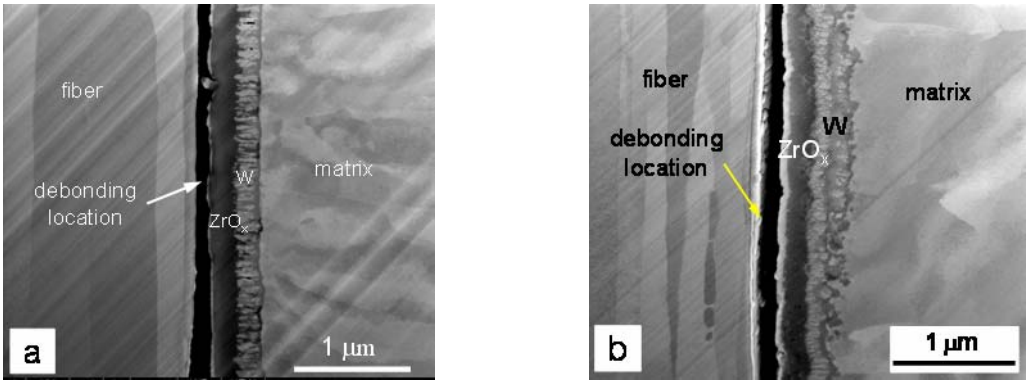

Figure 4.41. SEM images of the ZrO_x&W 260 interface: a) with heat treatment; b) without heat treatment

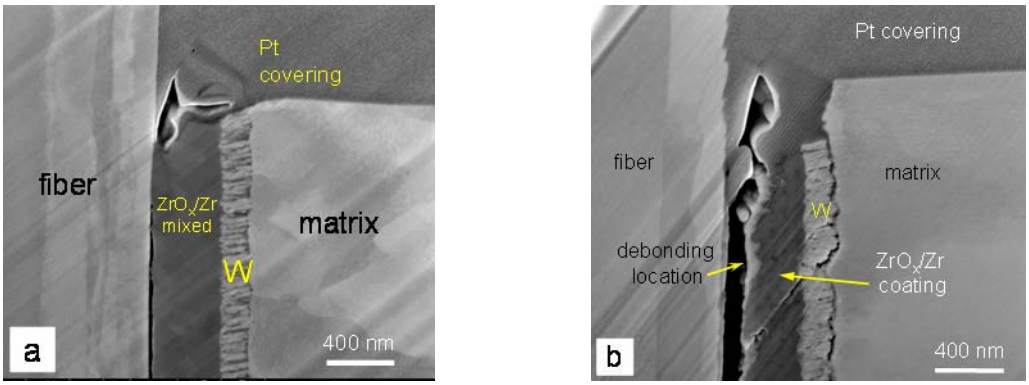

Figure 4.42. SEM images of the ZrO_x/Zr m interface: a) with heat treatment; b) without heat treatment

Figure 4.43 shows cross-section images of the specimen with and without heat treatment for the Cu/W multilayer interface. Before the heat treatment, the multilayer was amorphously arranged (see Fig. 4.43 b). After heat treatment, grain growth occurred in both Cu and W layers although the multilayer structure remains unchanged (see Fig. 4.43 a). More damage was found in the W layer (see Fig. 4.43 a) indicating the strength of the W layer decreased due to the grain growth.

No obvious change in the debonding location was found in the carbon layer. The interlayer delamination and carbon layer rupture occurred in both with and without heat treatment (see Figs. 4.44 a and b). On the other hand, the grain growth was found in the W layer. (see Fig. 4.44 c). The chemical analysis results (see Fig. 4.44 d) show that the layer arrangement after heat treatment stays the same as the one without heat treatment except some diffusion occurred on the edges of the layers. It is well-known that magnetron sputtering deposited carbon is amorphous carbon which contains small amount of graphite structure. When the specimens were heated to 800°C for 10 hours,

part of amorphous carbon was transformed into a graphite structure. Graphite has less toughness and strength than amorphous carbon. Therefore, the interface shows a lower fracture energy and interfacial shear strength after the heat treatment. Further, graphite has a much better lubricative property, which leads the decrease of the friction coefficient.

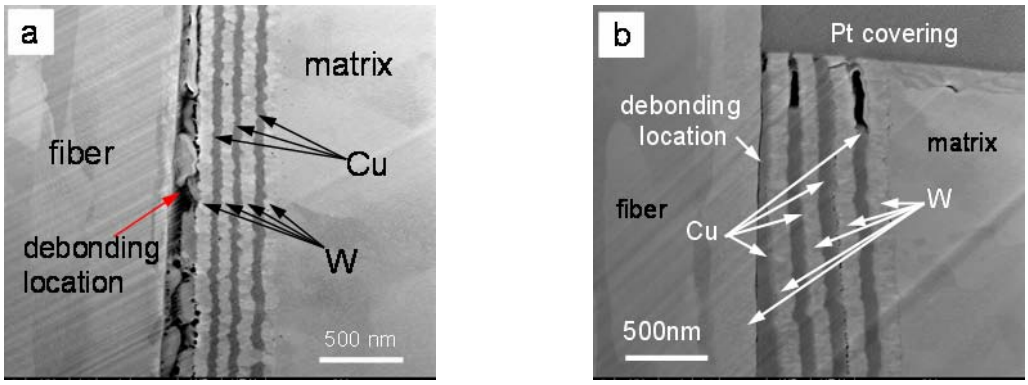

Figure 4.43. SEM images of the Cu/W m interface: a) with heat treatment; b) without heat treatment

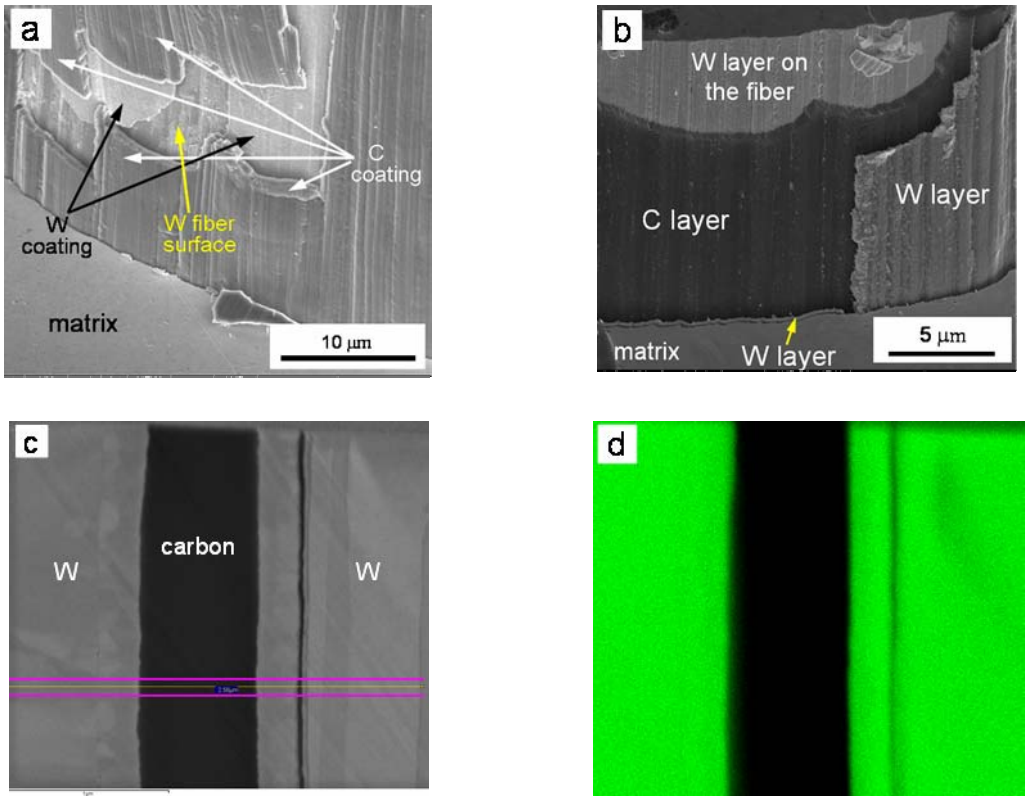

Figure 4.44. a) carbon rupture in the specimen after heat treatment; b) interface delamination in the specimen before heat treatment; c) cross-section image of the carbon interface after heat treatment; d) EDXS mapping of W in area shown in Fig. 4.44 c

It can be concluded that, among the investigated interfaces, the oxide coating (ZrO_x&W 260), the multilayer coatings (Er/W m and ZrO_x/Zr m), show a good thermal stability in terms of the interfacial fracture behavior, while the interfacial fracture behavior of the Cu/W m interface and the carbon interface were strongly affected by the heat treatment.

4.6 Mechanical property prediction of W_f/W_m composite

Based on the properties of fiber, matrix, and interface described above, the mechanical property (stress-strain curve) of W_f/W_m composite with each interface can be predicted. Following the procedure introduced in chapter 2.4, the results of the critical stress and strain are shown as follows.

The utilized material parameters for fiber and matrix were read from Table 3.1 and Table 3.3, respectively. The interfacial parameters (asperity caused shear stress τ_R and interfacial fracture energy Γ_i were taken from the calibration results in chapter 4.2. The fiber volume fraction is assumed as 0.6.

(1) Matrix cracking stress σ_{mc} and strain ε_{mc}

The matrix cracking stress σ_{mc} was calculated by solving Eq. (2.29). The corresponding strain ε_{mc}, was calculate by

$$\varepsilon = \frac{\sigma_{mc}}{c_f E_f + c_m E_m}.$$

Table 4.6 shows the calculated results of σ_{mc} and ε_{mc}.

(2) Matrix cracking saturation stress σ_{sat} and stain ε_{sat}

The matrix cracking saturation stress σ_{sat} was calculated using Eq. (2.31) while the corresponding strain was calculated via $\varepsilon_{sat} = \sigma_{sat} / c_f E_f$. The results of σ_{sat} and ε_{sat} are shown in Table 4.7.

(3) Composite yielding stress σ_y and strain ε_y

The composite yielding stress is given by $\sigma_y = c_f \sigma_{f-yield} + \sigma_S$, where $\sigma_{f-yield}$ is the fiber yielding stress. The corresponding strain is calculated by $\varepsilon_y = \sigma_{f-yield} / E_f$. The result of σ_y is shown in Table 4.8. For W_f/W_m composite, $\varepsilon_y = 4.29 \times 10^{-3}$.

Table 4.6. σ_{mc} and ε_{mc} values of each interface.

Interface	τ_R (MPa)	Γ_i (J/m^2)	σ_A (MPa)	σ_D (MPa)	σ_S (MPa)	σ_{mc} (MPa)	ε_{mc} ($\times 10^{-3}$)
ZrO_x 150	110	2.89	19899	235	78	677.07	1.69
ZrO_x 450	127	3	21382	240	90	720.32	1.8
ZrO_x 950	111	5.86	19990	335	79	594.48	1.49
ZrO_x&W 260	136	2.99	22126	240	97	743.48	1.86
ErO_x 600	174	9.61	25027	430	124	684.24	1.71
ErO_x 1000	64	2.03	15179	197	46	549.68	1.37
ZrO_x/Zr m	104	1.23	19349	154	74	696.22	1.74
ZrO_x/W m	175	3.5	25099	259	124	823.12	2.06
Er/W m	101	3.46	19068	258	72	634.65	1.59
ErO_x/W m	91	2.01	18100	196	65	643.32	1.60
Cu/W m	86	7.66	17595	384	61	414.20	1.03
Cu 170	176	12.34	25171	487	125	608.33	1.52
carbon	74	7.41	16322	377	53	362.01	0.90

Table 4.7. σ_{sat} and ε_{sat} values of each interface.

Interface	τ_R (MPa)	$\bar{l}_s$ (μm)	σ_{sat} (MPa)	ε_{sat} ($\times 10^{-3}$)
ZrO_x 150	110	285.02	627.05	2.61
ZrO_x 450	127	258.98	657.81	2.74
ZrO_x 950	111	283.31	628.94	2.62
ZrO_x&W 260	136	247.43	673.00	2.80
ErO_x 600	174	209.95	730.60	3.04
ErO_x 1000	64	408.96	523.47	2.18
ZrO_x/Zr m	104	295.88	615.43	2.56
ZrO_x/W m	175	209.14	732.01	3.05
Er/W m	101	301.71	609.46	2.54
ErO_x/W m	91	323.43	588.64	2.45
Cu/W m	86	335.85	577.65	2.41
Cu 170	176	208.35	733.40	3.06
carbon	74	371.24	549.43	2.29

Table 4.8. σ_y values of each interface.

Interface	σ_S (MPa)	σ_y (MPa)
ZrO_x 150	78	1098
ZrO_x 450	90	1110
ZrO_x 950	79	1099
ZrO_x&W 260	97	1117
ErO_x 600	124	1144
ErO_x 1000	46	1066
ZrO_x/Zr m	74	1094
ZrO_x/W m	124	1144
Er/W m	72	1092
ErO_x/W m	65	1085
Cu/W m	61	1081
Cu 170	125	1145
carbon	53	1073

(4) Composite ultimate tensile strength σ_u

σ_u is steered by the fiber ultimate stress σ_{f-u} since the fiber is bearing the whole load at the failure stage. The failure strain of the W fiber is determined to be the ultimate strain of the composite. According to the tensile test result σ_{f-u}=2593 MPa while the fiber failure strain is 2.1%. σ_u is obtained by $\sigma_u = c_f \times \sigma_{f-u}$=1555.8 MPa and ε_y=2.1% is determined for the W_f/W_m composites.

The stress-strain curves of the W_f/W_m composites with different interfaces were predicted based on the characteristic stresses and strains calculated above. As the representative examples, stress-strain curves of specimens with the ZrO_x 450 interface, the Cu 170 interface, and the carbon interface, are shown in Fig. 4.45. It should be mentioned that the fiber pull-out stage were drawn schematically; the actual curve form depends on the interface radial stress, friction coefficient, fiber pull-out length, etc.... It can be seen that all of these composites show typical stress-strain curve of a toughened composite, as given in chapter 2, Fig. 2.4 a.

The composite properties are strongly affected by the fiber volume fraction. The stress-strain curves of the W_f/W_m composites with the ZrO_x 450 interface are shown in Fig. 4.46 for different fiber volume fractions. The fracture toughness of the composites increases with the increase of fiber volume. This result is well-understood for two

reasons: firstly, based on the fibers with the same diameter, the increase of the fiber volume leads to a greater interface volume, which indicates an increase in energy absorption due to the crack deflection and frictional fiber sliding; secondly, the W fiber is stronger and tougher than the W matrix, large amount of the W fiber contribute more to the toughness of the composites.

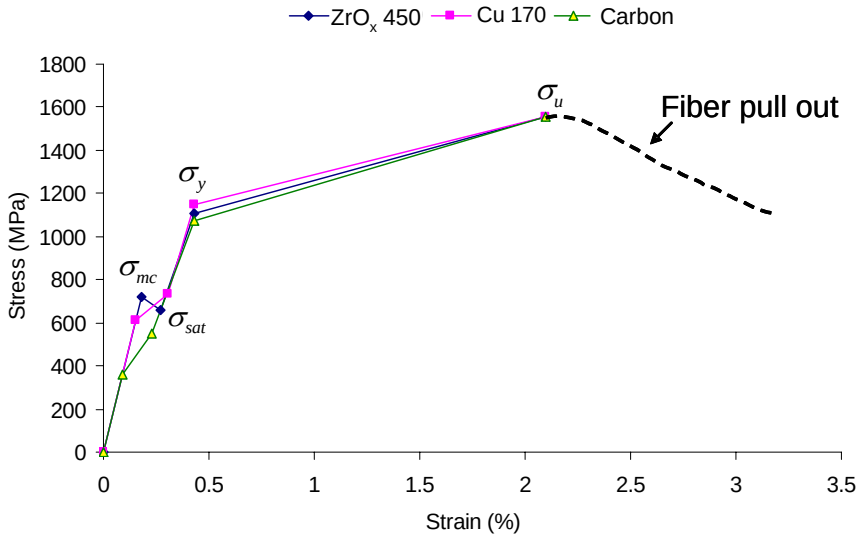

Figure 4.45. Stress-strain curves of W_f/W_m composites with different interfaces

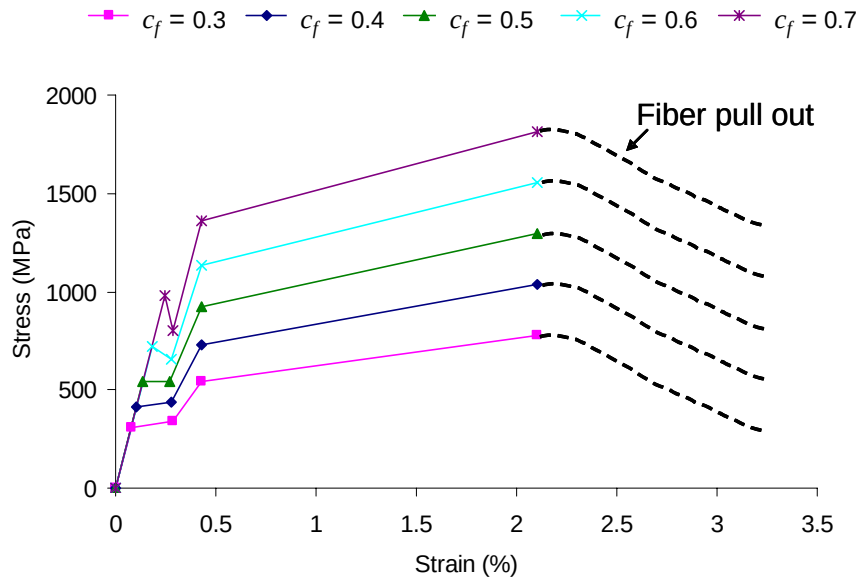

Figure 4.46. Stress-strain curves of W_f/W_m composites with different fiber volume fractions

Chapter 5

Discussion

5.1 Microstructure and chemical composition of the interface

The microstructure and chemical composition analysis results show that all the interfaces were deposited with the desired chemical composition and distribution. The porosity was found in the ZrO_x interfaces and the W particles were present in the ErO_x interfaces. These expected weak interfaces provided the desired environment for the crack deflection. The multilayer interfaces (ZrO_x/Zr m, ZrO_x/W m, ErO_x/W m, Er/W m, and Cu/W m), the ductile interfaces (Cu 170 and Cu 480), and the lubricating interface (C) were deposited with expected structures. Thus, in principle, all of the interfaces of W_f/W_m composite in this work can be fabricated desirable via magnetron sputter deposition.

5.2 Push-out (back) curve

5.2.1 Push-out curve and average energy absorption

No 'partial debonding' stage but a 'load raise' stage was observed in the push-out curves of W_f/W_m composites (see chapter 4.2). The catastrophic shear fracture behavior can be attributed to the thin-thickness effect of W_f/W_m composite specimens. In the first phase, the energy was stored due to the compliance of the indenter as well as the shear strain of the interface. When the load reached a critical value P_{max}, the cracks were initiated (possibly on both free surface edges) and rapidly propagated with the released strain energy, causing the dynamic push-out movement. The 'load raise' was a result mainly due to the interlocking of the debonded interfaces caused by a sudden termination of the fast fiber movement. In addition, the static friction force had to be overcome.

The average energy absorption Δ is a comprehensive parameter indicating the energy consumption ability of an interface during the push-out process. The results of average energy absorption of the 14 interfaces are collected in Table 5.1. The ZrO_x-based interfaces (both oxide and multilayer interfaces) show a similar average energy absorption which is around 20 kJ/m^2. The ErO_x-based interfaces (both oxide and

multilayer interfaces) have an average energy absorption of 17 kJ/m^2. The Cu interfaces (pure Cu and Cu/W m) contain lower average energy absorption ranges from 13-17 kJ/m^2. The carbon interface has the lowest average energy absorption among all interfaces, which is less than 10 kJ/m^2.

It can be concluded that the ZrO_x coating lead to a high energy absorption in the push-out process due to its ceramic characteristic while the carbon coating caused a low energy absorption due to its lubricating property.

Table 5.1. Average energy absorption Δ of each interface.

Interface	Average energy absorption Δ (kJ/m^2)	Interface	Average energy absorption Δ (kJ/m^2)
ZrO_x 150	20.7	ZrO_x/Zr m	18.3
ZrO_x 450	23.0	ZrO_x/W m	21.9
ZrO_x 950	20.5	ErO_x/W m	16.0
ZrO_x&W 260	17.3	Er/W m	16.8
ErO_x 600	15.6	Cu/W m	13.1
ErO_x 1000	16.7	Cu 170	15.8
carbon	9.8	Cu 480	17.2

5.2.2 Push-back curve and average sliding stress

No obvious reseating drop was observed in the push-back curve of the W_f/W_m composites. In reference [146] it was reported that SiC fiber/Borosilicate glass composites have a reseating drop when the fiber moves to its original position, with a load decrease of more than 1 N and a reseating gap of 9.7 μm during the push-back process; for monofilament SiC/Borosilicate composite processed by hot pressing sintering, reference [148] gives a load decease of 1.5 N and a reseating gap of 15 μm. Such reseating phenomena are mainly due to the roughness of the debonded interface. According to the push-back behavior of the W_f/W_m composites, it is believed that the friction caused by the roughness of the debonded interfaces is fairly small. Therefore, the friction during the sliding process is thought to be caused mainly by the Poisson effect as well as by damage on the contacting interfaces in the W_f/W_m composites.

The results of the average sliding stress indicate that specimens with ZrO_x&W 260, ZrO_x/Zr m, and Er/W m interfaces have a similar average sliding stress. This fact indicates that these brittle interfaces have similar interfacial roughness during the sliding stage. The carbon interface specimen has the smallest sliding stress probably due to its

lubricating property. The Cu interfaces (Cu/W m, Cu 480) specimens have a moderate sliding stress due to the plastic flow of the Cu.

5.3 Interfacial parameters

5.3.1 Interfacial shear strength

Figure 5.1 shows the interfacial shear strength τ_d of all the adopted interfaces.

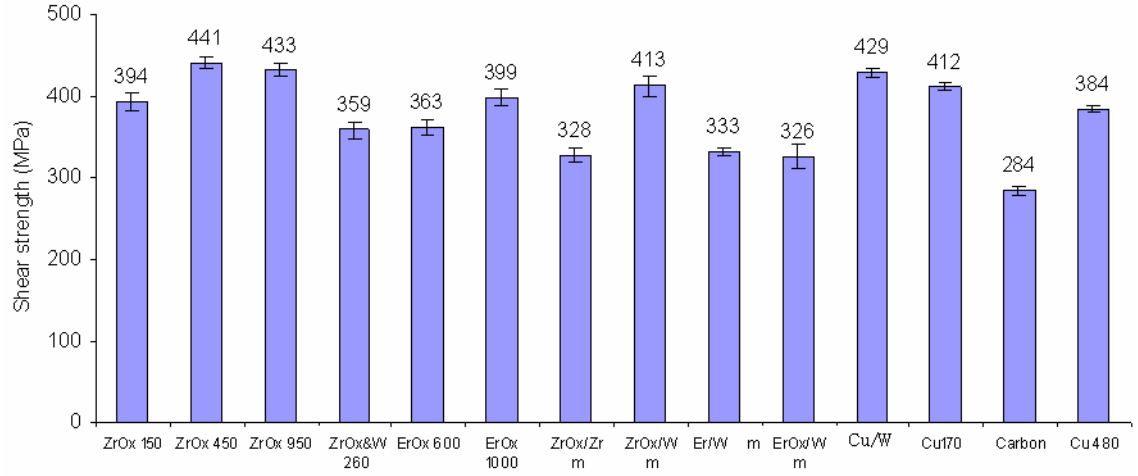

Figure 5.1. Shear strength τ_d of each interface

The average interfacial shear strength of these interfaces lies around 350 MPa. The highest shear strength was observed from the ZrO_x 450 interface, with a value of 441 MPa. The other interfaces have comparable shear strengths with a spread of less than 10%. However, the carbon interface has the lowest shear strength with less than 300 MPa.

These values are fairly moderate compared to the interfaces of other fiber-reinforced composites, for example: carbon-coated-glass-fiber-reinforced cement composites (50 MPa) [128] or SiC-fiber reinforced titanium composites (500 MPa) [144].

5.3.2 Interfacial friction coefficient

Figure 5.2 shows a comparison of the interfacial friction coefficient values for the adopted interfaces. Most of the friction coefficients of the W_f/W_m composite interfaces are lager than 1, being much larger than the typical friction coefficient values (0.25~0.6) [138, 157]. The friction coefficient μ is a dimensionless scalar value which describes the ratio of the drag force of friction between two contacting bodies and the normal force pressing them together. The coefficient of friction is an empirical quantity–it has to be

measured experimentally and cannot be found through calculations alone. Rougher surfaces tend to have higher effective values. Most dry materials in combination have friction coefficient values between 0.3 and 0.6. While in most relevant applications $\mu < 1$, a value above 1 merely implies that the force required to slide an object on a underlying surface is greater than the normal force applied to the object. However, when the contacting surfaces are conjoined, Coulomb friction becomes a very poor approximation (for example, adhesive tape resists sliding even when there is no normal force, or a negative normal force) [158]. In this case, the 'frictional' force may depend strongly on the area of contact as well as the contact interface conditions (interlocking particles and debris). Obviously, for W_f/W_m composite interfaces, the curve fitting results seem to indicate that the friction during the push-out process is of an adhesive type. The roughness and debris generated by the dislocation of the initially matched surfaces may have caused an adhesive type of friction leading to quite large friction coefficients.

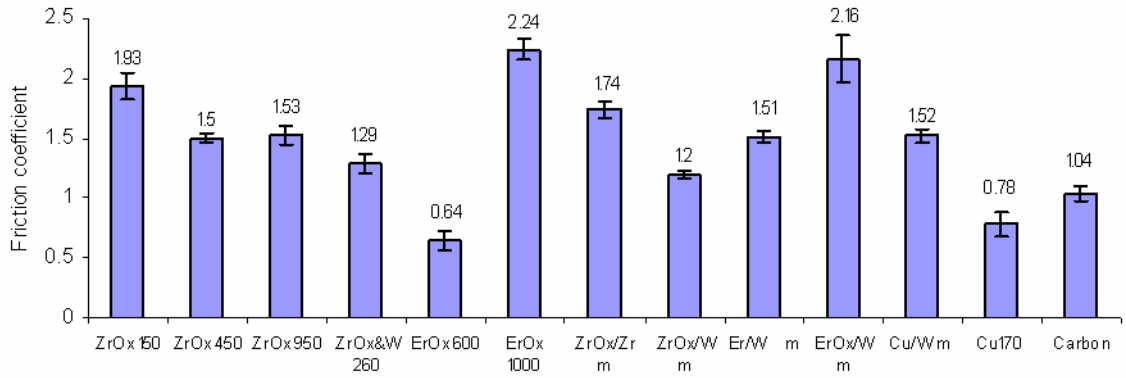

Figure 5.2. Friction coefficient μ of each interface

5.3.3 Interface radial stress

Since the thermal residual stress is neglected, the roughness caused interface radial stress σ_R is the unique radial stress in the W_f/W_m composites. Fig. 5.3 shows the comparison of σ_R for all the interfaces. In Fig. 5.3 the ErO_x 600 (272 MPa) and Cu 170 (225 MPa) interfaces show a rather large σ_R compared to the other interfaces. The ZrO_x&W 260 interface has the third largest one (146 MPa). Apart from these three interfaces, the other interfaces show interface radial stresses lower than 100 MPa.

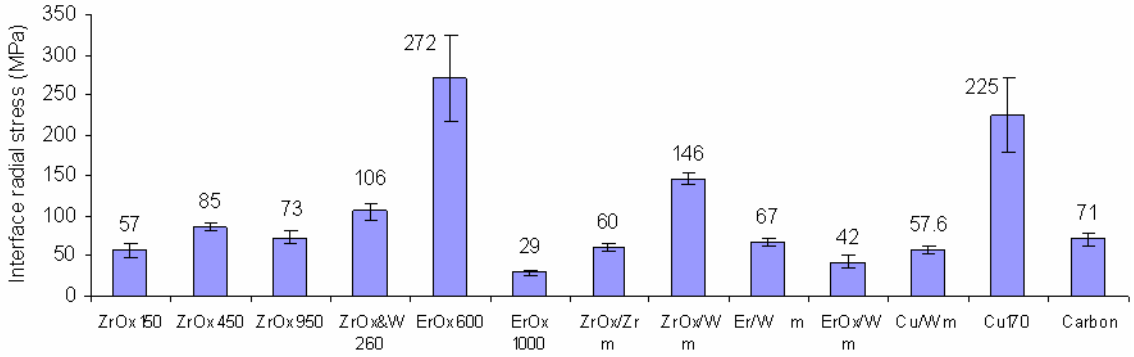

Figure 5.3. Interface radial stress σ_R of each interface

5.3.4 Asperity caused shear stress

The asperity caused shear stress τ_R was computed as the product of the interface radial stress σ_R and the friction coefficient μ. Fig. 5.4 shows the comparison of τ_R for the interfaces. The τ_R results show a value distribution similar to that of the interface radial stress results. The ErO_x 600, Cu 170, and ZrO_x/W 260 interfaces had the greatest τ_R values, 174 MPa, 175.5 MPa, and 175 MPa, respectively. All the other interfaces had a comparable τ_R values ranging from 70 MPa to 130 MPa. Clearly, the gap between the largest and the smallest τ_R is smaller than that of the interface radial stress σ_R. τ_R is the critical interfacial parameter which is used for the mechanical property prediction of the composite with multiple fibers.

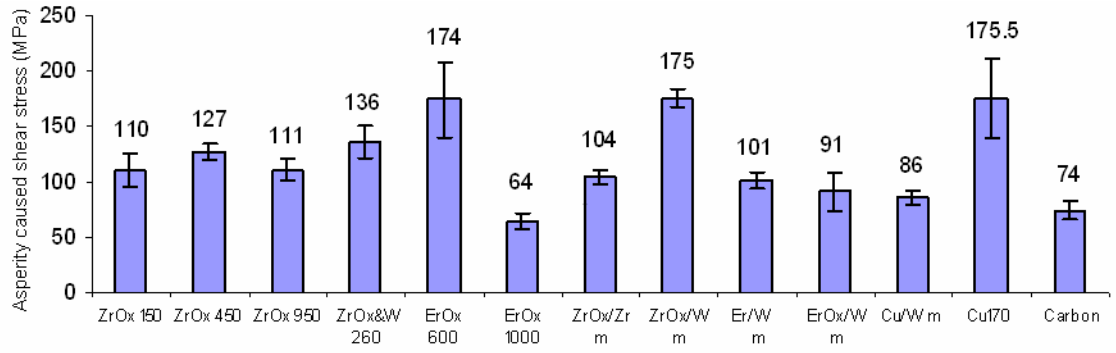

Figure 5.4. Asperity caused shear stress τ_R of each interface

5.3.5 Interfacial fracture energy

Interfacial fracture energy Γ_i is one of the most important interfacial parameters controlling the interfacial debonding and crack deflection in a composite. Fig. 5.5 shows a comparison of the Γ_i for each interface. It can be seen that the Cu interfaces have a very high fracture energy. In particular, the Cu 170 interface has the highest fracture energy, 12.34 J/m^2, while the Cu/W m interface has a fracture energy of 7.66 J/m^2. On the

other hand, the carbon interface also has a relatively high fracture energy: 7.41 J/m^2. The other brittle interfaces (oxide interfaces and the multilayer interfaces), show a very similar fracture energy which is around 3 J/m^2, while the ErO_x 600 interface specimen is an exception: its fracture energy is 9.61 J/m^2. These results are in agreement with the results of the microstructure analysis of interfaces after the push-out test. The microstructure analysis results indicated that, the oxide interfaces and multilayer interfaces had typical brittle debonding during the push-out test, which contained debonding locations mainly lying either between the interface coatings and the fiber or between the matrix and the interface coatings. The brittle interfacial debonding led to the low fracture energy of the interfaces. The Cu interfaces had debonding locations in the Cu coating and strong plastic deformation of the Cu, which led to the high interfacial fracture energy. The layer denomination and fracture of the carbon coating led to the high interfacial fracture energy for the carbon interface.

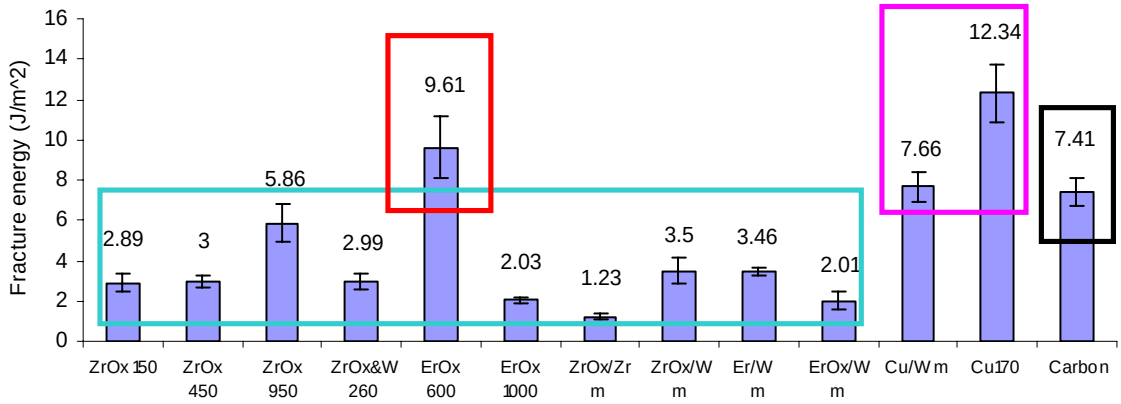

Figure 5.5. Interfacial fracture energy Γ_i obtained by curve fitting of each interface based on Liang-Hutchinson's model

Alternatively, following Clyne [143], Γ_i values were calculated using Eq. (2.20). The results are shown in Fig. 5.6, together with the results from the curve fitting based on Liang-Hutchinson's model: the average value obtained from Clyne's model agrees quite well with the results from Liang-Hutchinson's model, which support the reliability of the results calibrated in this work.

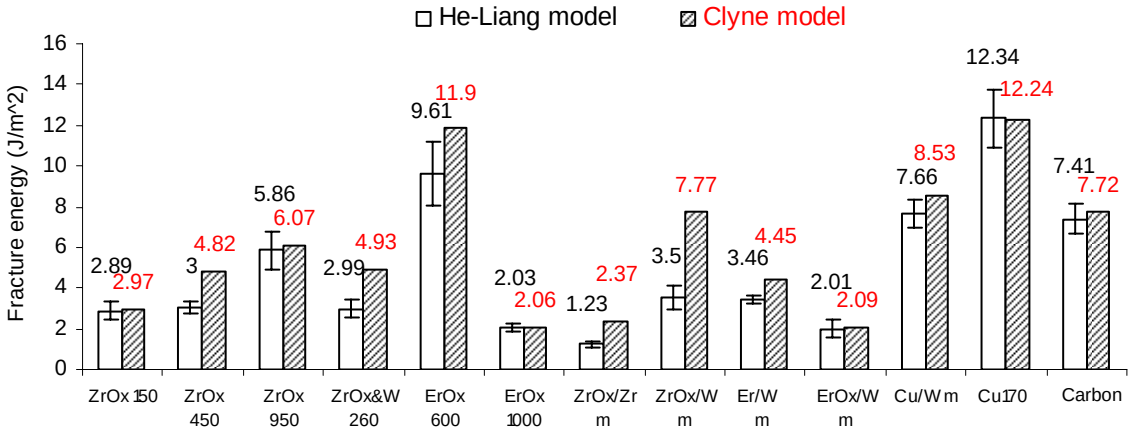

Figure 5.6. Comparison of the interfacial fracture energy Γ_i obtained using different models

5.4 Interfacial debonding realization—criteria verification

As discussed in chapter 2.1.2, the interfacial debonding is the prerequisite for realizing increased fracture toughness for a composite. Based on the interfacial fracture energy data obtained above, one can predict the interfacial debonding behavior of the W_f/W_m composites, regarding the fracture-mechanical criterion. The criterion states that the ratio of the interfacial fracture energy Γ_i to that of the fiber fracture energy Γ_f should be less than 0.25.

In Table 5.2, the fracture energy of each interface is compared with that of the W fiber and W matrix. The listed interfacial fracture energy was obtained by curve fitting using Liang-Hutchinson's model. From the data it can be inferred that the ratio of the interface fracture energy and the W fiber fracture energy lies between 0.003 and 0.034 satisfying the 0.25 criterion. On the other hand, all the interfaces have fracture energy much smaller than that of the W matrix, which satisfies the requirement of avoiding the crack deflecting back to the matrix as explained in chapter 2.1.2.3. These results suggest that all of these interfaces would most likely endow the W_f/W_m composite with pseudo-toughness by allowing the extending matrix cracks to deflect along the interfaces. It should be noted that the fracture energy of these interfaces are smaller than that of the fiber by a factor of 100. Indeed, some FCMC materials showing a high damage tolerance also have a very small interfacial fracture energy.

The fact that the interfacial debonding criterion was satisfied is major evidence for the feasibility of realizing an enhanced-toughness tungsten composite material based on the mechanism of FCMC toughening.

Table 5.2. Fracture energies of the interfaces, the W fiber and the matrix, combined with their ratios.

Interfaces	Fracture energy Γ_i (J/m^2)	Γ_i / Γ_f Γ_f =360 (J/m^2)	Γ_i / Γ_m Γ_m =114 (J/m^2)
ZrO_x 150	2.89	0.008	0.025
ZrO_x 450	3	0.008	0.026
ZrO_x 950	5.86	0.016	0.051
ZrO_x&W 260	2.99	0.008	0.026
ErO_x 600	9.61	0.026	0.084
ErO_x 1000	2.03	0.005	0.017
ZrO_x/Zr m	1.23	0.003	0.01
ZrO_x/W m	3.5	0.01	0.03
Er/W m	3.45	0.01	0.03
ErO_x/W m	2.01	0.005	0.017
Cu/W m	7.66	0.021	0.067
Cu 170	12.34	0.034	0.108
carbon	7.41	0.02	0.065

5.5 Crack deflection demonstration

The crack deflections were directly observed in specimens with an oxide interface (ZrO_x&W 260), a multilayer interface (ZrO_x/Zr m), and a Cu interface (Cu 480). Fiber sliding (pull-in) occurred in the ZrO_x&W 260 interface and ZrO_x/Zr m interface specimens. The Cu 480 interface specimen had a large strain in the fiber center while no fiber sliding was detected. This may be due to the large interfacial fracture energy of Cu 480 interface. The interfacial debonding started in the middle of the Cu 480 interface specimen, and propagated along the interface. Such debonding propagation consumed a great amount of energy due to the high interfacial fracture energy. Therefore, there was not enough energy left for driving the debonding through the entire half of the specimen, and eventually, for fiber dislocation at the end of specimen. Since the fiber had no chance to glide from its original location, the fiber had to be elongated when the tested specimen was bent. Thus, a large strain occurred in the middle of fiber.

The micrographs obtained by the in-situ imaging clearly reveal that the primary matrix crack was deflected along the interface leading to a controlled debonding at the interface while the fiber bridged the opening crack. This cracking feature coincides exactly with the typical toughening mechanism of a FCMC. This result may be direct evidence to support the approach to produce a high-toughness tungsten composite material.

5.6 Mechanical property of W_f/W_m composite with multiple fibers

The stress-strain curves of the W_f/W_m composites with multiple fibers (see Fig. 4.45)—as predicted based on the interfacial parameters obtained in this work—were typical for a toughened composite (see Fig. 2.4 a). The stress-strain curve for different fiber volume concentrations (see Fig. 4.46) indicated that the fracture toughness of the composites increases with the increase of the fiber volume. The stress-strain prediction results indicate the FCMCs toughing mechanism applies to the W_f/W_m composites with the engineered interfaces involved in this work, thus, support the possibility of fabricating a toughened tungsten utilizing the FCMC toughening mechanism.

Chapter 6

Conclusion

For the structural material used in the divertor of thermonuclear fusion reactors, a novel toughening method for tungsten was proposed based on the reinforcement of tungsten fibers (W_f/W_m composite) and engineered interfaces. The underlying toughening mechanism is analogous to that of a fiber-reinforced ceramic matrix composite (FCMC), which relies on energy dissipation by the controlled debonding and friction at the fiber/matrix interfaces. The goal of this thesis was to demonstrate the feasibility of producing a toughened W_f/W_m composite using the FCMC toughening mechanism. In order to optimize the interface between the W fiber and the W matrix to produce the energy dissipation, the main focus of this work lies in the investigation of the interfacial fracture behavior of W_f/W_m composites with various engineered interfaces.

The commercial tungsten wires (fibers) were selected as reinforcement; dense tungsten was chosen as the matrix. The employed interfaces contain: Oxide coatings (ZrO_x 150, ZrO_x 450, ZrO_x 950, ZrO_x&W 260, ErO_x 600, and ErO_x 1000), multilayer coatings (ZrO_x/Zr m, ZrO_x/W m, ErO_x/W m, Er/W m, and Cu/W m), ductile coatings (Cu 170 and Cu 480), and a lubricating coating (C). They were deposited via magnetron sputter deposition, while the tungsten matrix was fabricated via chemical vapor deposition (CVD). Fiber push-out tests were conducted extensively on single-fiber W_f/W_m composites to determine the interfacial parameters by interpreting the experimental data with the theoretical models. Additionally, a miniaturized three-point bending (3PB) test was employed for the direct demonstration of the crack deflection phenomena when an interface was enduring a tensile load. Push-out tests were also conducted on the specimens after heat treatment (800 °C for 10 h) to explore the thermal stability of the interfaces. Microscopic analysis of the interface structures was carried out before and after the push-out tests by means of scanning electron microscope (SEM) equipped with focused ion beam (FIB) engraving the embedded interface domains. Energy dispersive x-ray spectroscopy (EDXS) and secondary ion mass spectrometry (SIMS) were used for clarifying the chemical compositions and distributions of the interface coatings.

6 Conclusion

In the following, the main results of this work are discussed.

Composite synthesis

Commercial tungsten wires with diameters of 150 μm, >2.5 MPa tensile strength, and >2.1% failure strain were used as the fibers. The tungsten matrix, fabricated via CVD, had a density of 19.3±0.2 g/m^3. Various interface coatings were deposited via magnetron sputter deposition. The ZrO_x interfaces (ZrO_x 150, ZrO_x 450, ZrO_x 950, and ZrO_x&W 260) were successfully deposited with few pores present in the coatings. The ErO_x interfaces (ErO_x 600 and ErO_x 1000) were deposited with the expected thicknesses with a small amount of W particles. The multilayer interfaces (ZrO_x/Zr m, ZrO_x/W m, ErO_x/W m, Er/W m, and Cu/W m), the ductile interfaces (Cu 170 and Cu 480), and the lubricating interface (C) were deposited with expected distributions and fewer defects. Thus, in principle, the single-fiber W_f/W_m composites can be fabricated well with the methods used in this work.

Push-out (back) curves

The oxide interfaces and the multilayer interfaces had push-out curves with similar debonding characteristics, where no obvious progressive debonding was detected. The Cu/W m interface had similar push-out curve as the oxide ones, since the deformation of the Cu layer in the Cu/W m interface was strongly limited by the thickness restrictions of the Cu layers (100 nm). The Cu 480 and the Cu 170 interfaces had push-out curves indicating strong deformation of the Cu 480 layer and moderate deformation of the Cu 170 layer. The C interface showed similar debonding as with the oxide but had relatively low complete debonding and friction loads, indicating a low load bearing ability of the C coating deposited via magnetron sputtering. The ZrO_x coating led to a high energy absorption in push-out process due to its ceramic characteristic while the carbon coating caused a low energy absorption due to its lubricating property.

The push-back curves of the W_f/W_m composites showed no obvious reseating drop as described in literature for some other FCMCs, which indicates that the friction during the sliding process in the W_f/W_m composites was caused mainly by the Poisson effect as well as the damage on the contacting interfaces. The average sliding stresses of the debonded interfaces estimated according to the push-back curves showed that the brittle interfaces (ZrO_x&W 260, ZrO_x/Zr m, and Er/W m) had a similar average sliding stress being larger than 100 MPa; the C interface had the lowest average sliding stress of 68 MPa; and the Cu interfaces (Cu 480 and Cu/W m) had a moderate average sliding stress around of 90 MPa.

Interfacial parameters analysis

The interfacial parameters were obtained by interpreting the push-out data with the theoretical models through curve fitting.

The results for the average interfacial shear strength τ_d indicated that most of these interfaces had a shear strength around 350 MPa. The highest shear strength was observed from the ZrO_x 450 interface, with a value of 441 MPa, while the other interfaces had comparable shear strengths with a spread of less than 10%. However, the carbon interface had the lowest shear strength with less than 300 MPa. These values are fairly moderate compared to the interfaces of other fiber-reinforced composites.

The interfacial friction coefficient μ of different interfaces show that most of the friction coefficients of the interfaces of the W_f/W_m composites were extremely high (larger than 1), which may indicate that the friction during the push-out process was of an adhesive type caused by undulation and debris generated by the dislocation of the initially matched surfaces.

The results for the interface radial stress σ_R show that the ErO_x 600 and Cu 170 interfaces had the largest two interface radial stresses, 272 MPa and 225 MPa, respectively. The ZrO_x&W 260 interface had the third largest one (146 MPa). Apart from these three interfaces, the other interfaces exhibited radial stresses lower than 100 MPa.

The asperity caused shear stress τ_R results show a value distribution similar to that of the interface radial stress results: The ErO_x 600, Cu 170, and ZrO_x/W 260 interfaces had the largest asperity caused shear stress, 174 MPa, 175.5 MPa, and 175 MPa, respectively. All of the other interfaces had comparable asperity caused shear stress ranging from 70 MPa to 130 MPa. Clearly, the gap between the largest and the smallest asperity caused shear stress is less than that of the interface radial stress.

The results for the fracture energy Γ_i indicate that the Cu based-interfaces had very high fracture energies, the Cu 170 interface with 12.34 J/m^2, and the Cu/W m interface with 7.66 J/m^2; the carbon interface also had a relatively high fracture energy: 7.41 J/m^2; the other brittle interfaces (the oxide and multilayer interfaces) showed very similar fracture energies around 3 J/m^2.

Interfacial debonding location identification

Interfacial debonding locations identified via SEM equipped with FIB indicated that the brittle interfaces (the oxide interfaces and the multilayer interfaces) contained debonding locations mainly lying either between the interface coatings and the fiber or between the matrix and the interface coatings, while the debonding locations in the Cu interfaces and the carbon interface were present in the interface coatings. Those results are in accordance with the fracture energy calibration results.

Crack deflection verification

The estimated ratios of the interface fracture energies and the W fiber fracture energy lie between 0.003 and 0.034, which satisfy the interfacial debonding criterion. Additionally, the interface fracture energies were much smaller than that of the W matrix thus satisfying the criterion of avoiding the crack deflecting back to the matrix. Those results suggest that all of the considered interfaces would most likely endow the W_f/W_m composite with pseudo-toughness by allowing the extending cracks to deflect along the interfaces.

Direct demonstration of interfacial crack deflection

Interfacial crack deflections were observed directly in the ZrO_x&W 260 interface, the ZrO_x/Zr m interface, and the Cu 480 interface specimens via a miniaturized 3PB test. Significant fiber sliding (fiber pull-in) was found in the specimens with ZrO_x&W 260 and ZrO_x/Zr m interfaces. A large strain was found in the middle region of the fiber in the Cu 480 interface specimen, however, no fiber pull-in was observed.

This cracking feature coincided exactly with the typical toughened FCMC, which can be used as direct evidence to support our approach in the realization of a high-toughness tungsten composite material.

Interfaces thermal stabilities

The interfacial parameters obtained from the specimens after heat treatment (800 °C for 10 h) show that the oxide interfaces and multilayer interfaces had good thermal stability in terms of the interfacial fracture behavior, while the interfacial fracture behavior of the Cu/W m and the carbon interfaces were strongly affected by the heat treatment due to grain growth and phase change, respectively.

Mechanical property prediction of the W_f/W_m composites with multiple fibers

The stress-strain curves of the W_f/W_m composites with multiple fibers—as predicted based on the interfacial parameters obtained in this work—were typical for a toughened composite. This indicates the FCMCs toughing mechanism applies to the W_f/W_m composites with the engineered interfaces involved in this work, thus, supports the possibility of fabricating a toughened tungsten utilizing the FCMCs toughening mechanism.

Concluding remarks

Enhancing the properties of tungsten materials for their practical use in the divertor of thermonuclear fusion reactors is very challenging. There is an urgent need to explore new toughening mechanisms which function effectively even under neutron irradiation and in the embrittling temperature regime.

In this work, a novel toughening method for tungsten, which retains toughness even under embrittlement conditions, was proposed and developed based on the reinforcement of tungsten fibers (W_f/W_m composite) and engineered interfaces. This work opened a new pathway to improve the toughness of tungsten as a structural material.

Technologies such as the magnetron sputtering, and CVD are well-developed and suitable for the synthesis of W_f/W_m composites. The satisfying development, characterization, implementation, and mechanical testing of the single-fiber W_f/W_m composites demonstrate that the manufacturing of a toughened tungsten structural material by utilizing the FCMCs toughening mechanism for the divertor of thermonuclear fusion reactors is feasible.

List of publications and conference contributions

Publications

1. J. Du, T. Höschen , M. Rasinski , S. Wurster , W. Grosinger , J.-H. You. Feasibility study of a tungsten wire-reinforced tungsten matrix composite with ZrO_x interfacial coatings. Composites Science and Technology , 70: 1482–1489, 2010.
2. J. Du, T. Höschen, M. Rasinski, J.-H. You. Interfacial fracture behavior of tungsten wire/tungsten matrix composites with copper-coated interfaces. Materials Science and Engineering A, 527: 1623–1629, 2010.
3. J. Du, T. Höschen, M. Rasinski, J-H. You. Fracture Behavior of Engineered Fiber/Matrix Interfaces in Fibrous Tungsten-Tungsten Composites. Journal of nuclear materials (14th International Conference on Fusion Reactor Materials, Sapporo, Japan).

Oral conference presentation

J. Du, T. Höschen, M. Rasinski, J-H. You, A. Brendel, F. Koch, G. Matern, Fracture Behavior of ZrO_x-based interfaces in Fibrous Tungsten/Tungsten Composites. European Congress on Advanced Materials and Processes, 7-10 September 2009, Glasgow, United Kingdom.

Poster presentation

J. Du, T. Höschen, M. Rasinski, J-H. You. Fracture Behavior of Engineered Fiber/Matrix Interfaces in Fibrous Tungsten-Tungsten Composites. 14th International Conference on Fusion Reactor Materials, 7-12, September, 2009, Sapporo, Japan.

References

[1] J. D. Lawson. Some criteria for a power producing thermonuclear reactor. Proceedings of the Physical Society Section B, 70: 6-10, 1957.

[2] M. A. Pick and Jet Team. The technological achievements and experience at JET. Fusion Engineering and Design, 46: 291–298, 1999.

[3] O. Gruber. ASDEX Upgrade enhancements in view of ITER application. Fusion Engineering and Design, 84: 170–177, 2009.

[4] The TEXTOR Team and the ALT-I Group. Plasma-wall Interaction and Plasma Performance in TEXTOR - a review. Journal of Nuclear Materials, 145-147: 3-14, 1987.

[5] J. Winter, F. Waelbroeck, P. Wienhold, H. G. Esser, L. Koenen, M. Braun, B. Emmoth and H. E. Sätherblom. Wall conditioning of TEXTOR. Journal of Nuclear Materials 128 & 129: 841-850, 1984.

[6] S. Wu and the EAST Team. An overview of the EAST project. Fusion Engineering and Design, 82: 463–471, 2007.

[7] Y. Shimomura, K. Shimizu, T. Hirayama, M. Azumi and H. Ninomiya. JT-60 Program. Journal of Nuclear Materials, 128 & 129: 19-25, 1984.

[8] ITER technical basis. Technical report, International Atomic Energy Agency, 2002.

[9] U. Schumacher. Status and problems of fusion reactor development. Naturwissenschaften, 88 (3): 102-112, 2001.

[10] M. Merola, W. Dänner, J. Palmer, G. Vielder and C. H. Wu. European contribution to the development of the ITER divertor. Fusion energy and design, 66-68: 211-217, 2003.

[11] K. Ehrlich. Materials research towards a fusion reactor. Fusion Engineering and design, 56-7: 71-82, 2001.

[12] S. J. Zinkle and N. M. Ghoniem. Operating temperature windows for fusion reactor structure materials. Fusion Engineering and design, 51-52: 55-71, 2000.

[13] A. S. Kukushkin, H. D. Pacher, G. Federici, G. Janeschitz, A. Loarte, and G. W. Pacher. Divertor issues on ITER and extrapolation to reactors. Fusion Engineering and design, 65(3): 355-366, 2003.

[14] R. Lässer, N. Baluc, J. L. Boutard, E. Diegele, S. Dudarev, M. Gasparotto, A. Möslang, R. Pippan, B. Riccardi and B. van der Schaaf. Structural materials for DEMO: The EU development, strategy, testing and modeling. Fusion Engineering and Design, 82: 511–520, 2007.

[15] R. Andreani, E. Diegele, R. Laesser and B van der Schaaf. The European integrated materials and technology program in fusion. Journal of Nuclear Materials, 329–333:

20–30, 2004.

[16] D. Maisonnier, I. Cook, S. Pierre, B. Lorenzo, B. Edgar, B. Karin, D. P. Luigi, F. Robin, G. Luciano, H. Stephan, N. Claudio, N. Prachai, P. Aldo, T. Neill and W. David, The European power plant conceptual study. Fusion Engineering and Design, 75–79: 1173–1179, 2005.

[17] D. Maisonnier, I. Cook, S. Pierre, B. Lorenzo, D. P. Luigi, G. Luciano, N. Prachai, P. Aldo and PPCS Team. DEMO and fusion power plant conceptual studies in Europe. Fusion Engineering and Design, 81: 1123–1130, 2006.

[18] P. Norajitra, S. I. Abdel-Khalik, L. M. Giancarli, T. Ihli, G. Janeschitz, S. Malang, I. V. Mazul and P. Sardain. Divertor conceptual designs for a fusion power plant. Fusion Engineering and Design, 83: 893–902, 2008.

[19] I Ovchinnikov, R. Giniyatulin, T. Ihli, G. Janeschitz, A. Komarov, R. Kruessmann, V. Kuznetsov, S. Mikhailov, P. Norajitra and V. Smirnov. Experimental study of DEMO helium cooled divertor target mock-ups to estimate their thermal and pumping efficiencies. Fusion Engineering and Design, 73: 181–186, 2005.

[20] V. Widak, P. Norajitra, L. V. Boccaccini and G. Janeschitz. Assessment of the He-cooled Test Divertor Module for ITER. Fusion Engineering and Design, 83: 1131–1136, 2008.

[21] T. Ihli, A. R. Raffray, S. I. Abdel-Khalik, S. Shin and the ARIES-CS Team. Design and performance study of the helium-cooled T-tube divertor concept. Fusion Engineering and Design, 82: 249–264, 2007.

[22] P. Norajitra, R. Giniyatulin, T. Ihli, G. Janeschitz, W. Krauss, R. Kruessmann, V. Kuznetsov, I. Mazul, V. Widak, I. Ovchinnikov, R. Ruprecht and B. Zeep. He-cooled divertor development for DEMO. Fusion Engineering and Design, 82: 2740–2744, 2007.

[23] P. Norajitra, R. Giniyatulin, T. Hirai, W. Krauss, V. Kuznetsov, I. Mazul, I. Ovchinnikov, J. Reiser, G. Ritz, H. J. Ritzhaupt-Kleissl and V. Widak. Current status of He-cooled divertor development for DEMO. Fusion Engineering and Design. 84: 1429–1433, 2009.

[24] A. R. Raffray, S. Malang and X. Wang. Optimizing the overall configuration of a He-cooled W-alloy divertor for a power plant. Fusion Engineering and Design, 84: 1553-1557, 2009.

[25] A. R. Raffray, R Nygren, D. G. Whyte, S. Abdel-Khalik, R. Doerner, F. Escourbiac, T. Evans, R. J. Goldston, D. T. Hoelzer, S. Konishi, P. Lorenzetto, M. Merolak, R. Neu, P. Norajitra, R. A. Pitts, M. Rieth, M. Roedig, T. Rognlien, S. Suzuki, M. S. Tillack and C. Wong. High heat flux components-Readiness to proceed from near term fusion systems to power plants. Fusion Engineering and Design, 85: 93–108, 2010.

[26] Y Ishijima, H Kurishita, K Yubuta, H Arakawa, M Hasegawa, Y Hiraoka, T. Takida and K. Takebe. Current status of ductile tungsten alloy development by mechanical

alloying. J Nucl Mater. 329-333: 775-779, 2004.

[27] M Rieth, B Dafferner. Limitations of W and W–1%La2O3 for use as structural materials. J Nucl Mater. 342: 20-25, 2005.

[28] A A F Tavassoli. Present limits and improvements of structural materials for fusion reactors – a review. J Nucl Mater 302: 73-88, 2002.

[29] M Faleschini, H Kreuzer, D Kiener and R Pippan. Fracture toughness investigations of tungsten alloys and SPD tungsten alloys. J Nucl Mater, 367–370: 800-805, 2007.

[30] A. G Evans. Design and life prediction issues for high-temperature engineering ceramics and their composites. Acta Mater, 45(1): 23-40,1997.

[31] T. Mah, M. G. Mendiratta, A. P. Katz, R. Ruh and K. S. Mazdiyasni. Room-tmeperature mechanical behavior of fiber-reinforced cermaic-matrix composites. Journal of American Ceramic Society, 68(1): C-27-C-30, 1985.

[32] D. B. Marshall, B. N. Cox and A. G. Evans. The mechanics of matrix cracking in brittle-matrix fiber composites. Acta metallurgy, 33(11): 2013-2021, 1985.

[33] D. B. Marshall and A. G. Evans, Failure mechanisms in. ceramic-fiber/ceramic-matri x composites. Journal of American Ceramic Society, 68(5): 225-231, 1985.

[34] A. G. Evans and R. M. McMeeking. On the toughening of ceramics by strong reinforcements. Acta metallurgy, 34(12): 2435-2441, 1986.

[35] D. B. Marshall and B. N. Cox. Tensile fracture of brittle matrix composites: influence of fiber strength. Acta metallurgy, 35(11): 2607-2619, 1987.

[36] M. D. Thouless and A. G. Evans. Effects of pull-out on the mechanical properties of ceramic-matrix composites. Acta metallurgy, 36(3): 517-522, 1988.

[37] A. J. Eckel and R. C. Bradt. Strength distribution of reinforcing fibers in a Nicalon fiber/chemically vapor infiltrated silicon carbide matrix composite. Journal of American Ceramic Society, 72(3): 455-458, 1989.

[38] M. D. Thouless, O. Sbaizero, L. S. Sigl and A. G. Evans. Effect of interface mechanical properties on pullout in a SiC-fiber-reinforced Lithium Aluminum Silicate glass-ceramic. Journal of American Ceramic Society, 72(4): 525-532, 1989.

[39] R J Kerans, R S Hay, N J Pagano and T A Parthasarathy. The role of the fiber-matrix interface in ceramic composites. Ceram Bull 68(2): 429-442, 1989.

[40] H. C. Cao, E. Bischoff, O. Sbaizero, M. Rühle, A. G. Evans, D. B. Marshall and J. J. Brennan. Effect of interfaces on the properties of fiber-reinforced ceramics. Journal of American Ceramic Society, 73(6): 1691-1699,1990.

[41] A. G. Evans. Perspective on the development of high-toughness ceramics. J Am Ceram Soc 73(20: 187-206, 1990.

[42] H. Cao and M. D. Thouless. Tensile test of ceramic-matrix composites: theory and experiment. Journal of American Ceramic Society, 73(7): 2091-2094, 1990.

[43] W. A. Curtin. Theory of mechanical properties of ceramic-matrix Ccomposites. Journal of American Ceramic Society, 74(11): 2837-2845, 1991.

[44] F. E. Heredia, S. M. Spearing, A. G. Evans, P. Mosher and W. A. Curtin. Mechanical properties of continuous-fiber-reinforced carbon matrix composites and relationships to constituent properties. Journal of American Ceramic Society, 75(11): 3017-3025, 1992.

[45] A. G. Evans, J. M. Domergue and E. Vagaggini. Methodology for relating the tensile constitutive behavior of ceramic-matrix composites to constituent properties. Journal of American Ceramic Society, 77(6): 1425-1435, 1994.

[46] Yutaka and Kagawa. Effect of thermally induced stress on fracture toughness of SiC fiber-glass matrix composites. Materials transactions, JIM, 35(5): 363-369, 1994.

[47] M. Hoffman, B. Fiedler, T. Emmel, H. Prielipp, N. Claussen, D. Gross and J. Rödel. Fracture behaviour in metal fiber reinforced ceramics. Acta materials, 45(9): 3609-3623, 1997.

[48] T. Tanimoto. Continuous-fibre CMC fabrication using pre-impregnated sheets. Composites: Part A, 30: 583–586, 1999.

[49] M Kuntz and G Grathwohl. Advanced evaluation of push-in data for the assessment of fiber reinforced ceramic matrix composites. Adv Eng Mater, 3(6): 371-379, 2001.

[50] C. Kaya, X. Gu, I. Al-Dawery and E. G. Butler. Microstructrual development of woven mullite fiber-reinforced mullite ceramic matrix composites by infiltration processing. Science Technology of Advanced Materials, 3:35-44, 2002.

[51] J. Mentz, M. Mueller, H. P. Buchkremer and D. Stöver. Carbon-fibre-reinforced carbon composite filled with SiC particles forming a porous matrix. Materials Science and Engineering A 425: 64–69, 2006.

[52] S. Mall and K. J. LaRochelle. Fatigue and stress-rupture behaviors of SiC/SiC composite under humid environment at elevated temperature. Composites Science and Technology, 66: 2925–2934, 2006.

[53] N. P. Bansal. Mechanical properties of Hi-Nicalon fiber-reinforced celsian composites after high-temperature exposures in air. Journal of the European Ceramic Society, 29: 525–535, 2009.

[54] B. Budiansky, A. G. Evans and J. W. Hutchinson. Fiber-matrix debonding effects on cracking in aligned fiber ceramic composite. International Journal of solids structure, 452: 315-328, 1995.

[55] G. W. Milton. The theory of composites. Cambridge University Press, 2002.

[56] C. R. Popescu. Processing and characterization of SiC-fiber reinforced Cu-matrix composites. PhD thesis, Max-Planck-Institut für Plasmaphysik, 2004.

[57] D. Hull and T.W. Clyne. An Introduction to Composite Material, Second Edition. Cambridge Solid State Science Series Cambridge University Press, 1996.

[58] K. K. Chawla. Composite Materials: Science and Engineering, second edition. Springer-Verlag New York, 1998.

[59] B. Lawn. Fracture of Brittle Solids-Second Edition. Cambridge Solid State Science Series, Cambridge University Press, 1993.

[60] M. Y. He and Hutchinson. Crack deflection at an interface between dissimilar elastic materials. International Journal of Solids Structure, 25(9):1053-1067, 1989.

[61] J. Mencik. Mechanics of components with treated or coated surfaces. Kluwer Academic Publishers, 1995.

[62] W. Krenkel. Faserverbunkeramiken- Werkstoffe für den strukturellen Hoch temperatureinsatz, Vortrag, Max-Planck-Institut Garching, 2006.

[63] J. K. Kim and Y. W. Mai. Engineered interfaces in fiber reinforced composites, First edition. Elsevier Science Ltd, 1998.

[64] Z. Ji, J. A. Haynes, M. K. Ferber, and J. M. Rigsbee. Metastable tetragonal zirconia formation and transformation in reactively sputter deposited zirconia coatings. Surface and Coatings Technology, 135:109-117, 2001.

[65] B. Liang and C. Ding. Thermal shock resistances of nanostructured and conventional zirconia coatings deposited by atmospheric plasma spraying. Surface & Coatings Technology, 197: 185– 192, 2005.

[66] T. Chikada , A. Suzuki, Z. Yao, A. Sawada, T. Terai and T. Muroga. Basic study on self-healing of Er_2O_3 coating for vanadium–lithium blanket system. Fusion Engineering and Design, 82: 2572–2577, 2007.

[67] M. R. Gilbert and R. A. Forrest, Handbook of activation data calculated using EASY-2003. EURATOM/UKAEA Fusion Association, United Kingdom, 2004

[68] S. V. Aagender and P. R. Rao. Phase diagrams of binary tungsten alloys. Indian institute of metals, Calcutta, 1991.

[69] J. Mentz, M. Müller, H. P. Buchkremer, and D. Stöver, Carbon fibre-reinforced carbon composite filled with SiC particles forming a porous matrix. Material Science and engineering, A425: 64-69, 2006.

[70] W. Zhang, T. Hinoki, Y. Katoh, A. Kohyama, T. Noda, T. Muroga and J. Yu. Crack initiation and growth characteriatic in SiC/SiC under indentation test. Journal of Nuclear materials, 258-263: 1577-1581, 1998.

[71] S. Utsumi, M. Kanamaru, H. Honda, H. Kanoh, H. Tanaka, T. Ohkubo, H. Sakai, M. Abe and K. Kaneko. RBM band shift-evidenced dispersion mechanism of single-wall carbon nanotube bundles with NaDDBS. Journal of Colloid and Interface Science, 308: 276-284, 2007.

[72] J. E. Mahan. Physical vapor deposition of thin films. A Wiley-Interscience publication, 2000.

[73] M. Ohring. The material science of thin films, Academic press, 1991.

[74] P. J. Kelly and R. D. Arnell. Magnetron sputtering: a review of recent developments and applications. Vacuum 56: 159-172, 2000.

[75] I. Safi. Recent aspects concerning DC reactive magnetron sputtering of thin films: a review. Surface and Coatings Technology 127: 203-219, 2000.

[76] K. L. Choy. Chemical vapour deposition of coatings. Progress in Materials Science, 48: 57–170, 2003.

[77] N. Chandra and C. R. Ananth. Analysis of interfacial behavior in MMCs and IMCs by use of thin-slice push-out tests. Composites Science and Technology, 54: 87-100, 1995.

[78] R. J. Kerans and T. A. Parthasarathy. Theoretical analysis of the fiber pull-out and push-out tests. Journal of America Ceramic Society, 74(7): 1585-1596, 1991.

[79] T. A. Parthasarathy. P. D. Jero and R. J. Kerans, Extraction of interface properties from a fiber push-out test. Scripta Metallurgic Materials, Vol.25: 2457-2462, 1991.

[80] C. Liang and J. W. Hutchinson. Mechanics of the fiber pushout test. Mechanics of materials, 14: 207-221, 1993.

[81] L. B. Greszczuk. Theoretical studies of the mechanics of fiber-matrix interface in composites. ASTM special technical publication, 452: 42-58, 1969.

[82] P. Lawrence. Some theoretical considerations of fiber pullout problem, theory and experiment. Journal of Material Science, 7: 1-6, 1970.

[83] R. J. Gray. Analysis of the effect of embedded fiber length on fiber debonding and pull-out from an elastic matrix-Part 1 Review of the theories. Journal of Materials Science, 19: 861-870, 1984.

[84] D. K. Shetty. Shear-lag analysis of fiber push-out (indentation) tests for estimating interfacial friction stress in ceramic-matrix composites. Journal of America Ceramic Society, 71(2): C-107-C-109, 1988.

[85] David, B. Marshall and W. C. Oliver. Measurement of interfacial mechanical properties in fiber-reinforced ceramic composite. Journal of American Ceramic Society, 70(8): 542-548, 1987.

[86] C. H. Hsueh. Elastic load transfer from partially embedded axially loaded fiber to matrix. Journal of materials science letters, 7: 497-500, 1988.

[87] C. H. Hsueh. Analytical evaluation of interfacial shear strength for fiber-reinforced ceramic composites. Journal of America Ceramic Society, 71(6): 490-493, 1988.

[88] C. H. Hsueh, Mattison, K. Ferber and P. F. Becher. Stress-displacement relation of fiber for fiber-reinforced ceramic composites during (indentation) loading and unloading. Journal of materials research, 4(6): 1529-1537, 1989.

[89] C. H. Hsueh. Some consideration of evaluation of interfacial frictional stress from the indentation technique for fiber-reinforced ceramic composite. Journal of materials science letters, 8: 739-742, 1989.

[90] C. H. Hsueh. Analytical analyses of stress transfer in fiber-reinforced composites with bonded and debonded fiber ends. Journal of materials science, 24: 4475-4482, 1989.

[91] C. H. Hsueh. Effects of interfacial bonding on sliding phenomena during compressive loading of an embedded fiber. Journal of materials science, 25: 4080-4086, 1990.

[92] C H. Hsueh. Interfacial debonding and fiber pull-out stresses of fiber-reinforced composites. Mater Sci Eng, A123: 1-11, 1990.

[93] C. H. Hsueh. Interfacial debonding and fiber pull-out stresses of fiber-reinforced composites, II: Non-constant interfacial bond strength. Materials science and engineering, A125: 67-73, 1990.

[94] C. H. Hsueh. Interfacial debonding and fiber pull-out stresses of fiber-reinforced composites, III: With residual radial and axial stresses. Materials science and engineering, A145:135-142, 1991.

[95] C. H. Hsueh. Interfacial debonding and fiber pull-out stresses of fiber-reinforced composites, IV: Sliding due to residual stresses. Materials science and engineering, A145: 143-150, 1991.

[96] C. H. Hsueh. Interfacial debonding and fiber pull-out stresses of fiber-reinforced composites, VII: improved analyses for bonded interfaces. Materials science and engineering, A154: 125-132, 1992.

[97] C. H. Hsueh. Interfacial debonding and fiber pull-out stresses of fiber-reinforced composites, VIII: The energy-based debonding criterion. Materials science and engineering, A159: 65-72, 1992.

[98] C. H. Hsueh. Interfacial debonding and fiber pull-out stresses of fiber-reinforced composites, IX: A simple treatment of Posson's effect for frictional interfaces. Materials science and engineering letters, A161: L1-L6, 1993.

[99] C. H. Hsueh and M. K. Ferber. Evaluation of residual axial stresses and interfacial friction in Nicalon fiber-reinforced macro-defect-free cement composites. Journal of materials science, 28: 2551-2556, 1993.

[100] C. H. Hsueh. Pull-out a ductile fiber from a brittle matrix, part I shear lag model. Journal of materials science, 29: 4793-4801, 1994.

[101] C. H. Hsueh. Pull-out a ductile fiber from a brittle matrix, part II A simplified model. Journal of materials science, 29: 5135-5140, 1994.

[102] C. H. Hsueh. Consideration of radial dependences of axial stresses in the shear-lag mpdel for fiber pull-out. Journal of materials science, 29: 1801-1806, 1994.

[103] C. H. Hsueh. Crack-wake interfacial debonding criteria for fiber-reinforced ceramic composites. Acta materials , 44(6): 2211-2216, 1996.

[104] C. H. Hsueh. Effects of interfacial roughness on fiber push-out. Journal of materials science letters, 16: 354-357, 1997.

[105] C. H. Hsueh and P. F. Becher. Interfacial shear debonding problems in fiber-reinforced ceramic composites. Acta materials, 46(9): 3237-3245, 1998.

[106] D. B. Marshall. Analysis of fiber debonding and sliding experiments in brittle matrix composites. Acta metallurgy, 40(3): 427-441, 1992.

[107] P. G. Charalambides and A. G. Evans. Debonding properties of residually stressed Brittle-matrix composites. Journal of American Ceramic Society, 72(5): 746-753, 1989.

[108] P. G. Charalambides. Fiber debonding in residually stressed brittle matrix composite. Journal of American Ceramic Society, 73(6): 1674-1680, 1990.

[109] Y. C. Gao, Y. W. Mai and Brian Cotterell. Fracture of fiber-reinforced materials. Journal of Applied Mathematics and Physics (ZAMP), 39: 550-572, 1988.

[110] H. Y. Liu, L. M. Zhou and Y. W. Mai. Effect of interface roughness on fiber push-out stress. Journal of American Ceramic Society, 78(3): 560-566, 1995.

[111] J. D. Bright, D. K. Shetty, C. W. Griffin and S. Y. Limaye. Interfacial bonding and friction in silicon carbide(filament)-reinforced ceramic- and glass-matrix composites, Journal of America Ceramic Society, 72(10): 1891-1898, 1989.

[112] T. A. Parthasarathy, P. D. Jero and R.J. Kerans. Extraction of interface properties from a fiber push-out test. Scripta Metallurgic Materials, 25: 2457-2462, 1991.

[113] C. H. Hsueh, J. D. Bright and D. K. Shetty. Interfacial properties of SiC-borosilicate glass composites evaluated from pushout and pullout tests. Journal of materials science letters, 10: 135-138, 1991.

[114] D. B. Marshall, M. C. Shaw and W. L. Morris. Measurement of interfacial debonding and sliding resistance in fiber reinforced intermetallic. Acta metallurgy materials, 40(3): 443-454, 1992.

[115] M. C. Watson and T. W. Clyne. The use of single fiber pushout testing to explore interfacial mechanics in SiC monofilament-reinforced Ti—II Application of the test to composite material. Acta Metallurgic materials, 40(1):141-148, 1992.

[116] M. C. Watson and T. W. Clyne. Reaction-induced changes in interfacial and macroscopic mechanical properties of SiC monofilament-reinforced titanium. Composites, 24(3): 222-228, 1992.

[117] M. C. Watson and T. W. Clyne. The tensioned push-out test for fiber-matrix interface characterization under mixed mode loading. Materials Science and Engineering, A160: 1-5, 1993.

[118] M. C. Watson and T. W. Clyne. The use of single fiber pushout testing to explore interfacial mechanics in SiC monofilament-reinforced Ti— I. A photoelastic study of this test. Acta Metallurgic materials, Vol.40, No.1: 131-139, 1992.

[119] W. A. Curtin, J. I. Eldridge and G. V. Srinivasan. Push-out test on a new silicon carbide/ reaction-bonded silicon carbide ceramic matrix composite. Journal of American Ceramic Society, 76(9): 2300-2304, 1993.

[120] S. W. Wang, A. Khan, R. Sands and A. K. Vasudevan, A novel nanoindetor technique for measuring fiber-matrix interfacial strength in composite. Journal of materials science letters, 11: 739-741, 1993.

[121] E. L. Curzio and M. K. Ferber. Methodology for determination of the interfacial properties of brittle matrix composites. Journal of materials science, 29: 6152-6158, 1994.

[122] M. Kuntz, K. H. Schlapschi, B. Meier and G. Grathwohl. Evaluation of interface parameters in push-out and pull-out tests. Composites, Vol 25, No. 7: 476-481, 1994.

[123] A. f. Kalton, C. M. Ward-Close and T. W. Clyne. Development of the tensioned push-out test for study of fiber/matrix interfaces. Composites, 25(7): 637-644, 1994.

[124] G. N. Morscher, J. M. Fernandez and M. J. Purdy. Determination of interfacial properties using a single-fiber microcomposite test. Journal of American Ceramic Society, 79(4) 1083-1091, 1996.

[125] R. Asthana and S. N. Tewari. Processing effects on interfacial sliding of debonded fibers in a sapphire-NiAl(Yb) composite. Journal of materials science letters, 16: 406-411, 1997.

[126] S. Q. Guo and Y. Kagawa. Characterization of interface sliding damage in SiC fiber-reinforced Ti-15-3 matrix composite by cyclic fatigue. Acta materials, 45(6): 2257-2270, 1997.

[127] D. H. Kuo, W. M. Kriven and T. J. Mackin. Control of Interfacial Properties through Fiber Coatings: Monazite Coating in Oxide-Oxide Composites. Journal of America Society, 80(12): 2987-2996, 1997.

[128] C. M. Huang, D. Zhu, X. D. Cong and W. M. Kriven. Carbon-coated-glass-fiber -reinforced cement composites: I, fiber push-out and interfacial properties. Journal of America Society, 80(9): 2326-2332, 1997.

[129] K. Honda, Y. Kagawa and Y. W. Mai. Effects of relative sliding distance on the frictional stress transfer in fiber-reinforced ceramics. Materials Science and Engineering, A252: 53–63, 1998.

[130] T. Hinoki, W. Zhang, A. Kohyama, S. Sato and T. Noda. Effect of fiber coating on interfacial shear strength of SiC/SiC by nano-indentation technique. Journal of Nuclear Materials, 258-263: 1567-1571, 1998.

[131] J. Ye, A. K. Kaw. Determination of mechanical properties of fiber-matrix interface from push-out. Theoretical and Applied Fracture Mechanics, 32: 15-25, 1999.

[132] Y. J. Sun and R. N. Singh. A technique for the determination of interfacial properties from debond length measurement. Journal of materials science, 35: 5681-5690, 2000.

[133] A. Brunet, R. Valle and A. Vassel. Intermetallic TiAl-based matrix composites: investigation of the chemical and mechanical compatibility of a protective coating adapted to an alumina fiber. Acta materials, 48:4763-4774, 2000.

[134] N. Chandra and H. Ghonem. Interfacial mechanics of push-out tests: theory and experiments. Composites: Part A, 32: 575-584, 2001.

[135] W. Yang, A. Kohyama, T. Noda, Y. Katoh, T. Hinoki, H. Araki and J. Yu, Interfacial characterization of CVI-SiC/SiC composites. Journal of Nuclear Materials, 307–311: 1088–1092, 2002.

[136] Y. Zhong, H, Chen, W. Hu and G. Gottstein. Fiber damage and high temperature tensile properties of Al2O3 fiber reinforced NiAl-matrix composites with and without hBN-interlayer. Materials Science and engineering A, 464: 241-248, 2007.

[137] O. Dezellus, B. Digonnet, M. S. Peronnet, F. Bosselet, D, Rouby and J. C. Viala. Mechanical testing of steel/aluminium-silicon interfaces by pushout. International Journal of Adhesion&Adhesive, 27:417-421, 2007.

[138] Y. Zhong, W. Hu, J. I. Eldridge, H, Chen, J. Song and G. Gottstein. Fiber push-out tests on Al2O3 fiber-reinforced NiAl-composites with and without hBN-interlayer at room and elevated temperature. Material Science and Engineering A, 488: 372-380, 2008.

[139] G. Rausch, B. Meier and G. Grathwohl. A Push-out technique for the evaluation of interfaical properties of fiber-reinforced materials. Journal of the European Ceramic Society, 10: 229-235, 1992.

[140] D. H. Grande, J. F. Mandell and K. C. C. Hong. Fiber-matrix bond strength studies of ceramic, and metal matrix composites. Journal of materials science, 23: 311-328 (FEM), 1988.

[141] K. Goto and Y. Kagawa. Crack-fiber interaction and interfacial failure models in fiber-reinforced ceramics. Materials science and engineering, A176: 357-361, 1994.

[142] J. Dinter, P. W. M. Peters and J. Hemptenmacher, Finite element modelling of the push-out test for SiC fiber-reinfroced titanium alloys. Composites part A, 27A: 749-753, 1996.

[143] A. F. Kalton, S. J. Howard, J. J.Rusch and T. W. Clyne. Measurement of interfacial fracture energy by single fiber push-out testing and its application to the titanium-silicon carbide system. Acta Mater, 46(9): 3175-3189(FEM and application), 1998.

[144] W. D. Zeng, P. W. M. Peters and Y. Tanaka. Interfacial bond strength and fracture energy at room and elevated temperature in titanium matrix composites (SCS-6/Timetal 834). Composites: Part A, 33:1159-1170, 2002.

[145] H, Chen, W. Hu, Y. Zhong and G. Gottstein. Finite element analysis of single-fiber push-out tests of continuous Al2O3 fiber reinforced NiAl composites. Materials Science and engineering A, 460-461: 624-632, 2007.

[146] P. D. Jero and R. J. Kerans. The contribution of interfacial roughness to sliding friction of ceramic fibers in a glass matrix. Scripta Metall Mater, 24: 2315-2318, 1990.

[147] T. J. Mackin, P. D. Warren and A. G. Evans. Effects of fiber roughness on interface sliding in composites, Acta metallurgy materials, 40(6): 1251-1257, 1992.

[148] H. Cherouali, G. Fantozzi, P. Reynaud and D. Rouby. Analysis of interfacial sliding in brittle-matrix composites during push-out and push-back tests. Materials Science and Engineering, A250: 169–177, 1998.

[149] B. Budiansky, A. G. Evans and J. W. Hutchinson. Fiber-matrix debonding effects on cracking in aligned fiber ceramic composites. International Journal of Solid structure, 32 (3/4): 315-328, 1995.

[150] B. Budiansky, J. W. Hutchinson, A. G. Evans. Matrix fracture in fiber-reinforced ceramis. Journal of Mechanics and Physics of Solids. 34 (2): 167-189, 1986.

[151] A. Herrmann. Interface Optimization of Tungsten Fiber-Reinforced Copper for Heat Sink Application, PhD thesis, Max-Planck-Institut für Plasmaphysik, 2009.

[152] R. D. Conner, R. B. Dandliker and W. L. Johnson. Mechanical properties of tungsten and steel fiber reinforced Zr41.25Ti13.75 Cu12.5Ni10Be22.5 metallic glass matrix composites,. Acta material, 46(17): 6089-6012, 1998.

[153] K. Q. Qiu, A. M. Wang, H. F. Zhang, B. Z. Ding and Z. Q. Hu, Mechanical properties of tungsten fiber reinforced ZrAlNiCuSi metallic glass matrix composite. Intermetallics. 10: 1283-1288, 2002).

[154] H. Zhang, L. Z. Liu, Z. F. Zhang, K. Q. Qiu, X. F. Pan, H. F. Zhang and Z. G. Wang, Deformation and fracture behavior of tungsten fiber-reinforced bulk metallic glass composite subjected to transverse loading. Journal of Material Research, 21(6): 1375-1384, 2006.

[155] Stand of test method for plane-strain fracture toughness of metallic materials. Designation: E399-90, Reapproved 1997

[156] J. D. Murphy, A. Giannattasio, Z. Yao, C. J. D. Hetherington, P. D. Nellist and S. G. Roberts. The mechanical properties of tungsten grown by chemical vapour deposition. Journal of Nuclear Materials. 386–388: 583–586, 2009.

[157] N. Chawla and K. K. Chawla. Metal Matrix Composite, first edition. Springer, New York, 2006.

[158] A. Ruina and R. Pratap, Introduction to Statics and Dynamics. Pre-print for Oxford University Press, January 2002.

Appendix

This section serves to state the theory and define the terminology employed in the following. A more in depth coverage of the theory is provided by e.g.[1,2]. In Bayesian probability theory (BPT), the viability of a hypothesis H (e.g. parameter values) is assessed by calculating the probability of the hypothesis given the observed data D and any background information I. Following Jeffreys [3] we write such a probability as $P(H \mid D,I)$. The BPT rests on two rules [4] for manipulating conditional probabilities. The sum rule states that the probabilities of a proposition H and the proposition that H is false (signified by $\overline{H}$) add up to unity:

$$P(H \mid I) + P(\overline{H} \mid I) = 1 \tag{A-1}$$

Throughout this work, we will be concerned with exclusive and exhaustive hypotheses, so that if one particular hypothesis is true, all the others are false. For such hypotheses the normalization rule

$$\sum_i p(H_i \mid I) = 1 \tag{A-2}$$

holds. The second rule is the product rule which states that a joint probability or probability density function $P(H \mid D,I)$ can be factorized such that one of the propositions becomes part of the condition (i.e. moves right of the vertical bar). Due to the symmetry with respect to H and D, this can be done in two ways:

$$P(H \mid D,I) = P(H \mid I)P(D \mid H,I) = P(D \mid I)P(H \mid D,I) \tag{A-3}$$

Comparison of the two equivalent decompositions in (A-3) yields Bayes' theorem

$$P(H \mid D,I) = \frac{P(H \mid I)P(D \mid H,I)}{P(D \mid I)} \tag{A-4}$$

Bayes' theorem relates the likelihood $P(D \mid H,I)$ to the posterior probability $P(H \mid D,I)$. The posterior probability distributions provide the full description of our state of knowledge about H. It is often necessary to summarize the distribution in terms of a few numbers. The most common description is given by the mean value of the posterior. Other possible choices are the position of the most probable value of the posterior (also termed maximum a posteriori (MAP) estimate) or the median of the distribution. For a symmetric distribution the mean value and the median coincide. All of those numbers may be strongly misleading in the case of skew or multimodal distributions. Eq.(A-4) reveals also that the maximum-likelihood (ML) estimate is

usually different from the posterior estimate except for the special case of a constant prior. The maximum-likelihood estimate obtained by maximizing the likelihood function is often mistaken as the most probable estimate given the data. This is not so: The obtained hypothesis is the one that would make the observed data most probable. This is logically quite different. The quantity that is required (the most probable estimate given the data) is instead given by the posterior probability $P(H \mid D,I)$. It is related to the likelihood function through the prior probability $P(H \mid I)$. From a different point of view Bayes' theorem is a recipe for learning. Initially available prior knowledge about the hypothesis H coded in the distribution $P(H \mid I)$ is modified by the new information provided by the measured data D to its posterior distribution $P(H \mid D,I)$. The last quantity to be explained in Eq. (A-4) is $P(D \mid I)$. It follows from the marginalization rule which is itself a consequence of the sum and product rule. The extremely important marginalization rule tells how to remove an 'unwanted' nuisance variable from a Bayesian calculation and can be considered as a generalized formula for error propagation:

$$P(D \mid M,I) = \sum_I P(H_i \mid M,I) P(D \mid H_i,M,I) \tag{A-5}$$

Here we have split off the model M which specifies the bunch of hypotheses H_i we are considering from the general background information I. That is, the denominator of Bayes' theorem, which does not depend on H plays the role of a normalization constant. An additional significance of the evidence derived from Eq.(A-5) is the probability of the data averaged over all hypotheses in the class specified by M. Therefore the evidence is of vital importance for model comparison but is not considered in the following.

To employ the Bayesian analysis a physical model (functional relationship) is needed, relating the parameters to be determined with the data.
For the curve fitting of Eq. (2.8), the functional relationship is given by

$$P_A(h_i) = f(h_i;\underline{\theta}_A,I) + \eta_A = 471 * \theta_1 \tanh(\theta_2 * h_i) + \eta_A \tag{A-6}$$

where $P_A(h_i)$ is the recorded complete debonding load for the specimen thickness of h_i, and the parameters of this model $\underline{\theta}_A = \{\theta_1, \theta_2\}$ are θ_2 the shear-lag parameter and θ_1 the product of interfacial shear strength (MPa) divided by θ_2. The measurement noise η_A for the data points $P_A(h_i)$ $i = 1,\ 2,\ 3 \ldots$Ndata (typically the number of tested specimens) is assumed to be Gaussian in with mean zero and standard deviation σ_i for all cases in this work.

For the curve fitting of Eq. (2.16), the functional relationship is given by

$$P_B(l_i) = f(l_i;\underline{\theta}_B,I) + \eta_B = 0.129 * \theta_3 * [\exp(3.64 * \theta_4 * l_i) - 1] + \eta_B \tag{A-7}$$

where $P_B(l_i)$ is the friction load for the sliding length l_i, and the parameters of this model $\underline{\theta}_B = \{\theta_3, \theta_4\}$ are θ_3 the interface radial stress and θ_4 the friction coefficient.
For the curve fitting of Eq. (2.18), the functional relationship is given by

$$P_C(h_i) = f(h_i; \underline{\theta}_C, I) + \eta_C = 146 * \sqrt{\theta_5} * \exp(3.64 * \theta_4 * h_i) - \frac{\theta_3}{0.1365}[\exp(3.64 * \theta_4 * h_i) - 1] + \eta_C \quad \text{(A-8)}$$

where $P_C(h_i)$ is the peak-applied stress with specimen thickness of h_i, and the parameters of this model $\underline{\theta}_C = \{\theta_3, \theta_4, \theta_5\}$ are θ_3 the interface radial stress, θ_4 the friction coefficient, and θ_5 the interfacial fracture energy. In this work Eqs. (A-7) and (A-8) were **jointly** estimated.

The distribution of the noise η_i is assumed to be Gaussian, thus the generic likelihood function for all three cases is given by

$$P(\underline{d} \mid \underline{f}, I) = \frac{1}{\prod_{i=1}^{N_d} \sqrt{2\pi\sigma_i^2}} * \exp\left[-\frac{1}{2}\sum_{i=1}^{N_d} \frac{(d_i - f(x_i; \underline{\theta}, I))^2}{\sigma_i^2}\right] \quad \text{(A-9)}$$

The prior distributions for the parameter vector is taken as flat $p(\underline{\theta} \mid I)$ =const. within physical sensible bounds. The posterior distribution is sampled using rejection Monte Carlo, thus ensuring independent samples. Summarizing quantities like mean and variance of the parameters can then be easily derived using the standard equations e.g.

$$\langle \underline{\theta} \rangle \approx \frac{1}{N}\sum_{i=1}^{N} \underline{\theta}_i \quad \text{(A-10)}$$

although in this nonlinear case the full posterior distribution is much more informative (e.g. Fig. A-1 for θ_1 and θ_2 while Fig. A-2 for θ_3, θ_4 and θ_5). It should be pointed out that predictive computations are feasible, based on the computed posterior sample. In Fig. A-1, although the error bar of θ_1 and θ_2 are extremely large, the product of them—interfacial shear strength τ_d, which is the interested parameter for this work—can be estimated with high precision.

For further details referred to in the computation codes one may consult **Dr. Toussaint** (udo.v.toussaint@ipp.mpg.de)

Reference

[A1] D. S. Sivia. Data analysis - A Bayesian Tutorials. Clarendon, Oxford, 1996.

[A2] T. Leonard and J. S. J. Hsu. Bayesian Methods: An Analysis for Statisticians and Interdisciplinary Researches. Cambridge University Press, Cambridge, 1999.

[A3] H. Jeffreys. Theory of Probability. Oxford University Press, Oxford. 1961.

[A4] R. T. Cox. Probability, frequency and reasonable expectation. American Journal of Physics, 14:1-13, 1946.

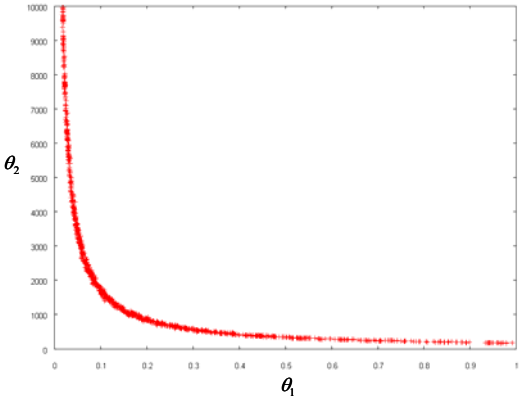

Figure A-1. Full posterior distribution of θ_1 and θ_2 for the ZrO_x&W 260 interface

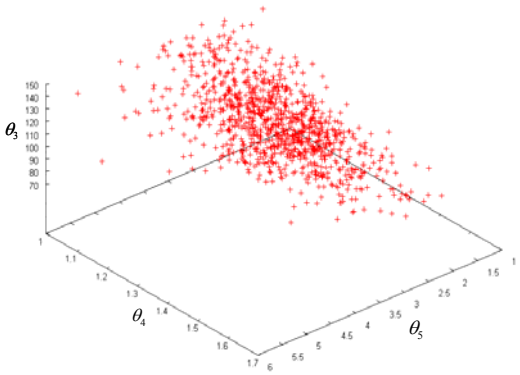

Figure A-2. Full posterior distribution of θ_3, θ_4 and θ_5 for the ZrO_x&W 260 interface

Acknowledgments

First and foremost, I would like to thank **Prof. Dr.-Ing. Dr.-Eng. Harad Bolt** for providing me the opportunity to pursue my dissertation at IPP, and guiding me through the entire process; as well as **Prof. Dr. E. Werner** and **Prof. Dr. H. Baier** for allowing me to pursue my doctorate degree at the Maschinenwesen department of TU München. I am grateful to my supervisor, **Dr. Jeong-Ha You**, for his guidance and encouragement during the past three years. Another Thank You goes to **Dr. Joachim Roth** for his oversight and approval in all purchases and conference related matters. A heart-felt thanks to **Dr. Christian Linsmeier** for giving me the direction when I was depressed with writing my thesis, and to **Dr. Hans Maier** for his critical reading of the chapters and relevant discussions. I owe my gratitude to **Dr. Karl Ertl** for his kind concern and assistance for my work in MF.

Special thanks to **Till Höschen** for all of his technical assistance and patient guidance, as well as his encouragement. My gratitude goes to **Freimut Koch** for his support with the magnetron sputtering process and to **Calvin Prentice** for providing me with the CVD process. Hearty thanks goes to **Dr. Annegret Brendel** for her revision of my thesis and patient guidance with the nano-indenter device. I am indebted to my many colleagues for supporting me during the interface investigation. **Marcin Rasinski**, **Stefan Lindig**, and **Dr. Martin Balden** helped me with the microstructure analysis at the SEM/FIB device. **Dr. Carmen Höschen** helped me with the SIMS analysis. **Dr. Christoph Adelhelm** helped me with the XRD analysis, and **Gabriele Matern** helped me with the specimen preparation as well as the SEM analysis. I am obliged to **Dr. Udo von Toussaint** for leading me through the curve fitting procedure of the interfacial parameters calibration. To **Stefan Wurster** for providing me with the 3PB test and his elaborate interpretation.

Many thanks to the division secretaries, **Anne Eggeling** and **Monika Mezger**, for help with regard many non-scientific parts of my life which would otherwise have been very difficult to handle for someone who had come to Germany the first time.

I am grateful to my best friend and colleague **Beata Tyburska**, for unreservedly supporting, inspiring, and encouraging me in both my work and daily life during my stay in Germany. I would like to express my deepest appreciation to **Dr. Moritz J. Püschel** for his invaluable support in revising the English of my thesis. I would like to thank **Johann Riesch** for his support with the German abstract. Among the many who deserve to be acknowledged are **Dr. Kazuyoshi Sugiyama**, **Dr. Verena Paffenholz**, **Dr. Aurelia Herrmann**, **Joachim Dorner**, **Michael Fußeder**, and **Arno Weghorn** for their assistance and friendship during my stay at IPP.

Thank you, fellow PhD students, **Weizhi Yao**, and **Martin Köppen** for your friendship and help. Thank you to my neighbors **Itxaso**, **Inma**, **Marcin**, **Yury**, **Sergio**, **Alex** for making my stay here so full of new cultures, languages, and cuisines.

I am grateful to the Chinese Scholarship Council (CSC) for their financial support.

Last but not least, I would like to thank Shaoning for supporting me always and of course my family for their support and belief throughout my everlasting schooling process. Without them none of this would have been possible.